

Warsaw University of Technology

F A C U L T Y O F P H Y S I C S



Master's diploma thesis

in the field of study Applied Physics
and specialisation Complex Systems Modeling

Dynamics of quantized vortex in superfluid medium with impurities

Dynamika wiru kwantowego w nadciekłym układzie zawierającym niejednorodności

inż. Konrad Kobuszewski

student record book number: 251697

Thesis supervisor:

dr hab. inż. Gabriel Włazłowski

WARSZAWA 2018

Abstract

Title of the thesis: Dynamics of quantized vortex in superfluid medium with impurities.

The main goal of the thesis was to investigate the Vortex Filament Model and construct an approach suitable for numerical simulations of superfluids with impurities immersed in the medium. This kind of systems appears in the research of liquid Helium, type II superconductors and neutron stars crust. The prepared program was also utilized to perform numerical simulations in the third of these cases.

Due to the aim for understanding the theory and various approximations to Vortex Filament Model, the literature investigation was done. The results are shown in the chap. 3. and 4. Also there are presented derivations repeated independently by the author of this thesis. The rest of chap. 3 contains some general information on theory of superfluidity and in the chap. 4 a review of the earlier research on vortex-impurity interaction is provided. For the simulation planning purpose, some knowledge on the neutron star physics was required, thus several aspects used in the further parts of the thesis are discussed in chap. 2.

In the chap. 5 a precise description of programs used for the simulations is provided, including the exploited algorithms, a software implementation, tests on correctness of the code and the simulation planning process.

The rest of the thesis contains results of the preformed simulations of vortex line in an environment imitating the neutron star crust case — vortex immersed in a lattice of impurities. The elaborated approach was utilized. Due to low numerical complexity of the Vortex Filament Model, a large number of vortex line trajectories moving through the lattice was obtained. The impact of external flows, dissipation rate, impurities average spacing and configuration was examined to reveal the conditions for pinning of the vortex line to the lattice of impurities. Vortex pinning is considered as an important phenomena that triggers sudden changes in neutron stars rotation periods — the glitches.

Two main conclusions of the simulations are achieved: a surprising impact of dissipation force on types of vortex trajectories appearing when changing velocity of external flow and possible sensitivity of vortex motion to the spatial impurity placement. Both of these issues have not been widely described in subject literature yet and can exhibit relevant effects on the neutron star crust dynamics.

Keywords:

quantum vortex, neutron star glitches, superfluidity, Vortex Filament Model, vortex line dynamics, Cython C extensions

(Supervisor)

(Student)

Streszczenie

Tytuł pracy: Dynamika wiru kwantowego w nadciekłym układzie zawierającym niejednorodności

Głównym celem niniejszej pracy magisterskiej było zbadanie możliwości użycia Vortex Filament Model do symulacji numerycznych nadciekłego systemu zawierającego domieszki. Tego typu układy są spotykane w badaniach nad ciekłym Helem, nadprzewodnikami drugiego rodzaju i gwiazdami neutronowymi. Przygotowany program został użyty do przeprowadzenia symulacji w trzecim z tych przypadków.

W celu dokładnego zrozumienia teorii i przybliżeń, które można zastosować w Vortex Filament Model, obszerna analiza literatury została przeprowadzona. Jej wyniki przedstawiono w rozdziałach 3. i 4. Także w tych rozdziałach pokazano wyprowadzenia, które zostały samodzielnie powtórzone przez autora pracy. Reszta rozdziału 3. zawiera ogólne informacje o teorii układów nadciekłych, a w 4. rozdziale zawarto informację na temat wcześniejszych badań oddziaływań wiru i domieszek w gwiazdach neutronowych. W celu zaplanowania symulacji konieczna okazała się wiedza na temat fizyki gwiazd neutronowych. Niezbędne informacje zamieszczono w rozdziale 2.

Rozdział 5. zawiera dokładny opis programu użytego do symulacji, włączając użyte algorytmy, szczegóły implementacji, testy poprawności działania kodu i opis procesu planowania symulacji.

Reszta pracy opisuje wyniki symulacji wiru przeprowadzone dla układu imitującego łąrodowisko wewnętrznej skorupy gwiazdy neutronowej (ang. inner crust). W tej warstwie gwiazdy spodziewane jest występowanie nadciekłej materii neutronowej i zanurzonych w niej jąder atomowych. Ponadto jądra tworzą sieć krystaliczną. Dzięki dużej efektywności zastosowanego podejścia możliwe było przeprowadzenie w krótkim czasie dużej liczby symulacji wiru poruszającego się przez sieć domieszek. W symulacjach zbadano wpływ zewnętrznego przepływu, dyssypacji oraz rozmieszczenia domieszek i średniej wzajemnej odległości między nimi. Starano się określić warunki w jakich wir może być "przypięty" do sieci domieszek. Wg obecnego stanu wiedzy zjawisko przypięcia wiru może tłumaczyć nagłe zmiany prędkości obrotu gwiazdy neutronowej.

Dzięki analizie wyników symulacji wysnuto dwa generalne wnioski: siła dyssypacji pomimo relatywnie małej wartości może mieć duży wpływ na dynamikę wiru oraz konfiguracja domieszek w sieci krystalicznej może mieć znaczący wpływ na charakter ruchu wiru. Do tej pory obie kwestie nie były dostatecznie zbadane, chociaż mogą mieć znaczący wpływ na makroskopową dynamikę skorupy gwiazdy neutronowej.

Keywords:

wir kwantowy, glitch w gwiazdzie neutronowej, nadciekłość, Vortex Filament Model, dynamika wiru kwantowego, rozszerzenia Cython

(Promotor)

(Student)

Oświadczenie o samodzielności wykonania pracy

Politechnika Warszawska
Wydział Fizyki

Ja, niżej podpisany:

Konrad Kobuszewski, nr albumu 251697

student Wydziału Fizyki Politechniki Warszawskiej, świadomy odpowiedzialności prawnej oświadczam, że przedłożoną do obrony pracę dyplomową magisterską pt.:

Dynamics of quantized vortex in superfluid medium with impurities

(Dynamika wiru kwantowego w nadciekłym układzie zawierającym niejednorodności)

wykonałem samodzielnie pod kierunkiem

dra hab. inż. Gabriela Włazłowskiego

Jednocześnie oświadczam, że:

- praca nie narusza praw autorskich w rozumieniu ustawy z dnia 4 lutego 1994 o prawie autorskim i prawach pokrewnych, oraz dóbr osobistych chronionych prawem cywilnym,
- praca nie zawiera danych i informacji uzyskanych w sposób niezgodny z obowiązującymi przepisami,
- praca nie była wcześniej przedmiotem procedur związanych z uzyskaniem dyplomu lub tytułu zawodowego w wyższej uczelni,
- promotor pracy jest jej współtwórcą w rozumieniu ustawy z dnia 4 lutego 1994 o prawie autorskim i prawach pokrewnych.

Oświadczam także, że treść pracy zapisanej na przekazanym nośniku elektronicznym jest zgodna z treścią zawartą w wydrukowanej wersji niniejszej pracy dyplomowej.

Warszawa, February 2, 2018

(podpis dyplomanta)

Oświadczenie o udzieleniu Uczelni licencji do pracy

Politechnika Warszawska
Wydział Fizyki

Ja, niżej podpisany:

Konrad Kobuszewski, nr albumu 251697

student Wydziału Fizyki Politechniki Warszawskiej, niniejszym oświadczam, że zachowując moje prawa autorskie udzielam Politechnice Warszawskiej nieograniczonej w czasie, nieodpłatnej licencji wyłącznej do korzystania z przedstawionej dokumentacji pracy dyplomowej pt.

Dynamics of quantized vortex in superfluid medium with impurities

(Dynamika wiru kwantowego w nadciekłym układzie zawierającym niejednorodności)

w zakresie jej publicznego udostępniania i rozpowszechniania w wersji drukowanej i elektronicznej¹.

Warszawa, February 2, 2018

(podpis dyplomanta)

¹Na podstawie Ustawy z dnia 27 lipca 2005 r. Prawo o szkolnictwie wyższym (Dz.U. 2005 nr 164 poz. 1365) Art. 239. oraz Ustawy z dnia 4 lutego 1994 r. o prawie autorskim i prawach pokrewnych (Dz.U. z 2000 r. Nr 80, poz. 904, z późn. zm.) Art. 15a. "Uczelni w rozumieniu przepisów o szkolnictwie wyższym przysługuje pierwszeństwo w opublikowaniu pracy dyplomowej studenta. Jeżeli uczelnia nie opublikowała pracy dyplomowej w ciągu 6 miesięcy od jej obrony, student, który ją przygotował, może ją opublikować, chyba że praca dyplomowa jest częścią utworu zbiorowego."

Contents

1	Introduction	15
1.1	Superfluid media with impurities	15
1.2	Pulsars — rotating neutron stars	17
1.3	Goals and motivation of work	19
1.4	Possible applications of constructed code for numerical simulations	21
2	Neutron stars	23
2.1	Basiscs of neutron stars physics	23
2.1.1	Tolman–Oppenheimer–Volkoff equation	23
2.1.2	Equation of state of nuclear matter	24
2.1.3	Internal structure of neutron stars	25
2.1.4	Spherical Wigner-Seitz cells method for neutron star matter	27
2.2	Neutron star glitches	30
2.2.1	Rotation of neutron star crust	30
2.2.2	Origin of glitches	31
2.2.3	Intervortex spacing	32
2.2.4	Energy of two rectlinear vortices in Vortex Filament Model	32
3	Theoretical description of superfluids	35
3.1	Microscopic theory of superfluidity	35
3.1.1	Coherence length	36
3.2	Density functional approach and Superfluid Local Density Approximation.	37
3.2.1	Basics of density functional theory	37
3.2.2	Superfluid Local Density Approximation	38
3.3	Vortex Filament Model	39
3.3.1	Vortex Filament Model derivation	39
3.3.2	Solving Vortex Filament Model without additional approximations	42
3.3.3	General approximation for small deflections from straight vortex line	44
3.4	Approximations to Vortex Filament Model	45

3.4.1	Motivations for approximating Biot-Savart integral	45
3.4.2	Local Induction Approximation and its applicability	45
3.4.3	Model of vibrations of columnar vortex	47
3.4.4	Final equations used for numerical simulations of Vortex Filament Model	49
4	Vortex-impurity interaction in neutron star crust	51
4.1	Vortex-nucleus force in neutron star crust	51
4.1.1	Hydrodynamical approach	51
4.1.2	Effective force approach and method of obtaining this force from microscopic quantum model (TDSLDA)	52
4.1.3	Comparison of estimates on vortex-nucleus force magnitude	56
4.2	Kelvin waves dispersion relation	59
4.2.1	Spectrum of vortex waves in TDSLDA simulations	59
4.2.2	Trials of detrending vortex motion signal for analysis	60
5	Metodology of numerical simulations	61
5.1	Utilized algorithms	61
5.1.1	Discretization of vortex line	61
5.1.2	Method of solving the equations of motion	61
5.1.3	Algorithm steps	62
5.1.4	Scaling and execution time	64
5.2	Software implementation	65
5.2.1	Applied programming tools and organization of code	65
5.2.2	General output from simulations	65
5.3	Verification of correctness of numerical simulations	67
5.3.1	Correctness tests	67
5.3.2	Impact of time step and vortex elements spacing	67
5.4	The planning of simulations imitating neutron star crust environment	70
5.4.1	Vortex-nucleus force parameters	70
5.4.2	Other parameters of SVFM	70
5.4.3	Frame of reference	71
5.4.4	Configuration of the impurity lattice	71

6 Results of numerical simulations	75
6.1 System consisting of single vortex and single nucleus	75
6.1.1 Comparison of vortex-nucleus system evolution in TDSLDA to Vortex Filament Model simulations	75
6.1.2 Spectrum of waves on a vortex line in SVFM simulations	76
6.2 Simulations of vortex moving through a lattice of impurities.	78
6.2.1 General remarks on results of simulations	78
6.2.2 Types of trajectories observed in numerical simulations	80
6.2.3 Inspection of methods for evaluation mean vortex velocity	80
6.2.4 Analysis of factors affecting vortex motion through the lattice	83
6.3 Impact of configuration of impurity lattice on vortex motion	85
7 Resume of numerical simulations, conclusions and further research proposal	87
7.1 Conclusions	87
7.1.1 Theoretical part of work	87
7.1.2 Summary of numerical simulations	88
7.2 Further research proposal	89
A Mathematical description of curves	91
A.1 Natural parameter of a curve	91
A.2 Frenét vectors	91
A.3 Frenét-Serret formulas	93
B Stability of numerical methods for solving ODEs	94
B.1 Definition of stability for numerical schemes	94
B.1.1 Stability function of a numerical method	94
B.1.2 A-stable methods	94
B.1.3 L-stable methods	94

Chapter 1

Introduction

1.1 Superfluid media with impurities

Superfluidity is a phenomena known since discovery of inviscid flow of ^4He below critical temperature $T_c = 2.17 \text{ K}$ made by P. L. Kapitza and independently by J.F. Allen & A.D. Misener [1, 2]. Similar behavoiur was observed (or suspected) in wide range of systems ranging from liquid ^3He [3], BEC condensates [4, 5] throughout some asymmetric nuclei [6, 7] and up to quark-gluon plasma [8]. Similar phenomena for charged particles implies non-dissipative current and is refereed as superconductivity, but the microscopic origin of such effects is the same in both cases. From theoretical point of view the classification depends rather on type of particles forming the medium and, due to existence of two main components of matter — bosons and fermions, a bosonic-like or a fermionic-like superfluidity can be distinguished.

In both cases, bosonic and fermionic superfluidity can occur only in sufficiently low temperatures. In the superfluid state U(1) symmetry of the order parameter is broken. In Ginzburg-Landau theory of phase transitions free energy of the system is related to the complex order parameter ψ with formula:

$$F = \frac{\hbar^2}{2m} |\nabla\psi|^2 + A|\psi|^2 + B|\psi|^4 + \mathcal{O}(|\psi|^6). \quad (1.1)$$

Comparison with corresponding formula in Bardeen-Cooper-Schriefer theory (see section 3.1) implies that the paring field Δ plays a role of the order parameter in case of fermionic ensembles.

Surprisingly, occurrence of superfluidity (or superconductivity) in condensed matter is not very sensitive to presence of impurities — it was explained theoretically by P. W. Anderson. In article [9] he extended derivation of Bardeen-Cooper-Schrieffer theory from infinite system with translational symmetry towards finite systems (i.e. for Hamiltonians where translational invariance is broken). Brief introduction to this microscopic theory of superfluidity is discussed in section 3.1.

At the same time concept of superfluidity was introduced in low energy nuclear physics. Authors A. Bohr, B. R. Mottelson, D. Pines [6] and A. B. Migdal [7] proposed to consider BCS-like paring between neutrons and protons in nuclear systems. Presently we know, that the paring

plays important role in large-amplitude collective motion of nuclei, where one of the most important example is nuclear fission [10].

While it may sound surprising, superfluidity is expected to occur in neutron star interiors. Even though the temperature of the star seems to be high when expressed in absolute units, of order of $10^7 \div 10^8$ K ≈ 0.01 MeV [11, 12], it turns that it corresponds to energy of thermal excitations to be only a tiny fraction of Fermi energies of protons and neutrons: $\varepsilon_{F,n}, \varepsilon_{F,p} \approx 10 \div 100$ MeV. Moreover, because of an attractive character of the nuclear force and the high degeneracy $\varepsilon_F \gg k_B T$ the nucleons become superfluid at critical temperatures of the order of $T_c \approx 10^9$ K [12]. Further introduction to subject of neutron stars will be provided in sec. 1.2 and in chapter 2.

It is worth to mention that neutron stars are the only fermionic system not generated by humans which manifests superfluidity. Simultaneously, these the largest superfluid systems that can be found in nature.

1.2 Pulsars — rotating neutron stars

The discovery of first radio pulsar by J. Bell in 1967 started new era of research in astrophysics. The observation was quickly explained connecting the phenomenon with existence of frequently rotating, extremely magnetized and massive star [13]. The only candidate for such object was a neutron star¹ — the concept introduced by F. Zwicky in paper [14].

Since their discovery, they are intensively studied, not only by astronomers, but also by theorist from nuclear physics community, because they have to consist of very dense and exotic forms of nuclear matter generated by enormous pressure. Despite many decades of studies many aspects of these systems is not well understood. One of them is phenomenon called *neutron star glitch*, and it will be subject of this thesis.

Neutron stars have huge moment of inertia (of order of $10^{45} \text{ g} \cdot \text{cm}^2$ [11]) which leads to exceptionally stable rotation rates and makes pulsars one of the most precise clocks in the universe. The rotation frequency of neutron star rotation decreases slowly², because the star radiates energy in form of electromagnetic and gravitational waves. However, precise measurements shows that pulsar from time to time abruptly increase its rotation frequency³. The phenomena of sudden increase of the pulsation frequency is called a *glitch* and I will refer to it throughout this thesis.

The glitches cannot be explained by interaction with other objects in neighbourhood of the neutron star, so number of theories have been proposed over years which relate increase of the rotation frequency to internal dynamics of the star. The most influential hypotheses are associated with superfluid neutron stars. First on them, conjectured by P. W. Anderson and N. Itoh in 1975 [17], connects a glitch with angular momentum transfer between vortices in superfluid neutron matter and nuclei forming the star crust. This process is accompanied by temporal confinement of vortex lines around nuclei, called *pinning*. The second hypothesis proposed in paper by M. Ruderman [18] is based on so-called Tkachenko waves propagating in lattice of quantum vortices [19]. The topic of glitches is discussed in more details in section 2.2.

¹Neutron stars have small period of rotation (of order from milliseconds to tens of seconds) as they relatively small objects in comparison to other stars (estimates of radii of these stars vary from 10 to 15 km). On the other hand their period of rotation is stable implying sufficiently large mass implying that interior of a pulsar must have densities comparable with density of nuclear matter.

²The spin-down rate of neutron stars usually falls within the range of 10^{22} to $10^9 \text{ s} \cdot \text{s}^{-1}$, for reference see chap. 6 in [15].

³The first event of this type was detected in 1969 by V. Radhakrishnan and R. N. Manchester for Vela pulsar [16].

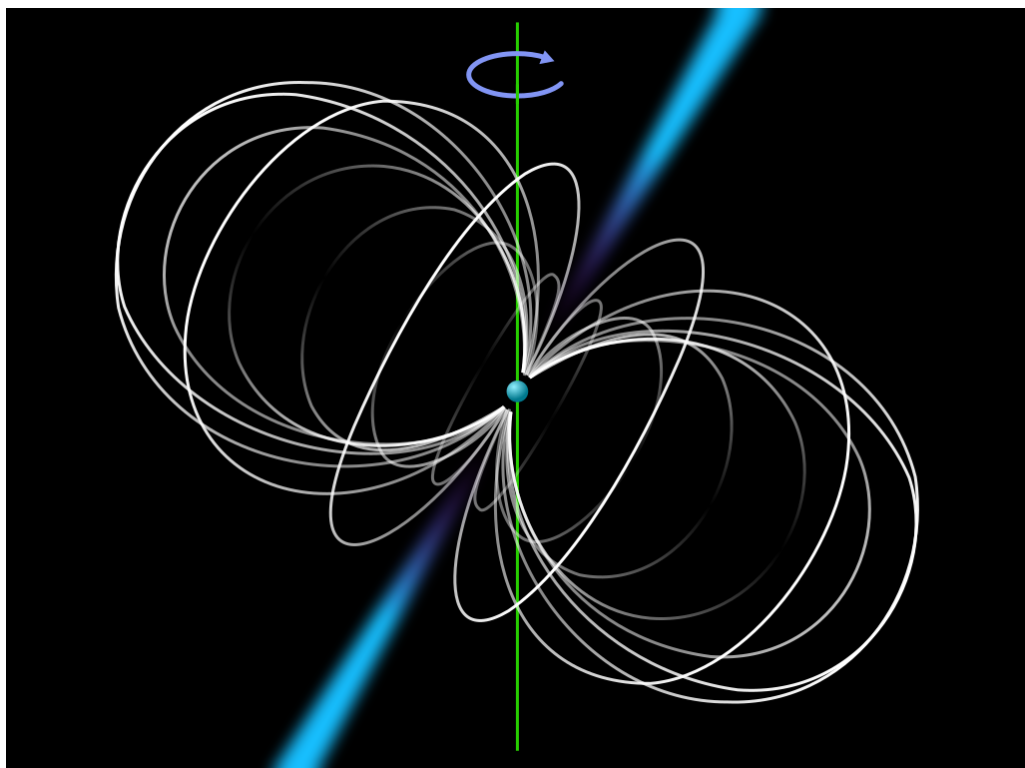


Figure 1.1: Schematic explanation of regular radio pulses — ionized matter falls towards surface of neutron star along lines of extremely huge magnetic field and the acceleration of charged particles in this field is source of electromagnetic radiation, picture taken NASA materials, <http://svs.gsfc.nasa.gov/10144>.

1.3 Goals and motivation of work

This work concentrates on superfluidity in neutron star crust. Systematic studies devoted to the internal structure (see section 2.1.3) revealed a region, called inner crust, where neutrons are dripping out from nuclei and are forming superfluid sea, while protons still form localized structures, which are called *impurities*.

The main aim of this work was to construct numerical code for solving equations of Vortex Filament Model (see section 3.3.1) that can be utilized for investigation of vortex dynamics in presence of multiple impurities. Two approximations of this model were studied. Parameters of these semi-classical models were extracted from existing results obtained by means of fully microscopic simulations, see section 3.2. Contrary to microscopic approaches, the semi-classical approach is computationally tractable for systems consisting of many quantum vortices and many impurities. The code was used to perform simulations of a vortex moving through a lattice of impurities in inner regions of a neutron star crust. Results of these simulations consist the main result of this thesis.

The topic of the thesis is mostly motivated by paper of G. Włazłowski, K. Sekizawa, P. Magierski, A. Bulgac, M. McNeil Forbes [20], where the force acting between quantum vortex (in superfluid neutron matter) and impurity was estimated from microscopic time-dependent simulations (see section 3.2). Semi-classical model of the vortex motion, based on approximation exploiting expansion in displacements of vortex element from straight line, was proposed earlier by B. Link in paper [21]. In B. Link's calculations the force acting between vortex and impurity was proposed arbitrarily without any connection to microscopic theories. Thus there is an essential need for re-examination of the system.

In order to investigate motion of vortex in the inner crust a number of tasks was undertaken, including deeper insight into theory of fermionic liquids described in chapter 3. Moreover, in chapter 4 the results of my own research on vortex pining in neutron stars are presented and previous estimates of vortex-nucleus interaction are compared to the work [20]. The excitations of vortex line called Kelvin waves were also investigated using results of microscopic simulations in order to reveal the dispersion relation needed in semi-classical description. The final results of the Vortex Filament Model simulations are demonstrated in chapter 6.

Vortex Filament Model simulations consists intermediate step between microscopic and macroscopic description of the star. As origin of the glitch is related to quantized vortices, the relevant length scales vary from fm (size of the vortex core) up to km (size of the star). It is clear that so wide range of scales cannot be captured effectively by single description. This makes the glitch problem very challenging system for formulating theories. Typically, it is attacked by series of approaches working at different length scales. Schematic representation of this idea is shown on fig. 1.2. Vortex Filament Model simulations based on parameters extracted from microscopic theory can give input to approaches applicable for dynamics on scales comparable with whole neutron star, i. e. Hall-Vinen-Bekherevich-Khalatnikov hydrodynamics.



Figure 1.2: Hierarchy of models in neutron stars physics.

1.4 Possible applications of constructed code for numerical simulations

The model was exploited here only for the neutron star crust, however various superfluid or superconducting systems can be possibly treated within Vortex Filament Model, thus the constructed code can have many applications in condensed matter physics.

One of them can be visualization of vortices in superfluid helium ^3He . In experimental studies the doping of liquid helium with impurities is widely applied for optical detection, enabling indirect measurements of fluid flow patterns. In other words, the vortices can be visualized by light interaction with impurities. Some examples of particle tracers in application for investigation of superfluids are described in papers [22, 23]. Recently, simulations of vortex-impurity system in model of coupled Gross-Pitaevskii equations was presented in paper of A. Pshenichnyuk and N.G. Berloff [24]. The authors argue that their model is equivalent to Landau's two fluid model, as well as Vortex Filament Model in form proposed by K. W. Schwarz [25]. While the methodology based on coupled non-linear Schrödinger equations looks to be very attractive, still it is numerically too complex to be applied to systems consisting of hundreds or more vortices and impurities. It scales as N^2 , where N is number of grid points, while complexity of the Vortex Filament Model scales as square of number of elements representing the vortex lines.

Another system where constructed tool can advance current research are type-II superconductors. Since the breakthrough in research made by G. Bednorz and K. A. Müller, whose discovery of high-temperature superconducting materials [26] was awarded a Nobel Prize in physics in 1987, efforts in this branch have been intensified, mainly due to industrial applications of the superconductors. Recently, a model for vortex dynamics in impure superconductors, similar to discussed in this thesis, was proposed in paper of D. Apushkinskaya, E. Apushkinskiy and M. Astrov [27]. It demonstrates applicability of the Vortex Filament Model for investigation of various aspects of superconducting dynamics, especially dynamics of vortices generated by magnetic fields.

Chapter 2

Neutron stars

2.1 Basics of neutron stars physics

2.1.1 Tolman–Oppenheimer–Volkoff equation

Assuming that matter in neutron star can be treated as irrotational ideal fluid¹ we can postulate metric² in form [28]:

$$g_{\mu\nu}dx^\mu dx^\nu = e^{\nu(r)}c^2dt^2 - e^{\lambda(r)}dr^2 - r^2d\theta^2 - r^2\sin^2\theta d\phi^2, \quad (2.1)$$

which is similar to Schwarzschild metric. Note that in above formula spherical symmetry is assumed. Irrotational metric (2.1) leads to great simplifications in Einstein's equation (2.3). If within the perfect fluid assumption we neglect effects related to star rotation, the stress-energy tensor $T_{\mu\nu}$ becomes diagonal, with eigenvalues of energy density and pressure given by:

$$T_0^0 = \rho(r)c^2 \quad T_i^j = -P(r)\delta_i^j \quad (2.2)$$

Having the stress-energy tensor one can solve Einstein's field equations to obtain matter distribution:

$$\frac{8\pi G}{c^4}T_{\mu\nu} = G_{\mu\nu}. \quad (2.3)$$

In case of irrotational ideal fluid picture the main interest concerns a relation between the matter distribution in curved space-time and the pressure. The relation derived under highlighted assumptions is given by:

$$\frac{dP}{dr}(r) = -\frac{G}{r^2} \left(\rho(r) + \frac{P(r)}{c^2} \right) \left(M(r) + 4\pi r^3 \frac{P(r)}{c^2} \right) \left(1 - \frac{2GM(r)}{c^2 r} \right)^{-1} \quad (2.4)$$

$$\frac{dM}{dr}(r) = 4\pi r^2 \epsilon[\rho](r), \quad (2.5)$$

¹Formally a fluid with no viscosity and no thermal conduction.

²In case of formula (2.1) Einstein's summation convention was used.

which is the relativistic equation of hydrostatic equilibrium — the Tolman-Oppenheimer-Volkoff equation. $M(r)$ stands for mass of matter inside a sphere of radius r and additional equation is needed to obtain this value — the Equation of State (EoS) (look at section 2.1.2).

The functional $\epsilon[\rho]$ is energy density in sense of Einstein's general relativity theory — the deformation of space-time is caused by mass of particles as well as by their kinetic and interaction energies. In general the energy density is a functional of density of the particles.

One of conclusion emerging from eq. (2.4) is that stars created in a supernova explosions have upper limit of mass. Current approximations of this limit vary from 1.5 to 3.0 solar masses [29] (depending on different types of EoS, see succeeding sec. 2.1.2) and lower limit of mass of neutron star is described by Chandrasekhar limit (fixing it at 1.4 solar mass). Presently, the heaviest detected neutron star has mass of approximately 2.01 solar mass [30].

2.1.2 Equation of state of nuclear matter

Using microscopic theory of nuclear matter one can find formula for energy per nucleon $E_i(n_i)$ (subscript i stands for p — protons, n — neutrons) and the energy density of nuclear matter is given by:

$$\epsilon = (E_n + m_n c^2)n_n + (E_p + m_p c^2)n_p \quad (2.6)$$

$n_{n,p}$ - particle density of neutrons,protons

$m_{n,p}$ - invariant mass of neutrons,protons

$$P \approx \left(\frac{\partial E}{\partial V} \right)_T = -\frac{N^2}{n^2} \left(\frac{\partial \epsilon}{\partial n} \right)_T, \quad n = (N_n + N_p)/V \quad (2.7)$$

Equation usually written in form

$$F(\rho, P) = 0 \quad (2.8)$$

is called as the equation of state. Extraction of this equations usually requires complicated calculations and recent overview is given in paper [31].

The EoS of neutron matter around nuclear densities is important for several reasons, but in case of interest of the thesis most important is its contribution to chemical potential in beta equilibrium condition (2.9), thus different models of EoS result in varying dependency of structure of impurities appearing in neutron star crust on baryons density. Moreover the EoS provides a direct comparison between different frameworks for the nuclear Hamiltonian in microscopic theories.

Combining TOV equation (2.4) and EoS (2.8) we can describe mass density with respect to distance from the centre of mass of the star. The results of research on the topic is described further in the next section (2.1.3).

2.1.3 Internal structure of neutron stars

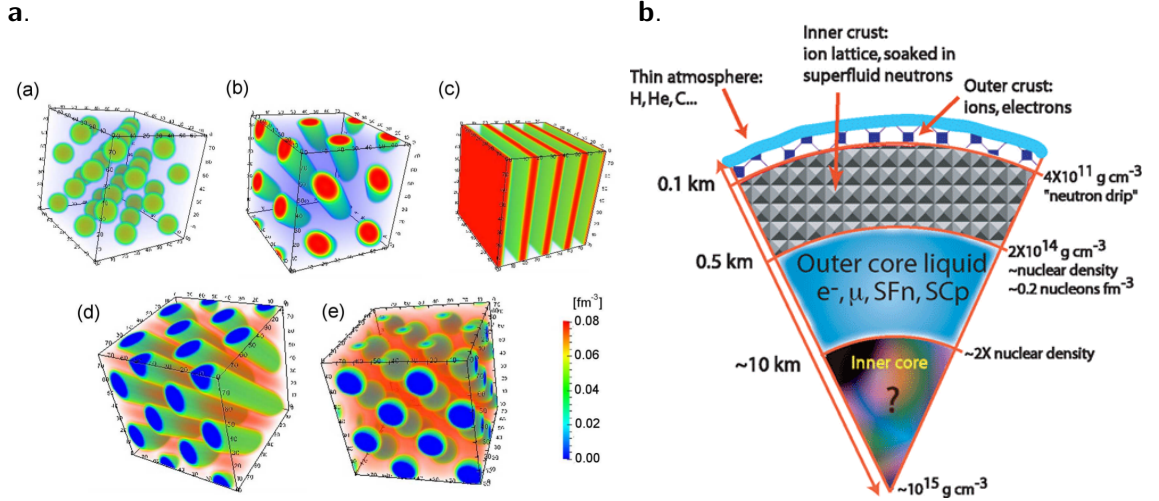


Figure 2.1:

Inset **a.** — plots of proton density distributions in symmetric dense nuclear matter published in work of M. Okamoto, T. Maruyama, K. Yabana, and T. Tatsumi [32] (for details see the cited paper). Different "pasta" structures revealed.

Inset **b.** — structure of neutron star interior, the picture taken from site of B. Link, <http://www.physics.montana.edu>.

Inside neutrons stars gravitational pressure causes such a growth of matter density that electrons start to form relativistic gas. Their Fermi energy exceeds neutron-proton mass difference and inverse β decay ($p + e^- \rightarrow n + \nu$) becomes energetically preferable to normal β decay. The inverse decay creates very neutron rich nuclei. As a consequence , for baryon density higher than neutron drip density $\rho_{drip} \gtrsim 4 \cdot 10^{11} \text{ g cm}^{-3}$ [29, 33] neutrons leak out from the nucleus (a significant fraction of them is unbounded) and form uniform gas of neutron surrounding nuclear impurities. This process is sometimes named **neutronization**.

Under the restriction of thermodynamical equilibrium, the nuclear matter, due to balance between β decay and inverse process, have to fullfil the following condition:

$$\delta\mu = m_e c^2 + \mu_e + m_p c^2 + \mu_p - m_n c^2 - \mu_n = 0 \quad (2.9)$$

called the **beta equilibrium condition**³.

Utilizing beta equilibrium condition one can investigate structure of neutron star below neutron drip point. One of methods exploited in research is Wigner-Seitz cells approach described in sec. 2.1.4.

As it was mentioned, just below this point nuclear matter is thought to consist of neutrons surrounding nuclei. Since neutron stars are cold objects, it turns out that in some regions

³Assumptions that during the evolution beta and thermodynamic equilibria are conserved is called **cold catalyzed matter hypothesis**. It was shown in chap. 9 of ref. [34] that this conjecture guarantees the stress-energy density tensor (2.2) to fulfill perfect fluid postulate providing theory to be self-consistent.

neutron matter can form a superfluid. The region of coexistence various localized nuclear defects (called impurities in this thesis) and superfluid background is called the neutron star crust.

Deeper inside the star, in outer core, nuclei are destroyed due to degeneration of neutron liquid under gravitational pressure and increase of Coulomb force magnitude (connected with compression of impurity lattice). This exotic phase of nuclear matter is called *nuclear pasta*. A numerical simulations revealing unusual structures in dense nuclear matter were observed by several research groups, i. e. [32]. See fig. 2.1, inset **a**. A framework of Wigner-Seitz cells expires in this limit, because there are no more distinct nuclei.

In inner core gravitational pressure effects are so huge, that no reliable theory is available leading to number of speculations, including creation of hyperon and quark matter. This topic will be omitted, because is considered to be irrelevant to further part of the thesis. In inset **a** of fig. 2.1 schematic structure of the neutron start is shown.

More emphasis can be placed on superfluidity in the neutron star crust. Calculations of neutron-protons pairs scattering phase shifts⁴ revealed that for densities expected in the neutron star crust (i.e. region where neutron form dilute gas), the s-wave interaction is of most importance (see fig. 2.2). Then, reasonable expectation is that background neutrons form s-wave superfluidity (i.e. Cooper pairs condensate in zero momentum state). Under this assumption, framework of Superfluid Local Density Approximation can be exploited (see sec. 3.2.2). For purpose of this thesis assumption of the s-wave superfluidity enables for utilization of the BCS coherence length formula to estimate size of the vortex core radius. It is very important parameter in Vortex Filament Model, see sec. 3.1.1 and sec. 3.4.3.

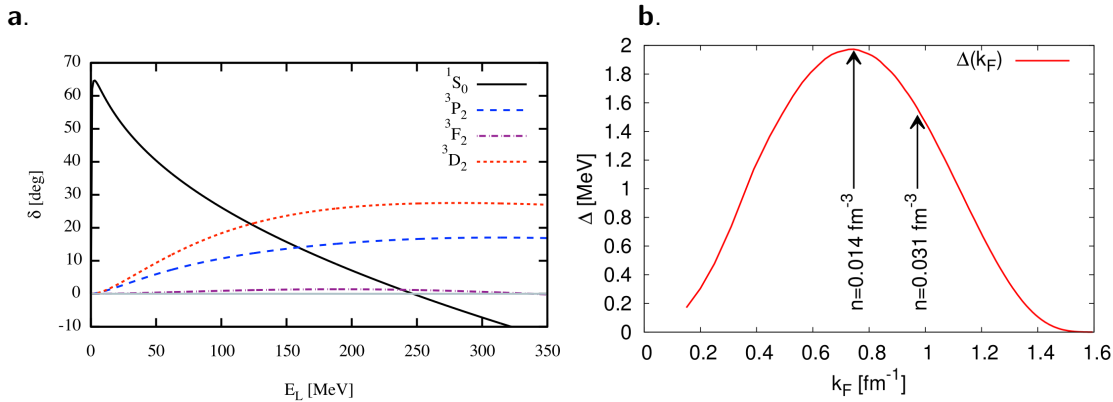


Figure 2.2:

Inset **a**. — The nucleon-nucleon scattering phase shifts as a function of energy (can be compared to Fermi energy and thus related to density). Analysis of the plot shows that at densities corresponding to the case of neutron star crust the most important is the s-wave channel of neutron-neutron interaction. Plot taken from review paper of B. Haskell and A. Sedrakian [12].

Inset **b**. — s-wave paring gap in uniform neutron matter. Clearly, up to Fermi momentum $k_F < 1.45 \text{ fm}^{-1}$ (densities smaller than 0.1 fm^{-3}) the matter is superfluid. The arrows indicate two cases for which the TDSLDA simulations where performed (see sec. 4.1.2). Plot taken from work of G. Włazłowski et al. [20].

⁴For quantum theory of scattering see chap. 19 in book of R. Shankar [35].

2.1.4 Spherical Wigner-Seitz cells method for neutron star matter

When determining microscopic properties of nuclear matter, with given isospin asymmetry, a concept of spherical Wigner-Seitz (WS) cells[36] is commonly utilized, since a seminal paper by J.W. Negele and D. Vautherin[37]. The method involves solving many body Schrödinger equation for protons and neutrons using (originally) Hartree-Fock approximation or (recently) more precise approximations (i.e. Hartree-Fock-Bogoliubov) assuming spherically symmetric geometry. The radius of the spherical cells is determined by beta equilibrium condition — number of protons Z and neutrons N can be found by looking for values of Z, N where $\delta\mu$ in (2.9) is changing sign. The cell is assumed to be electrically neutral (equal number of protons and electrons) and the problem of boundary conditions was discussed in papers [37, 38] and further description of this problem is beyond the topic of this thesis. Comparison of a number of different quantum approximations and semi-classical models for calculations of Wigner-Seitz cell radii is presented in a review paper by N. Chamel and P. Haensel [33].

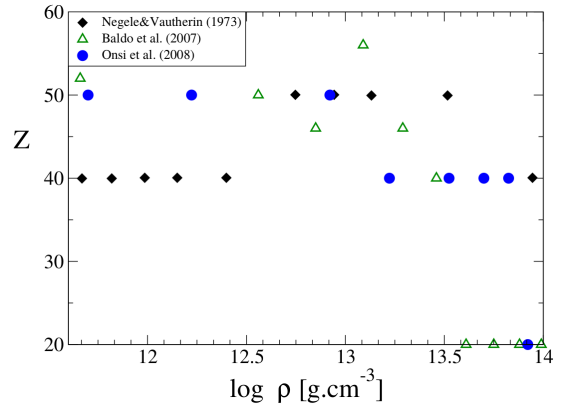


Figure 2.3: Number of protons inside Wigner-Seitz cell fulfilling condition (2.9) with respect to density of baryonic matter. It can be considered as mean number of protons inside nuclear impurity in neutron star crust. Different approaches compared.

For the purpose of this thesis only case of nuclei with $Z=50$ was considered (see sec. 4.1.2 and description of research in work of G. Włazłowski et al. [20]).

Plot taken from paper of N. Chamel and P. Haensel [33].

In this thesis, I focus only on situations where protons create localized structures called impurities, immersed in sea of neutrons. Then the WS method gives information about volume per single impurity. However, these calculations cannot give us information on spatial geometry impurities distribution, because interaction between neighbouring cells is neglected in such a framework. Nevertheless, physical properties of system calculated in single WS cell should be the same as physical properties for whole real system but averaged over its volume. The geometry has to be obtained by means of other approaches, for example semi-classical considerations or density functional theories (i. e. see paper of P. Magierski and P.-H. Heenen [39]). This type of considerations show that impurities typically form f.c.c. or b.c.c. lattice (depending on density). This two scenarios will be studied in my thesis.

In order to extract lattice spacing (which is geometry dependent quantity), author of the thesis assumed that number of protons and neutrons in spherical WS cell is the same as number of

protons and neutrons in f.c.c. or b.c.c. primitive cell. Volume of b.c.c./f.c.c Wigner-Seitz cell is volume of primitive cell divided by number of distinct nodes in primitive cell. Using this relation we can estimate lattice constant for assumed geometry of lattice. This gives:

$$V_{WS}^{spherical} = V_{WS}^{b.c.c.} = a^3/2 \quad V_{WS}^{spherical} = V_{WS}^{f.c.c.} = a^3/4 \quad V_{WS}^{spherical} = \frac{4}{3}\pi R_{WS}^3$$

$$a^{b.c.c.} = \sqrt[3]{\frac{8}{3}\pi R_{WS}} \quad a^{f.c.c.} = \sqrt[3]{\frac{16}{3}\pi R_{WS}} \quad (2.10)$$

In the figure 2.5 a dependence of spherical WS cell radius on mean baryon density inside the cell is shown. A smoothed interpolation⁵ of simulated data was performed to facilitate determination of spherical WS cell radius for neutron background densities of 0.014 fm^{-3} and 0.031 fm^{-3} . Large discrepancy in estimates of Wigner-Seitz cell size in previous works was noticed, whereas nuclear spacing possibly has noticeable influence on magnitude of force acting on a length element of vortex line. Thus influence of WS cell radius on vortex motion is tested in numerical simulation, see chap. 6.

To obtain the relation between neutron background densities and mean baryon density inside a WS cell, the data from paper [43] was utilized. Neutron background density of 0.014 fm^{-3} is obtained to correspond to baryon mass density $2.8 \cdot 10^{13} \text{ g} \cdot \text{cm}^{-3}$, whilst for 0.014 fm^{-3} baryon mass density is approximately equal $6.0 \cdot 10^{13} \text{ g} \cdot \text{cm}^{-3}$. Results of the article [43] are visualized in fig. 2.4. For comparison normal nuclear mass density is approximately equal $2.8 \cdot 10^{14} \text{ g} \cdot \text{cm}^{-3}$, which corresponds to density of baryonic particles 0.16 fm^{-3} .

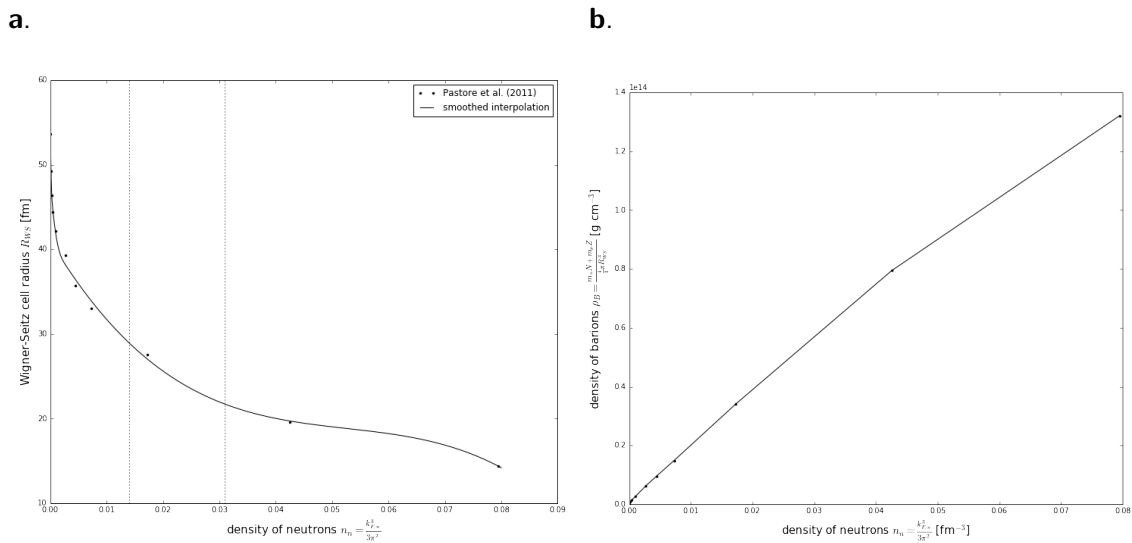


Figure 2.4: WS cell radius (inset a., dotted lines indicate neutron background density of 0.014 fm^{-3} and 0.031 fm^{-3}) and baryon mass density (inset b.) with respect to neutron background density. Data taken from article [43] and solid lines obtained with usage of smoothed interpolation of data points.

⁵Interpolation with function `scipy.interpolate.splrep` with nonzero parameter s [40] will be called smoothed interpolation. If s is directly not given in text, the value $s = m - \sqrt{2m}$ will be assumed, where m is number of data points. The algorithm exploited was invented by P. Dierckx [41, 42].

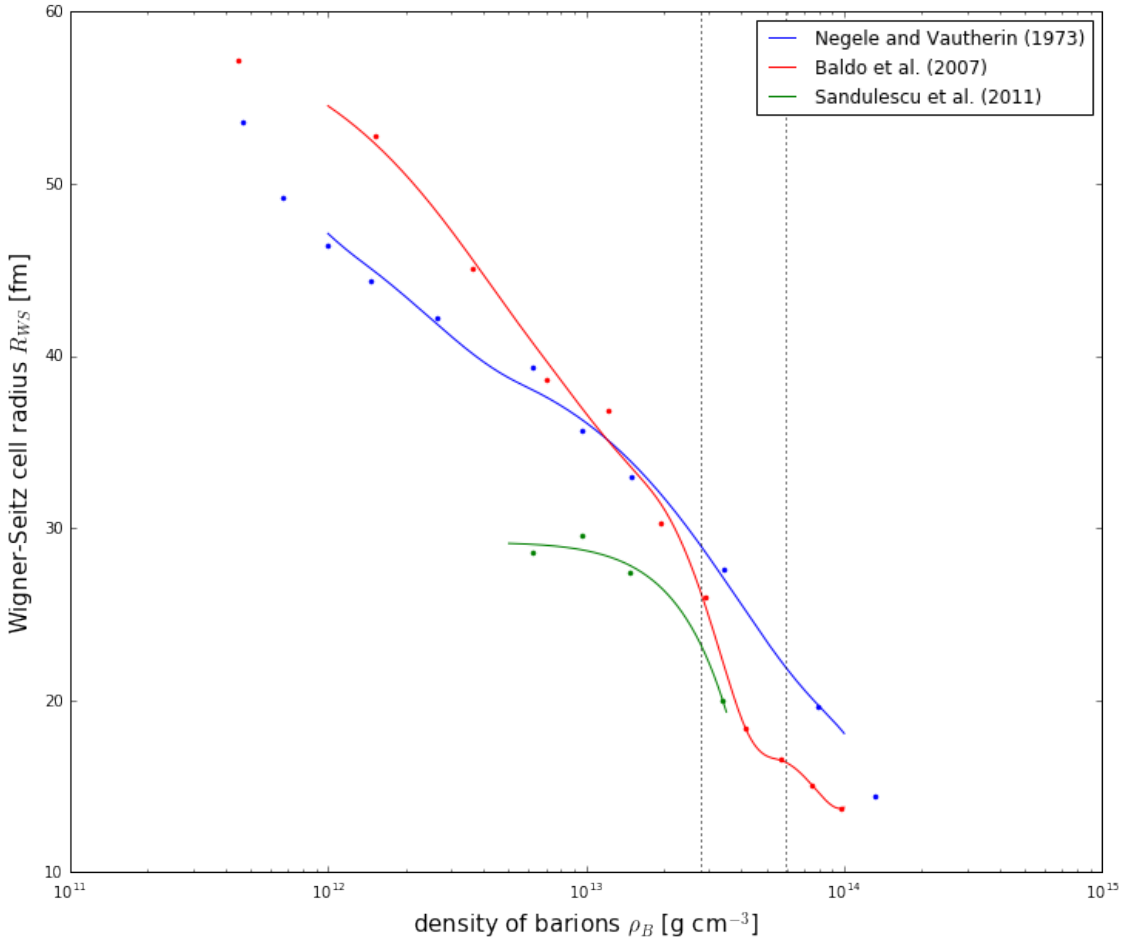


Figure 2.5: Comparison of results from simulations of asymmetric nuclear matter in Wigner-Seitz cells representing dependence of cell radius to mean baryon density in beta equilibrium presented by different groups. Data taken from [37],[38] and [44] (case of HFB approximation with isovector-isoscalar pairing forces). Solid lines are given by smoothed interpolation of data-points obtained in papers. Two dotted vertical lines represent baryon densities according to values neutron background densities of 0.014 fm^{-3} and 0.031 fm^{-3} respectively (the relation between neutron background densities and mean baryon density was calculated using data from paper [43]).

2.2 Neutron star glitches

2.2.1 Rotation of neutron star crust

The periods of rotation of neutron star can be measured by astronomical observations of pulsars, see i. e. paper by R. N. Manchester and V. Radhakrishnan [16]. Example of results of such observations with explanation is provided in fig. 2.6.

It is known that rotation period of a neutron star is slowly decreasing, see general discussion in sec. 1.2.

A robust estimate of star crust velocity can be utilized, according to work of M. Antonelli and P. Pizzochero [45]:

$$v_p = \Omega_p x \quad (2.11)$$

where x is distance from star rotation axis (see fig. 2.7) and angular velocity is connected to period of star rotation by $\Omega_p = 2\pi/P$. The velocity v_p can be considered as a linear velocity of surface of the star and author of the thesis does not rely on this estimate in case of velocity of lattice of impurities discussed in sec. 2.1.4. Thus a velocity of impurity lattice is treated as unknown in the rest part of the thesis, which affected on choice of frame of reference of simulations — see sec. 5.4.3.

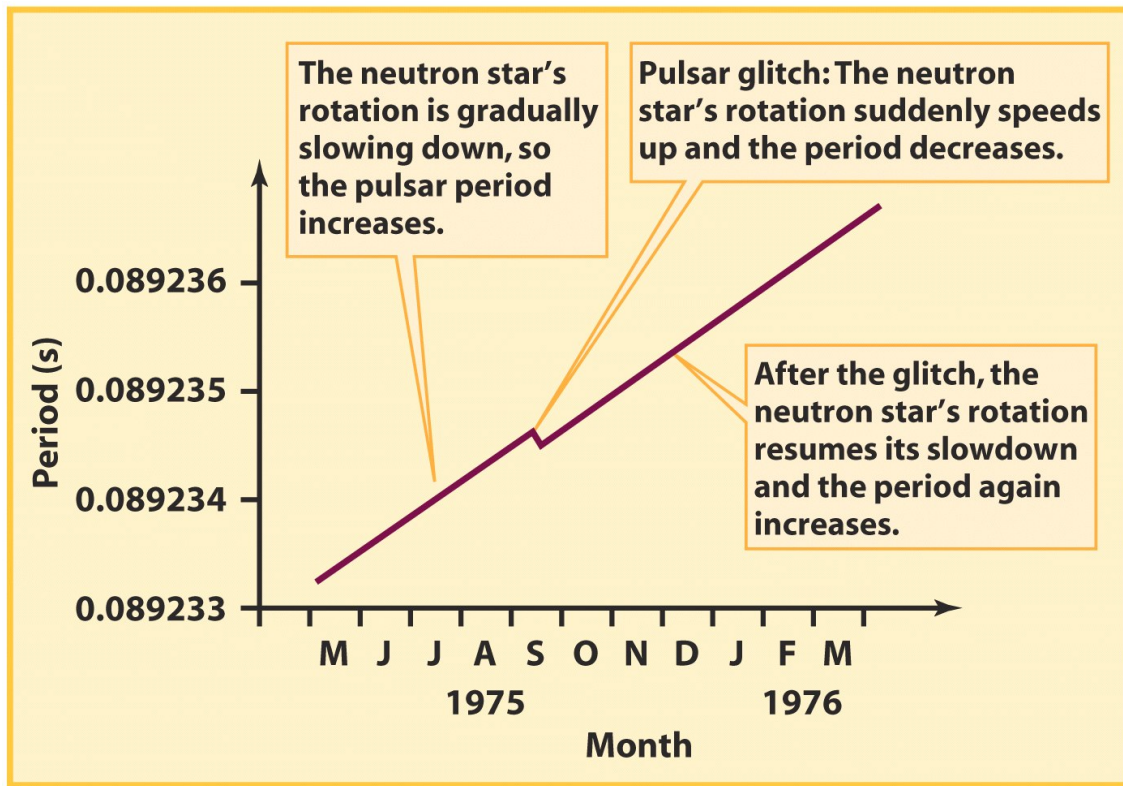


Figure 2.6: Changes of rotation period T of a neutron star. Picture taken from website <https://briankoberlein.com/2014/05/30/glitch-anti-glitch/> (visited on 29.01.2018).

2.2.2 Origin of glitches

In fig. 2.7 a schematic picture of neutron star interior, in context of the glitch studies, is presented. Two main components are highlighted: outer crust that rotates as rigid body (blue area) and superfluid interior filled with quantum vortices (yellow lines). As the outer crust radiates energy its angular velocity, and thus angular momentum, slowly decreases. Note however, that this cannot happen for superfluids, where the angular momentum can be only sustained in form of quantum vortices and vortices are protected by quantization rules, see (3.15). The angular momentum of superfluid is proportional to number of quantum vortices. Note that vortices can only be ejected outside the system (to the rust) or injected from outside (from the crust). If the vortices can move freely, then two reservoirs can always exchange angular momentum: the crust by changing rotation frequency while the superfluid component by changing number of vortices in it. It is conjectured that vortices can be pinned to nuclear defects in the start crust, and the angular momentum exchange cannot take place easily., see work of P. W. Andersson and N. Itoh [17]. However, mutual tension between outer part of the crust and lattice of pinned vortices can cause catastrophic events (from time to time) that result in global change of the vortex lattice configuration. The phenomenon is thought to be similar to avalanches, and during this rapid event some vortices are ejected from the interior and transfer its angular momentum to the outer crust. For an observer it is visible as a glitch, i.e. rapid increase of rotation frequency of the star. Note that in this rough explanation of the glitch phenomenon, the vortex pinning mechanism plays central role. Most of studies in this field is trying to verify if pinning indeed can take place inside the neutron star.

For references of theories of neutron star glitches see papers of M. Antonelli, P. Pizzochero [45] and of B. Haskell and A. Melatos [11].

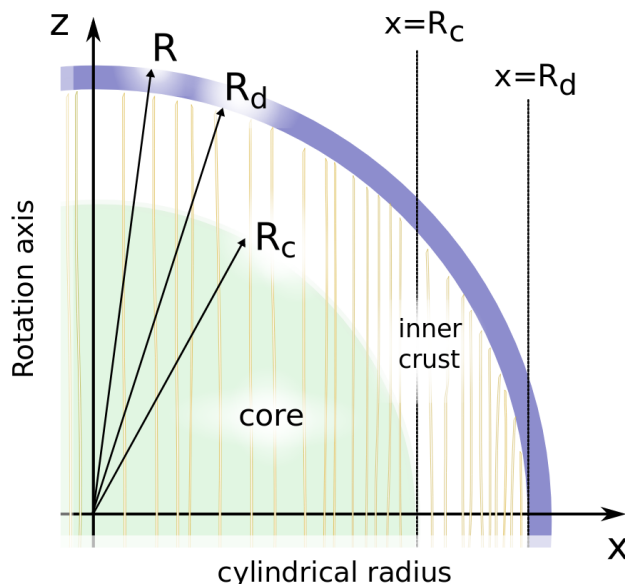


Figure 2.7: Schematic picture of neutron star interior, in context of the glitch studies taken from work of M. Antonelli and P. Pizzochero [45].

2.2.3 Intervortex spacing

One of the parameters that must be taken into consideration when investigating hydrodynamics of neutron stars is mean distance between superfluid vortices.

In further part of the thesis an expression, appearing in papers of B. Haskell [46, 11]:

$$d_V = 4 \cdot 10^{-4} \sqrt{\frac{P}{1ms}} \text{ cm}, \quad (2.12)$$

will be used for various estimates. Taking periods of rotation of a neutron star as 1.4 ms and 8.5 s and exploiting the formula above one can calculate **intervortex spacing** d_V to be greater than tens of nanometers.

2.2.4 Energy of two rectilinear vortices in Vortex Filament Model

In this section Vortex Filament Model derived in sec. 3.3.1 is utilized for the case of two rectilinear vortices. Assuming vortex length $L \approx d_V$ the energy of interaction between vortices decreases logarithmically (see fig. 2.8), but simultaneously $\lim_{d_V \rightarrow 0} E_V/L = \infty$ and effective core radius for real vortex fulfills $d_V \gg a_0$. The rectilinear vortex lines i,j are pointed by vectors $s_i(z) = [0, R/2, z]^T$, $s_j(z') = [0, -R/2, z']^T$ and for calculations following formula for mutual energy [47, 48] was used:

$$\begin{aligned} E_{ij}(d_V) &= \frac{\rho\kappa^2}{8\pi} \int_{\mathcal{L}_i} dz \int_{\mathcal{L}_j} dz' \frac{\hat{t}_i(z, t) \cdot \hat{t}_j(z', t)}{|s(z, t) - s(z', t)|} = \frac{\rho\kappa^2}{8\pi} \int_0^L \int_0^L \frac{dz dz'}{\sqrt{(z - z')^2 + d_V^2}} = \\ &= \frac{\rho\kappa^2}{4\pi} \left[d_V - \sqrt{L^2 + d_V^2} + L \tanh^{-1} \left(\frac{L}{\sqrt{L^2 + d_V^2}} \right) \right] \end{aligned} \quad (2.13)$$

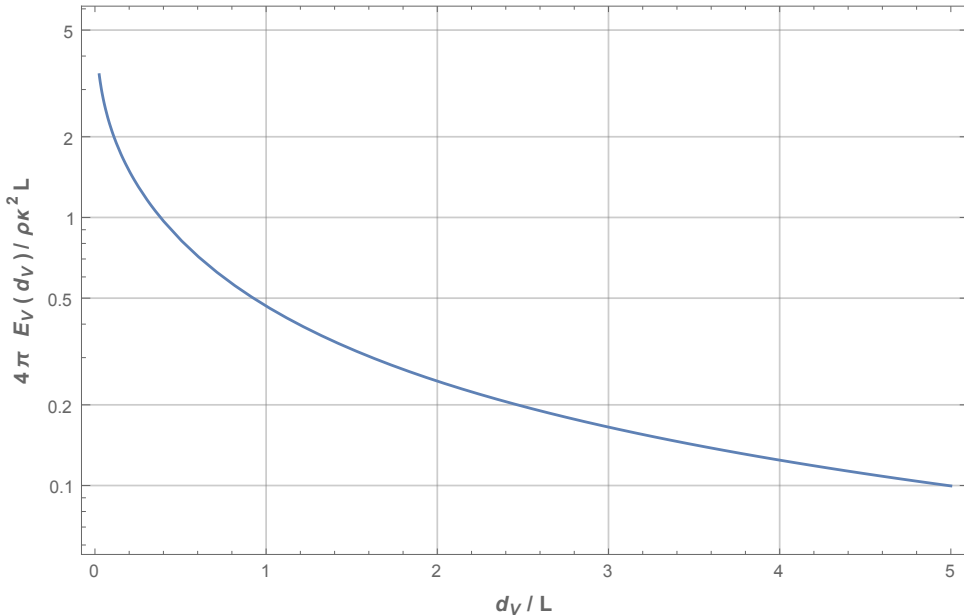


Figure 2.8: Estimate of mutual interaction energy of two rectilinear vortices $\frac{4\pi}{\rho\kappa^2 L} E_V(d_V) = \frac{d_V}{L} - \sqrt{1 + \frac{d_V^2}{L^2}} + \tanh^{-1} \left(\frac{1}{\sqrt{1 + \frac{d_V^2}{L^2}}} \right)$.

The result obtained in the fig. 2.8 and estimate for d_V in sec. 2.2.3 are justifying usage of single vortex line in numerical simulations in chap. 5 and 6.

Chapter 3

Theoretical description of superfluids

3.1 Microscopic theory of superfluidity

The understanding of superfluidity phenomena in fermionic system at low temperatures is expressed by Bardeen-Cooper-Schrieffer (BCS) theory[49]. The key concept of the BCS theory is Cooper pairing, i.e. appearance of correlations between particles having time reversed quantum numbers. It can be postulated as a consequence of Kramers' degeneration theorem.

In case of half-integer spin and momentum for state $|k \uparrow\rangle$ a time-reversed state has momentum in opposite direction and reversed spin $|-\mathbf{k} \downarrow\rangle$ and the particles can occupy these two eigenstates if it is energetically preferred from other states. L. N. Cooper proved that providing arbitrarily weak attractive interaction between particles near the Fermi surface there must be an particle with opposite spin and momentum[50]. Such a coupled system of two fermions is called Cooper pair. Operator $\hat{b}_k = \hat{c}_{\mathbf{k}\uparrow}^\dagger \hat{c}_{-\mathbf{k}\downarrow}^\dagger$ can be considered as creation operator of Cooper pairs.

Within BCS theory wavefunction of a fermionic superfluid (or superconducting) system is postulated in form

$$|\Psi_{BCS}\rangle = \prod_k \left(u_k + v_k \hat{c}_{\mathbf{k}\uparrow}^\dagger \hat{c}_{-\mathbf{k}\downarrow}^\dagger \right) |0\rangle \quad (3.1)$$

Coefficients v_k can be interpreted as probability amplitudes of existence of a Cooper pair at momentum \mathbf{k} and u_k is probability amplitude that there is no Cooper pair.

Since in finite systems, like nucleus the continuous translational invariance is destroyed, momentum \mathbf{k} is not well-defined quantum number and no longer can describe pure state of a particle in a many-body system. Generalization to arbitrary single particle states is known as Bogoliubov-de Gennes (BdG) equations in theory of electronic superconductivity or time-dependent Hartree-Fock-Bogoliubov (HFB) equations in nuclear theory.

Coefficients u_k and v_k are obtained by applying Ritz variational principle to many-fermion Hamiltonian. For BCS theory resulting equations have form:

$$\begin{pmatrix} h & \Delta \\ \Delta^* & -h^* \end{pmatrix} \begin{pmatrix} u_k \\ v_k \end{pmatrix} = E_k \begin{pmatrix} u_k \\ v_k \end{pmatrix} \quad (3.2)$$

where $h = -(\hbar^2/2m)\nabla^2 - \mu$ is the single-particle Hamiltonian, μ - chemical potential and Δ is the order parameter, and in the BCS theory 2Δ is energy needed to brake a Cooper pair. If the order parameter vanishes $\Delta = 0$, then the BCS theory is equivalent to Hartree-Fock theory, which approximate interacting system by non-interacting particles moving in averaged field, generated by all other particles. For this reason, it refereed that the BCS theory approximates the interacting system by set of non-interacting quasiparticles.

3.1.1 Coherence length

Coherence length ξ is a characteristic length at which the order parameter can change. For example, the vortex solution is characterized by vanishing order parameter inside the vortex core, see fig. 3.1. Then, the coherence length contains information about size of the vortex. It has to be noted, that the coherence length is not precisely equal to effective vortex radius core discussed in sec. 3.3.1.

In case of BCS theory the lenght is given by [51]:

$$\xi_{BCS} = \frac{\hbar v_F}{\pi \Delta} = \frac{\hbar^2 c^2 k_F}{\pi \Delta m_n c^2} \quad (3.3)$$

Direct calculations for neutron star crust case gives $\xi_{BCS} = 2.47$ fm for $\rho = 0.014$ fm $^{-3}$ and $\xi_{BCS} = 4.27$ fm for $\rho = 0.031$ fm $^{-3}$.

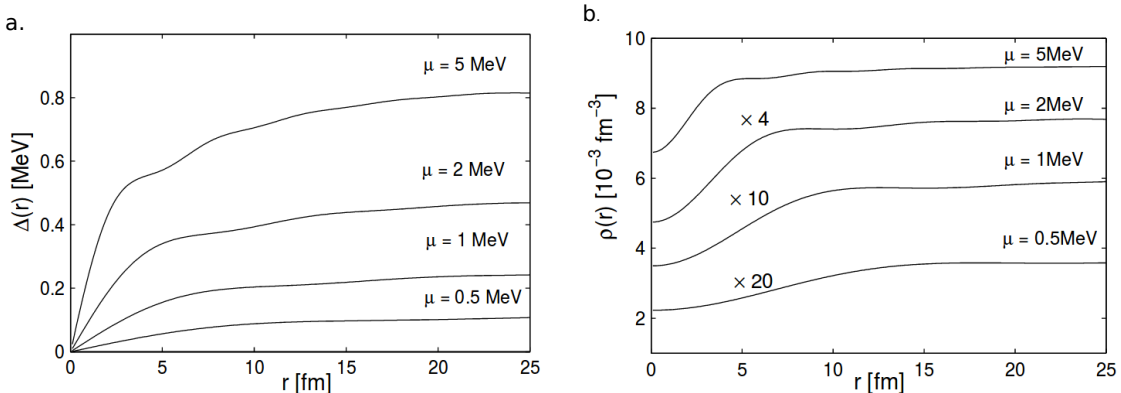


Figure 3.1: Vortex structure in neutron matter for different values of chemical potential μ , which is related to Fermi energy and thus to density of neutron matter. Comparison of the of order parameter (inset a.) and the matter density (inset b.) shows vanishing of the superfluid component in the core, which is filled by the normal component. Plots taken from work of A. Bulgac and Y. Yu [52].

3.2 Density functional approach and Superfluid Local Density Approximation.

3.2.1 Basics of density functional theory

For a system on N quantum particles described by wavefunction $\Phi(\mathbf{r}_1, \sigma_1, \mathbf{r}_2, \sigma_2, \dots, \mathbf{r}_N, \sigma_N)$ (\mathbf{r}_i - position operator in positions representation, σ_i - spin of a particle) one to one mapping onto density

$$n(\mathbf{r}) = \sum_{\sigma} \int d^3r_2 d^3r_3 \dots d^3r_N \Phi^*(\mathbf{r}, \sigma_1, \dots, \mathbf{r}_N, \sigma_N) \Phi(\mathbf{r}, \sigma_1, \dots, \mathbf{r}_N, \sigma_N) \quad (3.4)$$

can be introduced. This is consequence of Hohenberg-Kohn theorems, presented below, see [53] for reference). Since the mapping is one to one, the density contains as much information as the full wavefunction Φ .

Theorem 1. Hohenberg-Kohn theorem

Density of particles in the ground state $n(\mathbf{r})$ confined in external potential $V_{ext}(\mathbf{r})$ defines this potential uniquely.

Recall that the Hamiltonian can be written as $\hat{H} = \hat{T} + \hat{V} + V_{ext}$, where \hat{T} is kinetic energy operator, \hat{V} is interaction and V_{ext} is the external potential. The interaction \hat{V} defines type of particles, for example it is Coulomb interaction for electrons. The theorem allows to construct logical chain for given type of particles: $n(\mathbf{r}) \rightarrow V_{ext} \rightarrow \hat{H} \rightarrow \Phi$. It means that the wavefunction is a functional of density $\Phi = \Phi[n]$ and more general: each observable is a functional of density $O[n] = \langle \Phi[n] | \hat{O} | \Phi[n] \rangle$. Energy of the system is a case of special importance. It can be always written as

$$E[n] = \langle \Phi[n] | \hat{H} | \Phi[n] \rangle = F[n] + \int n(\mathbf{r}) V_{ext}(\mathbf{r}) d\mathbf{r}, \quad (3.5)$$

where $F[n]$ is a universal functional that depends only on type of particles (in the same sense as the interaction \hat{V}).

Theorem 2. Hohenberg-Kohn theorem

Density that minimises the energy functional $E[n]$ is the exact groundstate density.

This theorem is direct consequence of Ritz variational principle. Practically, it means that minimization of the functional $E[n]$ is equivalent to solving the Schrödinger equation.

The main problem is that the energy functional is not known (contrary to the interaction \hat{V}), and there is no prescription how to derive it. It must be somehow constructed. Typically, it is postulated in some form and adjusted to reproduce known set of results, either derived theoretically or experimentally.

For more details concerning the density functional approach we refer the interested reader to book of K. Burke [53].

3.2.2 Superfluid Local Density Approximation

The Superfluid Local Density Approximation (SLDA) for strongly interacting Fermi systems is based on the energy density functional (EDF) of generic form:

$$E = \int \mathcal{H}[\tau(\mathbf{r}), n(\mathbf{r}), \nu(\mathbf{r}), \dots] d^3\mathbf{r} + \int V_{ext}(\mathbf{r})n(\mathbf{r}) d^3\mathbf{r}, \quad (3.6)$$

where \mathcal{H} is the “universal” energy density functional which depends on local densities only, like kinetic density $\tau(\mathbf{r})$, normal density $n(\mathbf{r})$ and anomalous density $\nu(\mathbf{r})$. $V_{ext}(\mathbf{r})$ represents an external potential. Next, the densities are parametrized by functions $\{u_n(\mathbf{r}), v_n(\mathbf{r})\}$ as:

$$n(\mathbf{r}) = \sum_n |v_n|^2(\mathbf{r}), \quad \tau(\mathbf{r}) = \sum_n |\nabla v_n|^2(\mathbf{r}), \quad \nu(\mathbf{r}) = \sum_n u_n(\mathbf{r}) v_n^*(\mathbf{r}). \quad (3.7)$$

To find configuration with the lowest energy, one needs to minimize energy density functional (3.6) with respect to functions $\{u_n(\mathbf{r}), v_n(\mathbf{r})\}$. It turns out that resulting equations have the same generic form as the BCS equations (3.2), where $h = -\frac{\hbar^2}{2m} \nabla^2 + \frac{\delta E}{\delta n} + V_{ext} - \mu$ and $\Delta = -\frac{\delta E}{\delta \nu^*}$. It is seen, that in the SLDA approach the problem of interacting particles is mapped onto problem of noninteracting quasiparticles, smaly as in Kohn-Sham approach.

Equations of motion can be easily obtained from (3.2) where we replace $E_k \rightarrow i\hbar \frac{\partial}{\partial t}$. It turns out that the evolution of fermions is given by equations very similar to time-dependent extension of BdG or HFB equations. They have form:

$$i\hbar \frac{\partial}{\partial t} \begin{pmatrix} u_n(\mathbf{r}, t) \\ v_n(\mathbf{r}, t) \end{pmatrix} = \begin{pmatrix} h(\mathbf{r}, t) & \Delta(\mathbf{r}, t) \\ \Delta^*(\mathbf{r}, t) & -h^*(\mathbf{r}, t) \end{pmatrix} \begin{pmatrix} u_n(\mathbf{r}, t) \\ v_n(\mathbf{r}, t) \end{pmatrix}. \quad (3.8)$$

Note that, in case of nuclear problems one has solve these equations for protons and neutrons. This is very complicated problem, because the problem is represented by system of coupled (through densities (3.7)) complex nonlinear time-dependent 3D partial differential equation. Number of variables used in simulation of TDSLDA equations is

$$\underbrace{N_x N_y N_z}_{\text{grid size}} \cdot 2 \cdot N_{\text{components}} \cdot N_{\text{states}},$$

For nuclear systems $N_{\text{components}} = 2$ (neutrons and protons). The complexity arises from large number of states which need to be included into description. Precisely, in TDSLDA we must evolve states up to energy cut-off E_c which is typically a few times larger than Fermi energy of protons or neutrons ϵ_F . While the spectrum of the states below the Fermi energy is discrete, above it is continuum. In practical implementation the continuum becomes discretized due to discretization of the space, and obtained number of states is of the same order as number of grid points.

In work [20] authors neglected spin-orbit contribution to the nuclear interaction in order to reduce of the computational complexity, which was necessary to run simulations on available supercomputers.

3.3 Vortex Filament Model

3.3.1 Vortex Filament Model derivation

Vortex Filament Model (VFM) is a hydrodynamical model describing motion of a vortex line — a line whose direction is consistent with the vorticity ω of the vector field (as a definition of vorticity look at eq. (3.9)).

Despite historically it was introduced in context of classical hydrodynamics, a concept of vortex line is well-defined rather in quantum hydrodynamics. In classical description a vortex line is highly unstable due to any perturbations, while in quantum systems the line is a topological defect of the order parameter that is protected against decay by quantum rules. Precisely, topological quantum numbers have to be conserved so the vortex line can be destroyed only when sufficiently high energy perturbation is provided. Due to the fact that topological singularity in phase (of the order parameter) is point-like we can idealize vortex line as a infinitely thin filament and this leads to Vortex Filament Model. In the following section a derivation of this model will be discussed.

Inviscid and incompressible fluid described by the Euler equation[54] leads to simple formula for vortex line motion. Under the constraints fulfilled by this equation a superfluid velocity field with natural boundary conditions (field disappears in infinity) can be decomposed into divergence-free and rotation-free part¹ and a following description of velocity field induced by vortex line can be provided [56]:

$$\mathbf{v}_{superfluid} = \underbrace{\mathbf{v}_{ind}}_{\text{induced by vortex}} + \mathbf{v}_{external} \quad \begin{aligned} \nabla \times \mathbf{v}_{ind} &= \boldsymbol{\omega} & \nabla \times \mathbf{v}_{ext} &= 0 \\ \nabla \cdot \mathbf{v}_{ind} &= 0 & \nabla \cdot \mathbf{v}_{ext} &= \phi \end{aligned} \quad (3.9)$$

In further part of the work external flow vector \mathbf{v}_{ext} is assumed to be constant in both, time and space.

Incompressibility $\nabla \cdot \mathbf{v}_{ind} = 0$ implies existence of a vector potential of field induced by vortex line:

$$\mathbf{v}_{ind} = \nabla \times \mathbf{A} \quad \nabla \cdot \mathbf{A} = 0, \quad (3.10)$$

which is connected with vorticity with relation:

$$\boldsymbol{\omega} = \nabla \times \mathbf{v}_{ind} = \nabla \times \nabla \times \mathbf{A} = -\nabla^2 \mathbf{A} + \underbrace{\nabla \nabla \cdot \mathbf{A}}_0. \quad (3.11)$$

Using Green's function for Laplace operator and natural boundary conditions for the vector field one can express the vector potential and the velocity by the vorticity with following formulas:

$$\mathbf{A}(\mathbf{r}) = \frac{1}{4\pi} \int_{\mathbb{R}^3} \frac{\boldsymbol{\omega}(\mathbf{r}')}{|\mathbf{r} - \mathbf{r}'|} d^3 r' \quad (3.12)$$

¹Such decomposition is called Helmholtz-Hodge decomposition and in general an additional harmonic component describing a flow of fluid between boundaries must be considered [55]. Here it vanishes due to natural boundary conditions.

$$\mathbf{v}_{ind}(\mathbf{r}) = \frac{1}{4\pi} \int_{\mathbb{R}^3} \boldsymbol{\omega}(\mathbf{r}') \times \frac{\mathbf{r} - \mathbf{r}'}{|\mathbf{r} - \mathbf{r}'|^3} d^3 r \quad (3.13)$$

Moreover, assumption that vortex line is infinitesimally thin and massless leads to conclusion that vorticity $\boldsymbol{\omega}$ is equal zero everywhere except singularity on vortex line²:

$$\boldsymbol{\omega}(\mathbf{r}) = \kappa \int_{\mathcal{L}} \hat{\mathbf{t}}(\zeta) \delta^3(s(\zeta) - \mathbf{r}) d\zeta \quad \begin{matrix} \text{integration over vortex line} \\ \implies \end{matrix} \quad \mathbf{v}_{ind}(\mathbf{r}, t) = \frac{\kappa}{4\pi} \int_{\mathcal{L}} \frac{(s(\zeta, t) - \mathbf{r}) \times s'(\zeta, t)}{|s(\zeta, t) - \mathbf{r}|^3} d\zeta \quad \mathbf{A}(\mathbf{r}, t) = \frac{\kappa}{4\pi} \int_{\mathcal{L}} \frac{\hat{\mathbf{t}}(\zeta, t)}{|s(\zeta, t) - \mathbf{r}|} d\zeta \quad (3.14)$$

where $\hat{\mathbf{t}}$ is tangent vector to vortex line (see appendix A.2 for disambiguation), s is a vector pointing element on a vortex line \mathcal{L} and scalar factor κ is a circulation of velocity field.

The circulation is evaluated on contour \mathcal{C} around a vortex line and according to Feynman-Onsager quantization condition [57]:

$$\kappa = \oint_{\mathcal{C}} \mathbf{v} \cdot d\mathbf{l} = 2\pi \frac{\hbar}{m} \ell, \quad \ell \in \mathbb{Z} \quad (3.15)$$

where m is a mass of a particle forming superfluid, in case of neutrons in star crust one have to consider mass of Cooper pair, thus $m = 2m_n$.

Formula for the velocity field is in complete analogy with Biot-Savart law for a wire with electric current and thus is also reffered as Biot-Savart law. More exploitable form is:

$$\mathbf{v}_{ind}(\mathbf{r}, t) = \frac{\kappa}{4\pi} \int_{\mathcal{L}} \frac{(\mathbf{s}(\zeta, t) - \mathbf{r}) \times \mathbf{s}'(\zeta, t)}{|\mathbf{s}(\zeta, t) - \mathbf{r}|^3} d\zeta = \frac{\kappa}{4\pi} \int_{-\infty}^{\infty} \frac{(\mathbf{s}(z, t) - \mathbf{r}) \times \frac{ds}{dz}(z, t)}{|\mathbf{s}(z, t) - \mathbf{r}|^3} dz \quad (3.16)$$

Assuming constant mass density of the fluid, the energy of vortex³ is given by equation⁴:

$$E_V = \int_{\mathbb{R}^3} \frac{1}{2} \rho(\mathbf{r}) \mathbf{v}_{ind}^2 d^3 r \approx \frac{\rho}{2} \int_{\mathbb{R}^3} \boldsymbol{\omega}(\mathbf{r}) \cdot \mathbf{A}(\mathbf{r}) d^3 r = \frac{\rho \kappa^2}{8\pi} \int_{\mathcal{L}} dz \int_{\mathcal{L}} dz' \frac{\hat{\mathbf{t}}(z, t) \cdot \hat{\mathbf{t}}(z', t)}{|\mathbf{s}(z, t) - \mathbf{s}(z', t)|} \quad (3.17)$$

Note that energy of the vortex line does not depend on velocity of the line, since we assume that vortices are massless.

More detailed derivation of discussed formulas can be found i. e. in ref. [58].

According to works of A. Fetter [47] and E. B. Sonin [48], the equations of vortex motion can be obtained from minimization of system's total energy (3.17). Although in mentioned papers a lattice of vortices and mutual interactions between them were also considered, for purpose of this thesis only a case of single vortex is taken into account. This can be justified, if we recall that approximated inter-vortex spacing in neutron star crust is about $d_V \geq 10^{-7}$ m, see sec.

²In further part of this section there will be presented hat this statement is consistent with classical dynamics expressed by forces acting on a vortex line element.

³In fact this is vortex self-energy, because it origins from velocity field induced by the vortex line.

⁴A following general vector identity was used:

$$\mathbf{u} = \nabla \times \mathbf{B} \quad \implies \quad \frac{1}{2} \mathbf{u}^2 = \mathbf{u} \cdot (\nabla \times \mathbf{B}) - \nabla \cdot (\mathbf{u} \cdot \mathbf{B})$$

2.2.3. This value is significantly larger than the coherence length, which is of order of 10^{-15} , and thus vortex-vortex interaction is expected to be marginal. For completeness calculations of mutual interaction energy of two rectilinear vortices are presented in sec. 2.2.4.

Following [47, 48], we can write down equation of motion of vortex in uniform fluid:

$$\frac{\delta E_V}{\delta \dot{s}} = \kappa \rho_s \hat{t} \times \dot{s} \implies \dot{s} = \mathbf{v}_{ind}(s) = \frac{\kappa}{4\pi} \int_{\mathbb{R}^3} \boldsymbol{\omega}(\mathbf{r}') \times \frac{\mathbf{s} - \mathbf{r}'}{|\mathbf{s} - \mathbf{r}'|^3} d^3 r. \quad (3.18)$$

The integral in formula above is divergent, but case of regularization to obtain finite value is discussed in sec. 3.4.

Combining (3.9) and (3.18) one obtains:

$$\dot{s} = \mathbf{v}_{ind} + \mathbf{v}_{ext} \quad (3.19)$$

If an impurity appears in the continuous fluid medium, it will affect the incompressible part of the velocity field resulting in change in formula (3.9):

$$\dot{s} = \mathbf{v}_{ind} + \mathbf{v}_{ext} + \nabla \Phi_{impurity} \quad (3.20)$$

$\Phi_{impurity}$ is a potential of velocity field generated by presence of impurity.

Combining formulas (3.18) and (3.20) with requirement that equation of motion minimizes the vortex energy $\delta E_V / \delta s = 0$ we obtain:

$$\kappa \rho_s \hat{t} \times (\dot{s} - \mathbf{v}_{ind} - \mathbf{v}_{ext} - \nabla \Phi_{impurity}) = 0 \quad (3.21)$$

The first term in above formula is known as Magnus force:

$$\mathbf{f}^M = \kappa \rho_s \hat{t} \times \dot{s} = \kappa \rho_s \hat{t} \times \mathbf{v}_{ind}. \quad (3.22)$$

This force appears in classical equations if we consider spinning object immersed in medium, like air or water.

Physically, equation (3.21) represents equilibration of forces acting on a vortex line element. The balance can be understood if we recall basic assumption of our model: the vortex line is massless. Then, Newtonian equation of motion of vortex line element is given by

$$\mathbf{f}^{tot} = m_{vortex} \ddot{s} \approx 0, \quad (3.23)$$

where \mathbf{f}^{tot} is the total force.

When trying to obtain estimated formula for the velocity field disturbance $\nabla \Phi_{impurity}$ due to motion of impurities, we encounter several problems connected with identification of superfluid part of flow in BCS-like models. Some issues are described in sec. 4.1.1. But, we can move corresponding term to right-hand side of the eq.(3.21) and introduce an unknown force instead:

$$\kappa \rho_s \hat{t} \times (\dot{s} - \mathbf{v}_{ind} - \mathbf{v}_{ext}) = -\mathbf{f}^{VN} \quad (3.24)$$

The vortex-nucleus force was extracted from TDSLDA simulation in work of G. Włazłowski et al. [20] (for description of method of extraction see sec. 4.1.2).

Historically, the Vortex Filament Model was derived in context of classical hydrodynamics, but since a seminal paper of K. W. Schwarz [25] became a main tool for numerical investigation of

quantum turbulence. As it was mentioned in the introduction, initially it was applied to liquid helium in temperatures barely below the superfluid transition temperature. Then a significant fraction of non-superfluid component is present in the system and interaction of this 'normal' fluid with vortex line should occur⁵. Similar phenomenon is expected to occur in fermionic systems, even in zero temperature limit. It was shown that particle density n does not vanish in the core of vortex in fermionic superfluid, whereas the order parameter Δ is equal to zero , i. e. see papers of A. Bulgac and Y. Yu [52, 59]. It can also be seen in the fig. fig. 3.1 and 4.2. Clearly, the vortex core drags the normal component.

The effects related to coupling with normal fluid, in terms of eq. (3.24), can be modelled by inclusion of an additional force representing dissipation:

$$\kappa \rho_s \hat{\mathbf{t}} \times (\dot{\mathbf{s}} - \mathbf{v}_{ind} - \mathbf{v}_{ext}) + \mathbf{f}^{VN} + \mathbf{f}^D = 0 \quad (3.25)$$

Vortex Filament Model in this form was originally proposed by K. W. Schwarz [25].

There is still an intense discussion on a formula for dissipative force. The dissipation is caused by vortex-phonon⁶ interactions that should preserve Galilean invariance, as it was pointed by recent Nobel prize laureate D. Thouless in ref. [60]. Due to this argument, the author of thesis considers that main component of the force should be directed along the vector $\dot{\mathbf{s}}$. In numerical simulations the simplest form is considered (allowed by physical constraints mentioned above):

$$\mathbf{f}^D = -\eta (\dot{\mathbf{s}} - \mathbf{v}_{ext}). \quad (3.26)$$

where η is dissipation coefficient.

Dissipation force in form (3.26) origins from non-direct assumption that normal fluid is moving locally with the same velocity as superfluid component (phonons interacting with vortex form the normal component). For further discussion of this assumption see sec. 5.4.3. However, another form of \mathbf{f}^D was used in simulations of B. Link [21]:

$$\mathbf{f}^D = -\eta \dot{\mathbf{s}}. \quad (3.27)$$

which connects dissipation with absolute velocity of vortex line element. Some arguments against usage of force in form (3.27) are also presented in sec. 5.4.3.

3.3.2 Solving Vortex Filament Model without additional approximations

Notation of Frénet vectors: $\hat{\mathbf{t}}, \hat{\mathbf{n}}, \hat{\mathbf{b}}$ denote tangent, normal and binormal vectors respectively.

Choosing parametrization of vortex line by value on z-axis of the frame of reference we get

$$\mathbf{s}(z, t) = [s_x(z, t), s_y(z, t), z]^T \implies \frac{\partial s_z}{\partial z}(z, t) = 1$$

⁵Terms of superfluid and normal fluid arise naturally in Landau's two fluids theory, which phenomenologically explains lack of viscosity in flow of ${}^4\text{He}$ (boson), but cannot be simply utilized in case of fermions, because in BCS-like theories one cannot disentangle superfluid component from normal component.

⁶Here phonons are considered generally as thermal excitations.

and the tangent vector takes form:

$$\hat{\mathbf{t}} = \frac{1}{\sqrt{\left(\frac{\partial s_x}{\partial z}\right)^2 + \left(\frac{\partial s_y}{\partial z}\right)^2 + \left(\frac{\partial s_z}{\partial z}\right)^2}} \begin{bmatrix} \frac{\partial s_x}{\partial z}(z, t) \\ \frac{\partial s_y}{\partial z}(z, t) \\ \frac{\partial s_z}{\partial z}(z, t) \end{bmatrix} = \frac{1}{\sqrt{\left(\frac{\partial s_x}{\partial z}\right)^2 + \left(\frac{\partial s_y}{\partial z}\right)^2 + 1}} \begin{bmatrix} \frac{\partial s_x}{\partial z}(z, t) \\ \frac{\partial s_y}{\partial z}(z, t) \\ 1 \end{bmatrix}$$

Direct formulas for normal and binormal vectors are described in appendix A.

In this section, due to convenience reasons, following abbreviations on partial derivatives of a vector function $\mathbf{g} = \mathbf{g}(z, t)$ are exploited

$$\dot{\mathbf{g}} = \left[\frac{\partial g_x}{\partial t}, \frac{\partial g_y}{\partial t}, \frac{\partial g_z}{\partial t} \right]^T \quad \mathbf{g}' = \left[\frac{\partial g_x}{\partial z}, \frac{\partial g_y}{\partial z}, \frac{\partial g_z}{\partial z} \right]^T$$

and lenght arc element is denoted as $dl = \sqrt{(s'_x)^2 + (s'_y)^2 + 1}$, and transcribed eq. (3.25)

$$\kappa\rho_s \hat{\mathbf{t}} \times (\dot{\mathbf{s}} - \mathbf{v}_{ind} - \mathbf{v}_{ext}) - \eta \mathbf{s} + \mathbf{f}^{VN} = 0$$

has the form

$$\underbrace{\begin{pmatrix} -\tilde{\eta}dl & -1 & s'_y(z, t) \\ 1 & -\tilde{\eta}dl & -s'_x(z, t) \\ -s'_y(z, t) & s'_x(z, t) & -\tilde{\eta}dl \end{pmatrix}}_A \begin{pmatrix} \dot{s}_x(z, t) - v_x^{ext} \\ \dot{s}_y(z, t) - v_y^{ext} \\ \dot{s}_z(z, t) - v_z^{ext} \end{pmatrix} = \begin{pmatrix} 0 & -1 & s'_y \\ 1 & 0 & -s'_x \\ -s'_y & s'_x & 0 \end{pmatrix} \begin{pmatrix} v_x^{ind} \\ v_y^{ind} \\ v_z^{ind} \end{pmatrix} - \frac{dl}{\kappa\rho_s} \begin{pmatrix} f_x^{VN} \\ f_y^{VN} \\ f_z^{VN} \end{pmatrix} \quad (3.28)$$

whereas with dissipation force used by B. Link (3.27)

$$\underbrace{\begin{pmatrix} -\tilde{\eta}dl & -1 & s'_y(z, t) \\ 1 & -\tilde{\eta}dl & -s'_x(z, t) \\ -s'_y(z, t) & s'_x(z, t) & -\tilde{\eta}dl \end{pmatrix}}_A \begin{pmatrix} \dot{s}_x(z, t) \\ \dot{s}_y(z, t) \\ \dot{s}_z(z, t) \end{pmatrix} = \begin{pmatrix} 0 & -1 & s'_y \\ 1 & 0 & -s'_x \\ -s'_y & s'_x & 0 \end{pmatrix} \begin{pmatrix} v_x^{ind} + v_x^{ext} \\ v_y^{ind} + v_y^{ext} \\ v_z^{ind} + v_z^{ext} \end{pmatrix} - \frac{dl}{\kappa\rho_s} \begin{pmatrix} f_x^{VN} \\ f_y^{VN} \\ f_z^{VN} \end{pmatrix} \quad (3.29)$$

where reduced dissipation coefficient is given by $\tilde{\eta} = \frac{\eta}{\kappa\rho_{sf}}$.

At fixed time t the eq. (3.28) can be considered as a linear algebraic equation for velocity of vortex line $\dot{\mathbf{s}}$ and the solution of this equation is defined only when $\det \mathbf{A} \neq 0$.

$$\begin{aligned} \det \mathbf{A} &= - \left[(s'_x)^2 + (s'_y)^2 + 1 \right] \tilde{\eta}dl - \tilde{\eta}^3 dl^3 = \tilde{\eta}dl \left[-(s'_x)^2 - (s'_y)^2 - 1 - \tilde{\eta}^2 dl^2 \right] \\ \det \mathbf{A} &= \tilde{\eta} (1 + \tilde{\eta}^2) dl^3 \quad \Rightarrow \quad \det \mathbf{A} \xrightarrow[\tilde{\eta} \rightarrow 0]{} 0 \end{aligned} \quad (3.30)$$

We can conclude: **full model is unsolvable in the limit of vanishing dissipation.**

The interpretation of revealed dependency is not fully understand yet, but concerning its origin from simplified form of dissipation (3.27) one should not concetrat on this problem and rather

re-think vortex-phonon interactions. In fermionic system in temperature far below transition point $T \ll T_c$, dissipative force should not have strong effect on vortex pinning unlike vortex-nucleus force, as an example we refer to conclusions in paper of B. Link [21]. On the other hand, we also noted a change in a structure of equation of motions when substituting force in form (3.27) by (3.26) and numerical simulations reveled essential changes in vortex motion in comparison to results of B. Link, for further discussion inspect sec. 6.2.2.

Author of the thesis decided not to concentrate further on topic of dissipation model, despite of consciousness of its impact on investigated system, and leaves elaboration of better formula for dissipation effects as a further research issue.

3.3.3 General approximation for small deflections from straight vortex line

The Vortex Filament Model in form given by eq. (3.25), (3.28) exhibits numerical instabilities in limit of vanishing dissipation $\tilde{\eta} \rightarrow 0$ and suitable changes have to be introduced. For purpose of this work *almost* straight (rectilinear) vortices are considered. It implies $s'_x \approx s'_y \approx 0$, and total neglection of motion (of vortex elements) along z axis $\dot{s}_z \approx 0$. While it seems to be a robust approximation, microscopic calculations by G. Włazłowski et al. [20] indicate that the approximation can be treated as justified, see chapter. 4 for more details. Setting length of the vortex element $dl = 1^7$ one obtains simplified equation:

$$\begin{pmatrix} \dot{s}_x(z, t) - v_x^{ext} \\ \dot{s}_y(z, t) - v_y^{ext} \end{pmatrix} = \underbrace{\begin{pmatrix} -\tilde{\eta} & -1 \\ 1 & -\tilde{\eta} \end{pmatrix}}_{A'^{-1}}^{-1} \left[\begin{pmatrix} 0 & -1 \\ 1 & 0 \end{pmatrix} \begin{pmatrix} v_x^{int} \\ v_y^{int} \end{pmatrix} - \frac{1}{\kappa\rho_s} \begin{pmatrix} f_x^{VN} \\ f_y^{VN} \end{pmatrix} \right] \quad (3.31)$$

where due to $\det A' = \tilde{\eta}^2 + 1$ **no singular terms occur**. The Vortex Filament Model in this form will be investigated in further part of my thesis.

⁷Formula for length of vortex element

$$dl = \sqrt{1 + (s'_x)^2 + (s'_y)^2} \approx 1 + \frac{1}{2} \left[(s'_x)^2 + (s'_y)^2 \right] + \mathcal{O} \left(\left[(s'_x)^2 + (s'_y)^2 \right]^2 \right)$$

implies that in approximation of small deflections from rectilinear line even a linear correction to $dl = 1$ will result in terms of higher orders than relevant for further modifications of the Vortex Filament approach, that are described in this thesis.

3.4 Approximations to Vortex Filament Model

3.4.1 Motivations for approximating Biot-Savart integral

The Vortex Filament Method requires computation of induced velocity according Biot-Savart integral (for $\mathbf{r} = \mathbf{s}(z, t)$):

$$\mathbf{v}_{ind}(\mathbf{r}, t) = \frac{\kappa}{4\pi} \int_{\mathcal{L}} \frac{(\mathbf{s}(z, t) - \mathbf{r}) \times \hat{\mathbf{t}}(z, t)}{|\mathbf{s}(z, t) - \mathbf{r}|^3} dz.$$

Clearly, there is singularity along the vortex line and the Biot-Savart integral (due to zeros in denominator) is divergent. The problem arises from nonphysical assumption of δ -centered vorticity $\boldsymbol{\omega}$ on the vortex line (eq. (3.14)). It makes formally impossible application of eq. (3.25) for dynamics. Nevertheless, physical vortex has finite vortex core radius, so one should be able to evaluate the self-induced velocity. Indeed, regularization schemes of the integral were proposed over years [61, 62].

Moreover, numerical complexity of evaluation of the integral scales like $\mathcal{O}(N^2)$, where N is number of elements on vortex line. One of aims of this thesis was also to find possibly faster and memory-saving algorithm for large scale simulations, i.e. containing many vortices and many impurities.

In the following subsections the Local Induction Approximation (abbreviation LIA, 3.4.2) and model of displacements from straight line are discussed. In both simplifications of the original model the complexity is scaling as complexity of numerical algorithms computing second derivative. Aiming on a system with periodic boundary conditions along the vortex line, the usage of Fast Fourier Transform for derivative computation is a primary choice. The complexity of FFT algorithm is of order $\mathcal{O}(N \log N)$, which can be a great advantage for large systems (in comparison to $\mathcal{O}(N^2)$ for full integral).

Elaboration of possibly the fastest algorithm can result in development of neutron star crust simulations in mesoscopic scales, that are required to further research on dynamics of neutron stars.

3.4.2 Local Induction Approximation and its applicability

In this section, a regularization of Biot-Savart integral will be discussed. For this purpose a description of curve by natural parameter is most convenient.

Starting from integral in form (3.14) and considering a point $\mathbf{s}(\zeta_0, t)$ on a vortex line one obtains

$$\mathbf{v}_{ind}(\mathbf{s}(\zeta_0, t), t) = \frac{\kappa}{4\pi} \int_{\mathcal{L}} \frac{\mathbf{s}'(\zeta, t) \times (\mathbf{s}(\zeta_0, t) - \mathbf{s}(\zeta, t))}{|\mathbf{s}(\zeta, t) - \mathbf{s}(\zeta_0, t)|^3} d\zeta. \quad (3.32)$$

To get rid of the divergence at $\zeta \rightarrow \pm\zeta_0$ (mentioned above), an expansion around the singular point can be provided together with suitable truncation of the integral:

$$\mathbf{s}(\zeta) = \mathbf{s}(\zeta_0) + (\zeta - \zeta_0) \mathbf{s}'(\zeta_0) + \frac{1}{2} (\zeta - \zeta_0)^2 \mathbf{s}''(\zeta_0) + \mathcal{O}[(\zeta - \zeta_0)^3] \quad (3.33)$$

$$\begin{aligned} \mathbf{s}'(\zeta, t) \times (\mathbf{s}(\zeta_0, t) - \mathbf{s}(\zeta, t)) &= \\ &= -[\mathbf{s}'(\zeta_0) + \mathbf{s}''(\zeta_0)(\zeta - \zeta_0) + \dots] \times \left[\mathbf{s}'(\zeta_0)(\zeta - \zeta_0) + \frac{1}{2} \mathbf{s}''(\zeta_0)(\zeta - \zeta_0)^2 + \dots \right] \end{aligned} \quad (3.34)$$

Using a general vector identity $\mathbf{a} \times \mathbf{a} = 0$ and neglecting terms of order $\mathcal{O}[(\zeta - \zeta_0)^3]$ and higher one finally gets

$$\mathbf{s}'(\zeta, t) \times (\mathbf{s}(\zeta_0, t) - \mathbf{s}(\zeta, t)) \approx \frac{1}{2} \mathbf{s}'(\zeta_0) \times \mathbf{s}''(\zeta_0)(\zeta - \zeta_0)^2 \quad (3.35)$$

indicating that main component of the vortex self-induced velocity at point $\mathbf{s}(\zeta_0)$ on a vortex line is directed along binormal vector $\hat{\mathbf{b}}$ at this point (see appendix A.2 for explanation).

Treating in similar way the denominator of expression in integral (3.32) we get:

$$\mathbf{v}_{ind}^{LIA} = \frac{\kappa}{4\pi} \int_{a_0}^{\mathcal{R}} \frac{d(\zeta - \zeta_0)}{|\zeta - \zeta_0|} \mathbf{s}'(\zeta_0) \times \mathbf{s}''(\zeta_0) = \frac{\kappa}{4\pi} \ln\left(\frac{\mathcal{R}}{a_0}\right) \hat{\mathbf{b}}. \quad (3.36)$$

Parameter a_0 is an effective vortex core radius and \mathcal{R} is an arbitrary upper cutoff, which in general has to depend on position and for infinite superfluid medium sometimes is said to be connected with local (or global) curvature of the vortex line [62, 61].

Paper of K. W. Schwarz [25] suggests that Local Induction Approximation is precise in case of circular vortex ring dynamics, but for purpose of the thesis a reliable model for almost rectilinear vortex is demanded. Numerical investigation of Local Induction Approximation revealed problems connected with numerical evaluation of Frénet normal and binormal vectors at inflection points of curve, where derivatives $\frac{\partial^2 s_x}{\partial z^2}, \frac{\partial^2 s_y}{\partial z^2} \rightarrow 0$, see fig. 3.2. Intuitively, for a straight vortex there is no a distinguished direction in space to fix orientation of normal and binormal vector because of vanishing curvature of the line (one can perform rotation of Frénet trihedron to obtain equivalent frame of reference). Moreover, at every point infinitesimally close to inflection point vectors $\hat{\mathbf{n}}, \hat{\mathbf{b}}$ are well defined and normalized, but they change direction when passing through the inflection point.

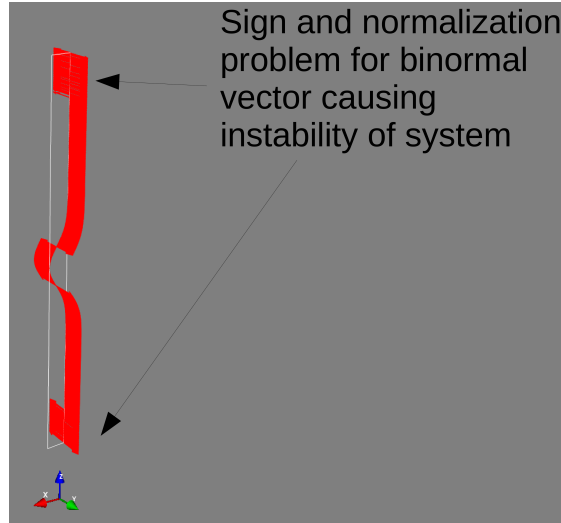


Figure 3.2: Vectors of self-induced velocity in Local Induction Approximation for a vortex slightly bent from a straight line configuration, the numerical instability of calculation the binormal vector is revealed.

Logarithmic factor in equation (3.36) should decrease to 0 in order to cancel the effect of vector direction change. However, in most cases the factor is considered to be constant [62, 21]. Substitution of \mathcal{R} to local radius of curvature in the LIA expression, as suggested by C. F. Barenghi,

R. J. Donnelly and W. F. Vinen in [61], makes the self-induced velocity infinite at inflection points.

The regularization of velocity is required for purpose of numerical simulations, because rapid changes of direction of the vectors affect stability of ODEs solvers, thus **the author of the thesis concluded that LIA is not applicable for purpose of simulations with almost rectilinear vortices.**

3.4.3 Model of vibrations of columnar vortex

Returning to eq. (3.31), in case of deflections from straight line one can utilize another approximation that dates back a nineteenth-century work of Lord Kelvin [63], see also [47, 48, 64].

To introduce the approximation, a connection between vortex self-induced velocity and tension force have to be remarked. In terms of eq. (3.25) we have:

$$\begin{aligned}\kappa\rho_s\hat{\mathbf{t}} \times (\dot{\mathbf{s}} - \mathbf{v}_{ext} - \mathbf{v}_{ind}) + \mathbf{f}^{VN} + \mathbf{f}^D &= 0, \\ \kappa\rho_s\hat{\mathbf{t}} \times (\dot{\mathbf{s}} - \mathbf{v}_{ext}) + \mathbf{f}^T + \mathbf{f}^{VN} + \mathbf{f}^D &= 0.\end{aligned}$$

Thus a columnar vortex should behave somehow similarly to vibrating string.

In case of small deflections, and neglecting motion of the vortex elements along z direction, it is convenient to introduce notation:

$$\mathbf{u}(z, t) = [s_x(z, t), s_y(z, t), 0]^T, \quad (3.37)$$

instead of $\mathbf{s}(z, t) = [s_x(z, t), s_y(z, t), z]^T$.

The self-energy of vortex, given by eq. (3.17), is expressed by \mathbf{u} in form:

$$E_V = \frac{\rho\kappa^2}{8\pi} \int_{\mathcal{L}} dz \int_{\mathcal{L}} dz' \frac{\hat{\mathbf{t}}(z, t) \cdot \hat{\mathbf{t}}(z', t)}{|\mathbf{s}(z, t) - \mathbf{s}(z', t)|} = \frac{\rho\kappa^2}{8\pi} \int_{\mathcal{L}} dz \int_{\mathcal{L}} dz' \frac{\hat{\mathbf{t}}(z, t) \cdot \hat{\mathbf{t}}(z', t)}{|\mathbf{u}(z', t) - \mathbf{u}(z, t) + (z - z')\hat{\mathbf{z}}|}, \quad (3.38)$$

where the tangent vector is now given by $\hat{\mathbf{t}} = \frac{1}{\sqrt{1+(\frac{\partial s_x}{\partial z})^2+(\frac{\partial s_y}{\partial z})^2}} \frac{\partial \mathbf{s}}{\partial z} = \frac{1}{\sqrt{1+\frac{\partial u_x}{\partial z} \cdot \frac{\partial u}{\partial z}}} [\hat{\mathbf{z}} + \frac{\partial \mathbf{u}}{\partial z}]$.

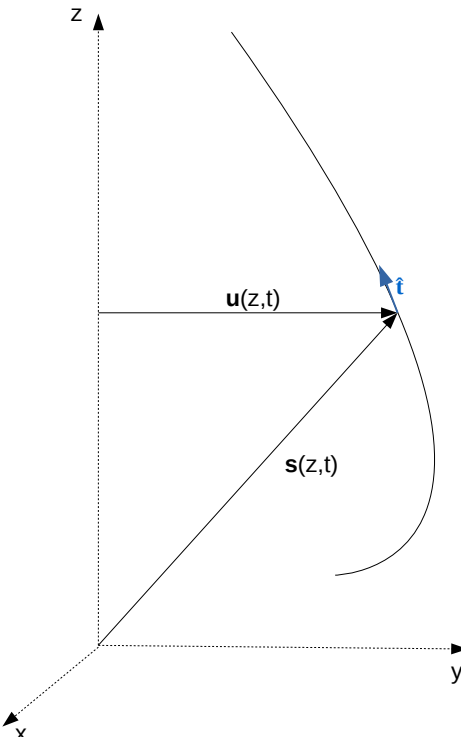


Figure 3.3: Scheme of vectors used for description of a vortex line in parametrization of curve by value of z coordinate

Making simple algebra:

$$E_V = \frac{\rho\kappa^2}{8\pi} \int_{\mathcal{L}} dz \int_{\mathcal{L}} dz' \frac{1 + \frac{\partial \mathbf{u}}{\partial z} \cdot \frac{\partial \mathbf{u}}{\partial z'}}{\sqrt{(\mathbf{u}(z', t) - \mathbf{u}(z, t))^2 + (z - z')^2}} = \quad (3.39)$$

$$= \mathcal{E}_0 + \frac{\rho\kappa^2}{8\pi} \int_{\mathcal{L}} dz \int_{\mathcal{L}} dz' \frac{\frac{\partial \mathbf{u}}{\partial z} \cdot \frac{\partial \mathbf{u}}{\partial z'}}{\sqrt{(\mathbf{u}(z', t) - \mathbf{u}(z, t))^2 + (z - z')^2}} \quad (3.40)$$

and using expansion $1/\sqrt{a+x} \approx \frac{1}{\sqrt{a}} - \frac{1}{2} \frac{x}{a^{3/2}} + \frac{3}{8} \frac{x^2}{a^{5/2}} + \mathcal{O}(x^3)$ and denoting $\Delta \mathbf{u} = \mathbf{u}(z, t) - \mathbf{u}(z', t)$ we end up with formula:

$$E_V = \mathcal{E}_0 + \frac{\rho\kappa^2}{8\pi} \int_{\mathcal{L}} dz \int_{\mathcal{L}} \left(\frac{\partial \mathbf{u}}{\partial z} \right)^2 \left[\frac{1}{|z - z'|^2} + \frac{1}{2} \frac{\Delta \mathbf{u}^2}{|z - z'|^3} + \mathcal{O}(\Delta \mathbf{u}^4) \right]. \quad (3.41)$$

Switching to Fourier space we have:

$$E_V \approx \mathcal{E}_0 + \int_{\mathcal{L}} dz' \int_{-\infty}^{\infty} dk_z \hat{\mathbf{u}}(k_z) \hat{\mathbf{u}}(-k_z) \underbrace{\frac{\rho\kappa^2}{4\pi} \int_{a_0}^{\infty} dz \left[k_z^2 e^{ik_z z} - \frac{1}{z^2} (1 - e^{ik_z z}) \right]}_{\omega(k_z)} \quad (3.42)$$

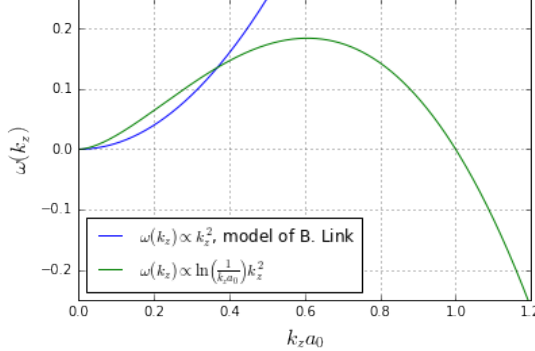


Figure 3.4: Comparison of two different approximations on Kelvin waves dispersion relation. Analysis of plot suggests that formula (3.44) can be used only for waves shorter than $2a_0$, because decreasing part of relation is an artifact of truncation of series expansion. Dispersion relation exploited by B. Link differs significantly, but there are no interpretation problems and no restriction on wavelengths appearing in simulations.

Again, to derive equation of motion, we minimize the energy (3.42) by taking variational derivative:

$$\frac{\delta E_V}{\delta \hat{\mathbf{u}}^*} = \omega(k_z) \hat{\mathbf{u}}(k_z) \quad (3.43)$$

Details of derivation can be found in paper [48]. The truncation of series (3.41) at $\mathcal{O}(\Delta \mathbf{u}^4)$ gives dispersion relation

$$\omega(k_z) = \frac{\rho\kappa^2}{4\pi} \ln\left(\frac{1}{k_z a_0}\right) k_z^2 \quad (3.44)$$

a_0 — effective vortex core radius

which can be valid only for $k_z \ll 1/a_0$, because the expression becomes negative at $k_z = 1/a_0$ and this behaviour is considered non-physical. According to fig. 3.4, the formula (3.44) cannot be utilized, because the computational grid should not be restricted to placement of vortex elements in steps Δz greater than $2a_0$ and shorter waves than $2a_0$ have to be available for simulation.

Equation of motion expressed in reciprocal space (dependence on wave number k_z not z), is obtained by comparing (3.18) and (3.43). It is following:

$$\kappa \rho_s \hat{\mathbf{t}}(k_z) \times \frac{\partial \hat{\mathbf{u}}}{\partial t}(k_z, t) = \omega(k_z) \hat{\mathbf{u}}(k_z, t) \quad (3.45)$$

The equation above has fundamental solutions representing helical waves propagating with wave number k_z along the vortex line (no dissipation included). These waves are called Kelvin

waves. It is worth to mention, that providing $\omega(k_z)$, extracted from microscopic simulation, should reproduce realistic dynamics of vortex line. My attempts to extract the dispersion relation from results of G. Włazłowski et al. [20] are discussed in sec. 4.2.

Transforming back to positions in normal space we can obtain expression for tension force per length of the vortex line:

$$\mathbf{f}^T \approx T_V(z) \frac{\partial^2 \mathbf{u}}{\partial z^2} \quad (3.46)$$

It was proposed in several papers, including work of B. Link [21], to treat vortex tension T_V as a constant. Dispersion relation obtained with the assumption above was compared with (3.44) in fig. 3.4. The tension constant was estimated in simulations of vortex-nucleus system in TDSLDA model (for details see paper of G. Włazłowski et al. [20]) to be 1.4 MeV and 7.3 MeV for neutron background densities 0.014 and 0.031 fm⁻³ respectively.

3.4.4 Final equations used for numerical simulations of Vortex Filament Model

Combining equations (3.24),(3.45) and assuming dissipation force in form (3.26) one obtains following equation of motion in reciprocal space:

$$\begin{pmatrix} \frac{\partial \hat{u}_x}{\partial t}(k_z, t) - 2\pi v_x^{ext} \delta(k_z) \\ \frac{\partial \hat{u}_y}{\partial t}(k_z, t) - 2\pi v_y^{ext} \delta(k_z) \end{pmatrix} = \underbrace{\begin{pmatrix} -\tilde{\eta} & -1 \\ 1 & -\tilde{\eta} \end{pmatrix}}_{A'^{-1}}^{-1} \begin{pmatrix} \omega(k_z) \hat{u}_x(k_z, t) - \frac{1}{\kappa\rho_s} \hat{f}_x^{VN} \\ \omega(k_z) \hat{u}_y(k_z, t) - \frac{1}{\kappa\rho_s} \hat{f}_y^{VN} \end{pmatrix} \quad (3.47)$$

Formally it is still an nonlinear partial differential equation, because vortex-nucleus force is dependent on positions of vortex elements and on first derivatives of these variables (an angle between tangent vector and vector connecting vortex line element with center of mass of impurity, exact formula given in eq. (4.3)).

The equation in form above was utilized in numerical simulations discussed in chap. 5 and 6. For justification of usage of reciprocal space see sec. 5.1.2.

Chapter 4

Vortex-impurity interaction in neutron star crust. Review of previous works and TDSLDA simulations analysis.

4.1 Vortex-nucleus force in neutron star crust

4.1.1 Hydrodynamical approach

As it was mentioned before in section 2.1.3, in neutron star crust one can consider nuclei embedded in the uniform neutron superfluid. A nuclear impurity can be considered as having an effective superfluid density inside denoted by ρ_N . In addition, the impurity may have an instantaneous arbitrary velocity v_N . The presence of the impurity modifies the velocity field of superfluid, compare with eq. (3.20). The modification can be described as gradient of scalar potential $\Phi^{impurity}$, which has different forms inside and outside of the nuclei (neutrons in background superfluid can penetrate interior of the impurity). Velocity fields and potentials $\Phi_{in}^{impurity}$ and $\Phi_{out}^{impurity}$ are required to be continuous, thus suitable conditions at boundary of the impurity have to be satisfied. For details see a discussion of the topic by P. Magierski in supplementary material for article [20].

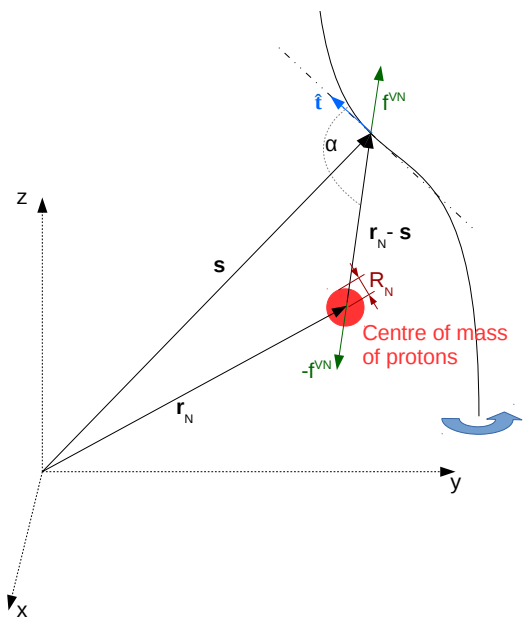


Figure 4.1: Schematic of vortex nucleus system with perspicuous explanation of symbols used in equations.

In this supplement following hydrodynamical formula for the energy of vortex-impurity system inside a tube of radius D was derived:

$$E_{tot} = \frac{\rho_s \kappa^2}{4\pi} H \ln \left(\frac{D}{2a_0} \right) + 2\pi R_N^3 \frac{\rho_N - \rho_s}{\rho_N + 2\rho_s} \left[\frac{1}{3} (\rho_N - \rho_s) v_N^2 + \rho_s \left(\frac{\kappa}{2\pi |\mathbf{r}_N - \mathbf{s}|} \right)^2 \right] \quad (4.1)$$

where:

a_0 - effective core radius, in this case is considered to be of order of BCS coherence length (3.3),

ρ_s - superfluid density outside the nuclear impurity — assumed to be equal to neutron fraction mass density (due to small number of thermal excitations discussed in sec. 1.1),

ρ_N - superfluid density inside the nuclear impurity, discussed furthered.

Inside a nucleus, in region where density of protons is getting almost equal to density of neutrons superfluid order parameter almost vanishing. This can be deduced from Fig. 4.2 showing that the paring field goes to zero for densities around 0.1 fm^{-3} ($k_F \approx 1.5 \text{ fm}^{-1}$). This phenomena can be seen in the visualization of TDSLDA initial state in the fig. 4.2. As mentioned in sec. 3.3.1, the superfluid density cannot be disentangled from normal density within BCS-like theories, and thus no reliable estimate on ρ_N can be obtained. Therefore even the sign of $(\rho_N - \rho_s)$ cannot be determine and in consequence character of the vortex-impurity $\mathbf{F} \sim -\nabla E_{tot}$ (attractive or repulsive) cannot be established.

4.1.2 Effective force approach and method of obtaining this force from microscopic quantum model (TDSLDA)

Due to many relevant problems of hydrodynamical estimates of velocity field generated by presence of nucleus, we can exploit numerical simulations of vortex-nucleus system based on microscopical. From them we can extract the effective force acting between centre of mass of protons and quantum vortex¹. This approach was proposed in recent work of G. Włazłowski, K. Sekizawa, P. Magierski, A. Bulgac, M. McNeil Forbes [20].

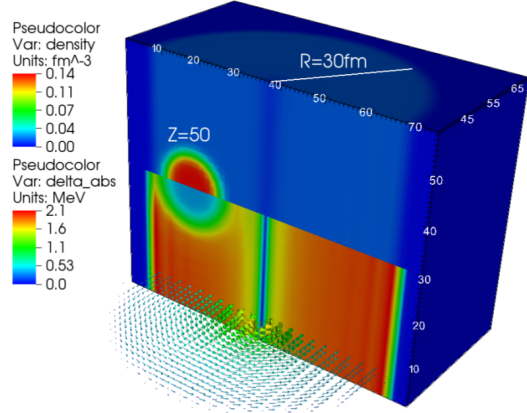


Figure 4.2: Visualization of vortex-nucleus system studied in TDSLDA model. Disappearance of Δ in the vortex core and inside nucleus can be seen (lower half of the intersection). Illustration taken from [20].

In the simulations, two cases were considered, where system contained 2,530 or 5,710 neutrons and 50 protons. Produced neutron background densities were of 0.014 fm^{-3} and 0.031 fm^{-3} ,

¹We can consider centre of mass of protons as a centre of nuclei. Due to fluctuations of neutrons density connected with flow of fluid around the nuclei any other estimate is problematic to be calculated in the numerical simulation.

respectively. These two cases correspond to baryon densities of Wigner-Seitz cells equal to $2.78 \cdot 10^{13} \text{ g} \cdot \text{cm}^{-3}$ and $5.95 \cdot 10^{13} \text{ g} \cdot \text{cm}^{-3}$.

Computations were performed on 3D grid of points of size $75 \times 75 \times 60$ fm with spacing $\Delta x = 1.5$ fm. Code used for the simulation imposes periodic boundary conditions, so an external potential restricting motion of particles in x,y directions was added and hereby a tube with periodic boundary conditions in direction of z-axis was created, see fig. 4.2.

Schematic of method of extraction of the force is presented on fig. 4.3. In the study case an external force, that couples only to protons was provided to keep it in constant motion along straight line (the force was adjusted at every timestep to fulfill requirement of constant velocity motion). According Newtonian mechanics, if the nucleus moves with constant velocity then the total force acting on it must be zero. It means that the external force has to be balanced by other force, which was attributed to vortex-nucleus interaction.

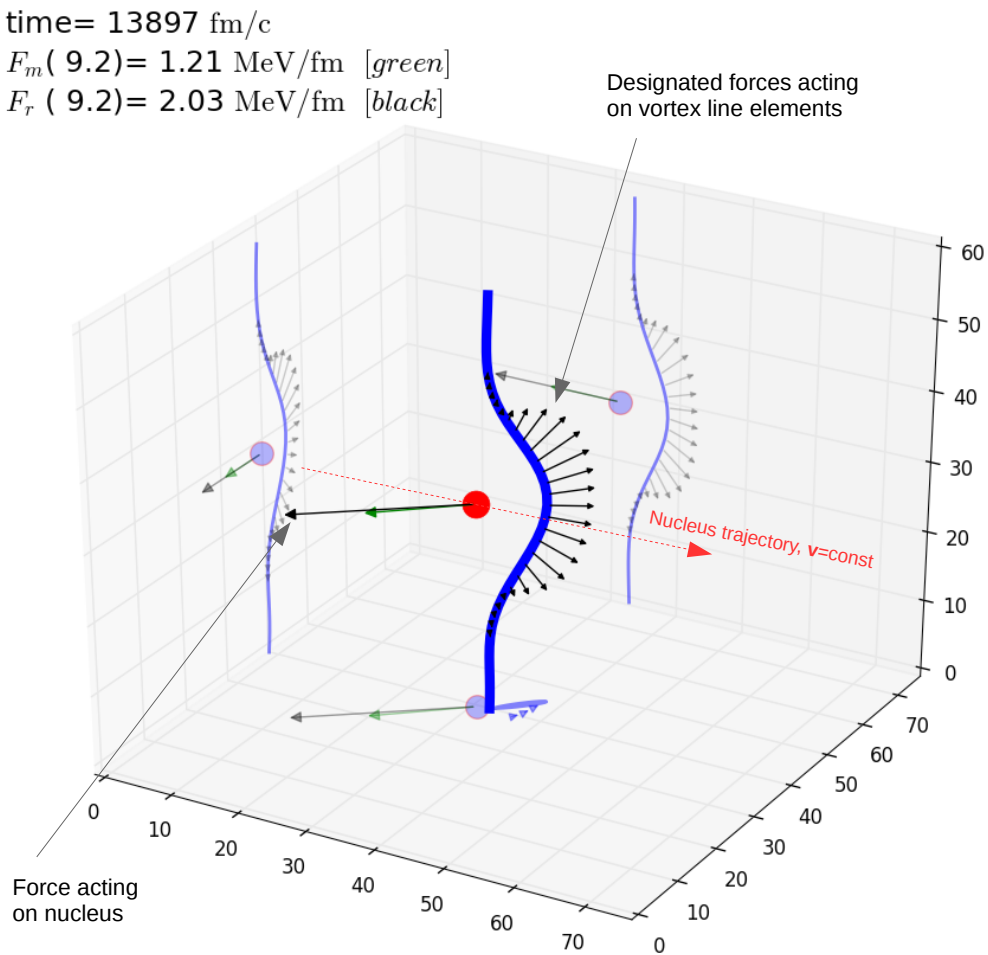


Figure 4.3: Schematic of method used for extraction of vortex-nucleus force from TDSLDA model. Illustration created with usage of data provided by authors of article [20].

This approach enabled to omit problems connected with estimations of the force with utilization of the hydrodynamics (see sec. 4.1.1). However the data on interaction magnitude were

obtained only for vortex-nucleus distance greater than about 8 fm and no reliable estimate for closer distances can be obtained. In case of numerical simulations presented in chap. 5 and 6 there were necessity to supervise if the vortex line does not achieve untrusted values of vortex-nucleus spacing during the time evolution.

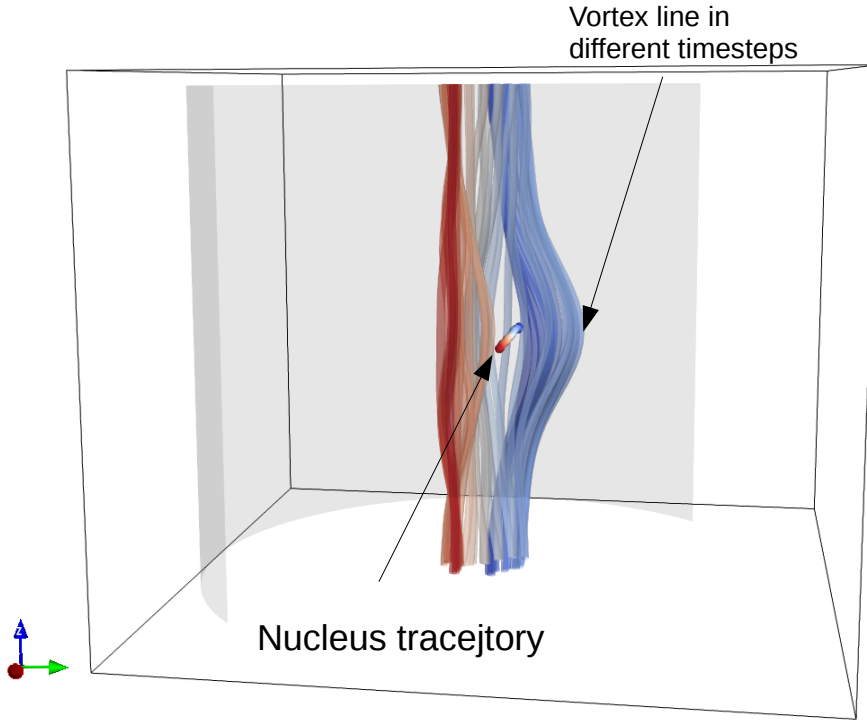


Figure 4.4: Evolution of vortex line due to constantly moved nuclei. Glyphs colors diverge from blue to red according to increasing time. Vortex line created two dimensional manifold that can be parameterized by z, t and magnitude and rotation angle of displacement vector u (see fig. 3.3) for fixed z can be mapped onto complex plane. Thus in context of the data analysis can be treated as two dimensional complex signal, which was utilized in sec. 4.2.

The simulations presented in paper [20] resulted in two main conclusions:

- the configuration with vortex imprinted inside nucleus is unstable and thus the vortex is almost immediately expelled from interior of the nucleus resulting in quick unpinning (time scales of order of 1000 fm/c),
- vortex-nucleus interaction has repelling character, and it acts mostly in radial direction² with negligible tangent components.

Moreover force acting per unit length of the vortex as a function of vortex-nucleus distance

²Along vectors connecting center of mass of nucleus and vortex line elements, see schematic in fig. 4.1.

was extracted by fitting formula³

$$f(r) = \frac{\sum_{k=0}^{n=2} a_k r^k}{1 + \sum_{k=1}^{n=5} b_k r^k}. \quad (4.2)$$

The obtained coefficients of the above Padé approximant can be find in tab. 5.1. Magnitude of force (4.2) is compared to results of R. I. Epstein, G. Baym [65, 64] and B. Link [21] in fig. 4.7.

Author of this thesis does not consider changes of magnitude of vortex-nucleus force with changing number of protons Z inside nucleus, however it can have non-negligible impact. According to formula (4.1) the strength of the interaction should be a nonlinear function of superfluid mass density inside and outside of nuclei, but it was already pointed that there are no reliable methods for extraction of the superfluid component in the BCS-like theories.

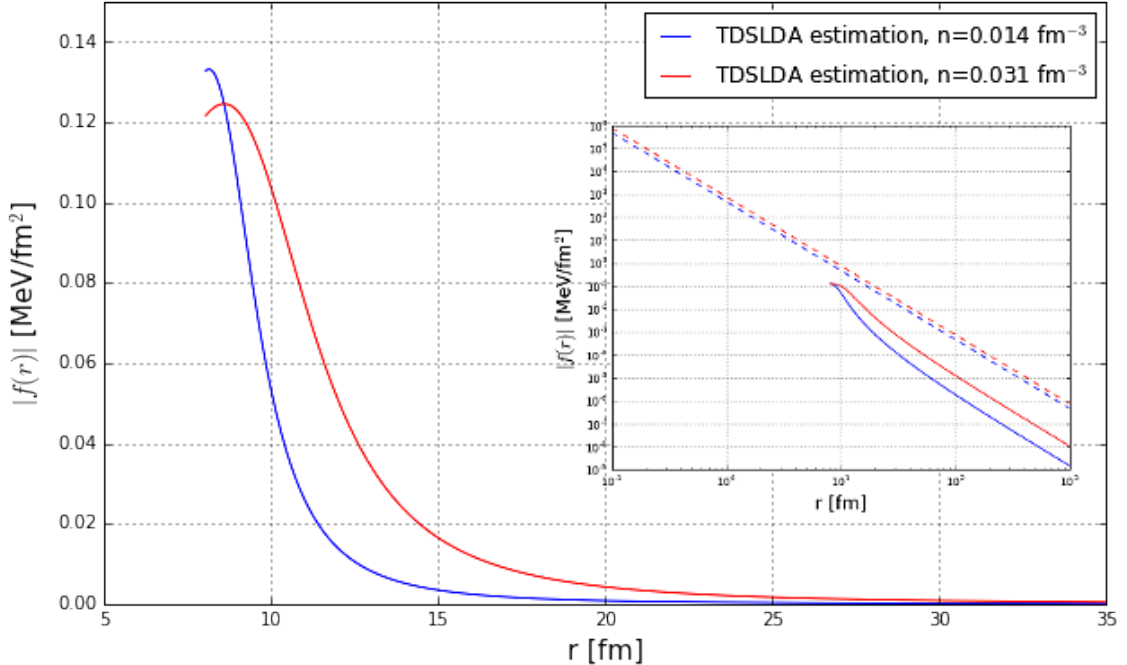


Figure 4.5: Magnitude of the force per unit length of the vortex line, estimated from simulations in TDSLDA model [20] for two different neutron background densities. In inset, log-log plot reveals scaling $f(r) \propto r^{-3}$, required by formula (4.1). The lines are truncated for values of vortex-nucleus distance not obtained in TDSLDA simulations. Dotted lines present an estimate of the force in the hydrodynamic approach for superfluid density inside impurity ρ_N equal to density of neutrons, large discrepancy in orders of magnitudes seen, see also discussion in sec. 4.1.1.

³The expression in this form preserves long range behaviour given by formulas (4.1) and (4.5).

4.1.3 Comparison of estimates on vortex-nucleus force magnitude

Due to radial character of vortex-nucleus force it can be described by following formula [20]:

$$\mathbf{f}^{VN} = f(|\mathbf{s} - \mathbf{r}_N|) \sin(\alpha) \frac{\mathbf{s} - \mathbf{r}_N}{|\mathbf{s} - \mathbf{r}_N|} \quad (4.3)$$

where $f(r)$ is the magnitude of interaction force with respect to vortex-nucleus distance and the angle $\alpha = \angle(\hat{\mathbf{t}}, \mathbf{s} - \mathbf{r}_N)$, \mathbf{s} is a vector pointing element of vortex line and \mathbf{r}_N is a vector pointing centre of mass of impurity. Compare with schematic in fig. 4.1.

Force acting on impurity is connected with tot energy of superfluid flow with formula

$$\mathbf{f}^{VN} = -\nabla_{\mathbf{r}_N} E_{tot} \quad (4.4)$$

First research on the interaction force was performed by R. I. Epstein and G. Baym [65, 64]. Exploiting both, hydrodynamical approach similar to the described in sec. 4.1.1 and Ginzburg-Landau theory, they obtained following formula

$$f(r) = \frac{2r}{R_N} \left[\frac{4E_S}{\left(1 + (r/R_N)^2\right)^5} + \frac{E_L}{\left(1 + (r/R_N)^2\right)^2} \right], \quad (4.5)$$

containing short range and long range part of interaction corresponding to coefficients E_S and E_L , respectively and R_N is effective radius of the impurity (nucleus). Values of these parameters are illustrated in fig. 4.6 (insets a. and b.) and magnitudes with respect to baryon mass density are plotted in fig. 4.6 (inset c.). In addition

It was revealed that interaction between vortex and nucleus can change character from repulsive to attracting for varying density of superfluid medium (compare fig. 4.6, inset c.).

An approximation to the force (4.5) was utilized by B. Link in paper [21], but with more convenient formula (indicating maximal magnitude F_m):

$$f(r) \approx 0.85 \cdot F_m \frac{r}{R_{WS}} e^{-(r/R_{WS})^2} \quad (4.6)$$

where R_{WS} is Wigner-Seitz sell radius describing average spacing between nuclei⁴. B. Link was considering case of maximal amplitude of force in range $0.01T_V \div 0.1 T_V$, and vortex tension parameter T_V was introduced in sec. 3.4.3. Estimate obtained within TDSLDA simulations in work of G. Włazłowski et al. [20] (1.4 MeV for neutron background density 0.014 fm^{-3}) is consistent with 1.35 MeV calculated for same density with assumptions mentioned in B. Link article.

The vortex-nucleus force obtained in microscopic model TDSLDA can be considered as the most trustworthy, however, due to great numerical complexity of simulations of the TDSLDA approach, only two neutron background densities were investigated. Analysis of the figure 4.7 suggests that, in comparison to the TDSLDA result, the formula (4.5) with parameters obtained by R. I. Epstein and G. Baym underestimates interaction range for neutron background density $n_n = 0.031 \text{ fm}^{-3}$ and can provide attractive interaction for $n_n = 0.014 \text{ fm}^{-3}$ (on length scales

⁴In paper of B. Link [21] random lattice with average spacing of $2R_{WS}$ was considered, for explanation of correspondence of avg. spacing and spherical Wigner-Seitz cell radius see sec. 2.1.4

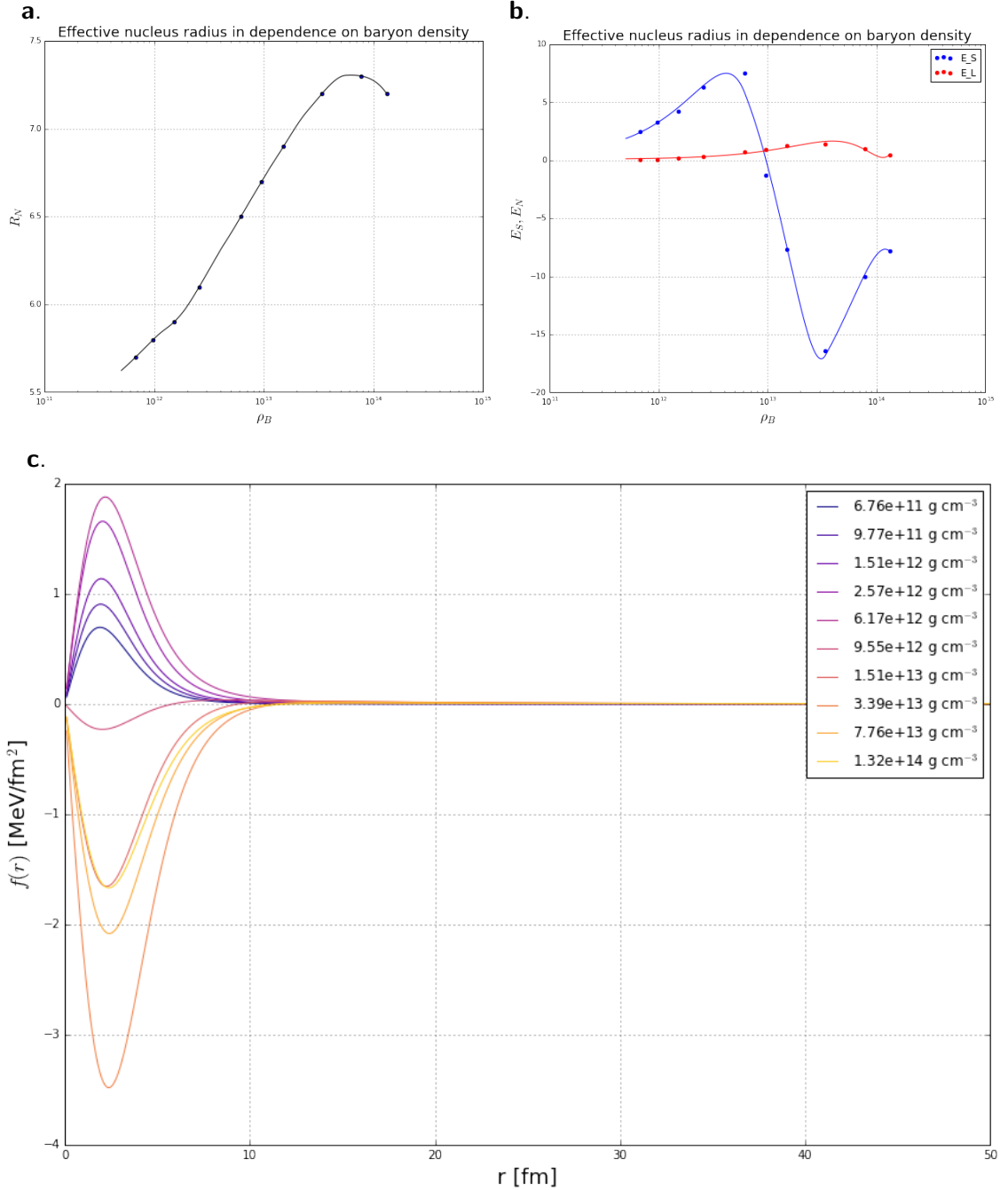


Figure 4.6: Results from works of Epstein & Baym. Inset **a.** — effective nucleus radius; inset **b.** — sign and magnitude of long- and short- range components of vortex nucleus force as a function of baryon mass density; inset **c.** — magnitude and sign of vortex-nucleus force with respect to vortex-nucleus separation, different colors represent varying baryon mass density.

important for vortex-nucleus dynamics), while approximation utilized by B. Link overestimates range as well as strength of the interaction in both cases.

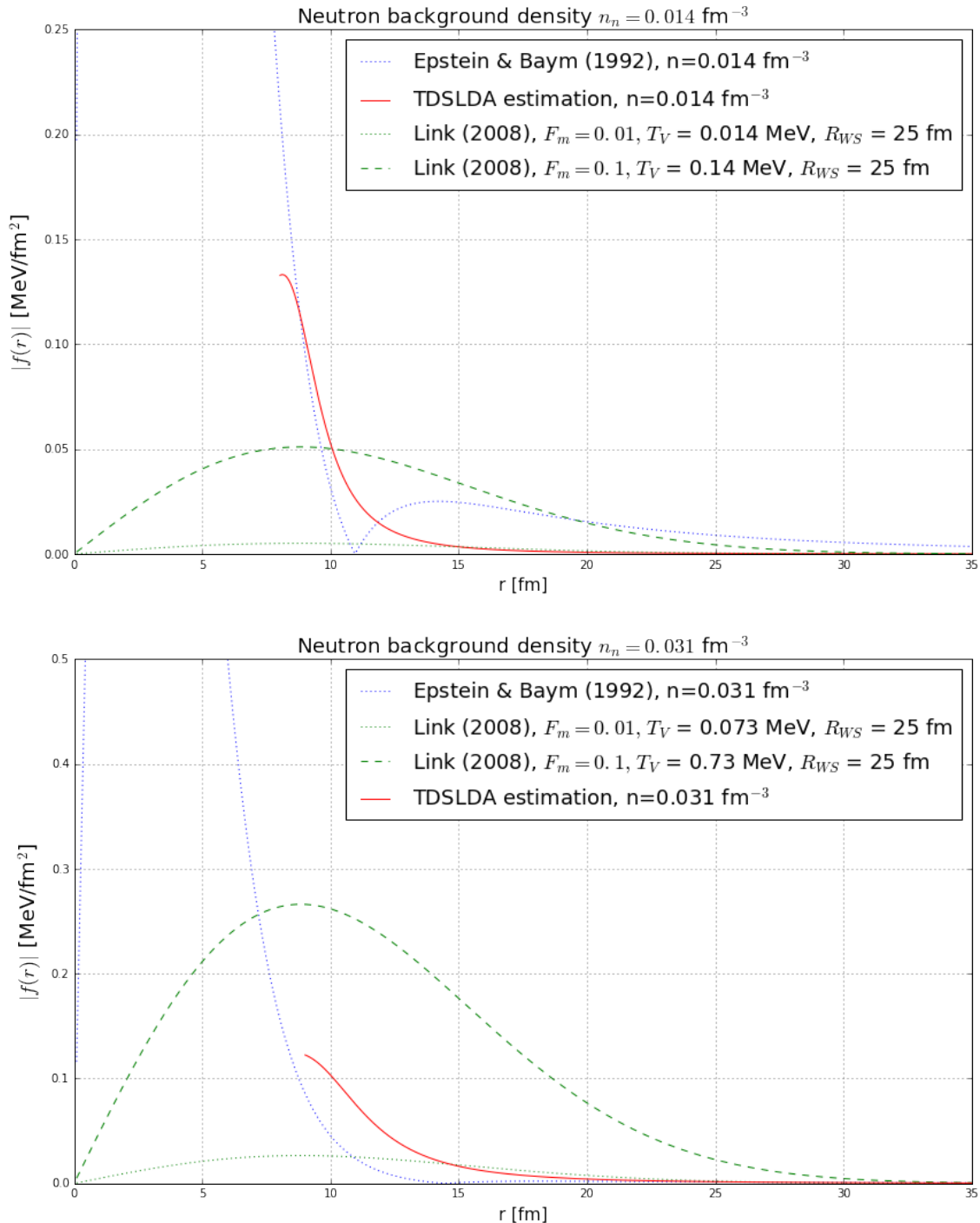


Figure 4.7: Comparison of magnitude of vortex-nucleus forces (absolute value, irrespectively to sign $f(r)$.)

4.2 Kelvin waves dispersion relation

4.2.1 Spectrum of vortex waves in TDSLDA simulations

Interaction of vortex with impurities can generate excitations of a vortex line, which are referred as Kelvin Waves (or Kelvons when studying microscopic quantum model), thus it is worth to include several words about the dispersion relation of such excitations in this chapter.

The easiest method to reveal frequencies present in the system is calculation of a power spectrum (Fourier transform of correlation function).

In purpose to deal with two real variables of position vector \mathbf{u} (for definition see sec. 3.4.3 and fig. 3.3), one can introduce a complex variable

$$U(z, t) = u_x(z, t) + iu_y(z, t). \quad (4.7)$$

which is referred as vortex motion signal in futher part of this section.

A power spectrum of vortex motion signal U can be computed with respect to time, position along z-axis or both. A Fourier transformation $\mathcal{F}_{z \rightarrow k_z}$ corresponds to an integral transform⁵

$$\mathcal{F}_{z \rightarrow k_z}[U(z, t)](k_z, t) = \frac{1}{2\pi} \int_{-\infty}^{\infty} e^{ik_z z} U(z, t) dz \quad (4.8)$$

and

$$\mathcal{F}_{t \rightarrow \omega}[U(z, t)](k_z, t) = \frac{1}{2\pi} \int_{-\infty}^{\infty} e^{-i\omega t} U(z, t) dt \quad (4.9)$$

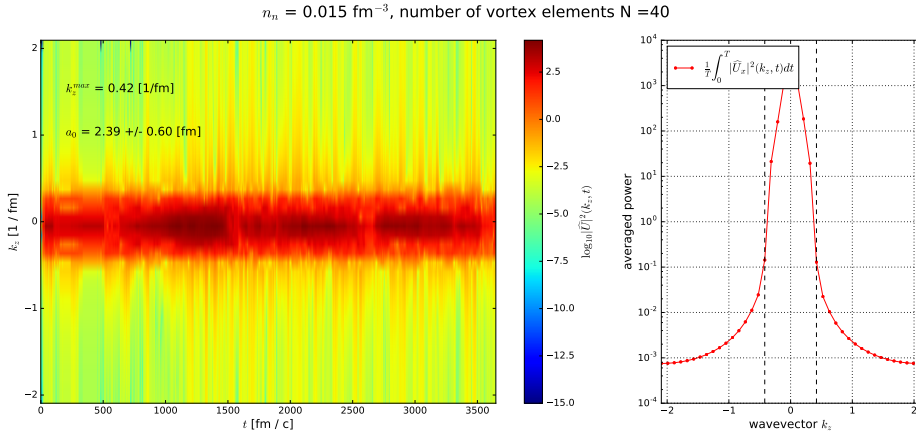
Note that combining these two transforms, we get exponent factor $e^{i(k_z z - \omega t)}$, which clearly demonstrates that we look for waves propagating in time along the vortex line. Power spectrum $S(k_z, t) = |\mathcal{F}_{z \rightarrow k_z}[U]|^2$ will be denoted as *spectrogram*, which is not strictly correct definition in context of signal analysis, but is proposed in the following section as an abbreviation.

The plots in fig. 4.8 reveal cutoff wavenumber k_z^{max} and suppression of high frequency waves (which can be connected with dissipation). It was also noticed, that values of k_z^{max} are fairly lower than maximal wavenubers that can be seen in TDSLDA simulation. It was assumed that cutoff wavenumber k_z^{max} can be connected with effective vortex radius $a_0 \approx \frac{1}{k_z^{max}} \pm \frac{1}{k_z^{max^2}}$. Due to insufficient resolution in both cases the obtained value was $a_0 = 2.3 \pm 0.6$ fm and the result is of the same order as BCS coherence length (see sec. 3.1.1 and tab. 5.2).

Trial to compute full spectrum $|\mathcal{F}_{t \rightarrow \omega}[\mathcal{F}_{z \rightarrow z}[U]]|^2$ does not enable to obtain a dispersion relation $\omega(k_z)$ for Kelvin waves, thus it is omitted. See sec. 4.2.2 for further discussion.

⁵In fact, due to finite number of points representing a function and domain consisted of finite interval $[z_{min}, z_{max}]$, a numerical Fourier Transform is rather an algorithm for evaluation of coefficients of Fourier Series approximating function on this interval.

a.



b.

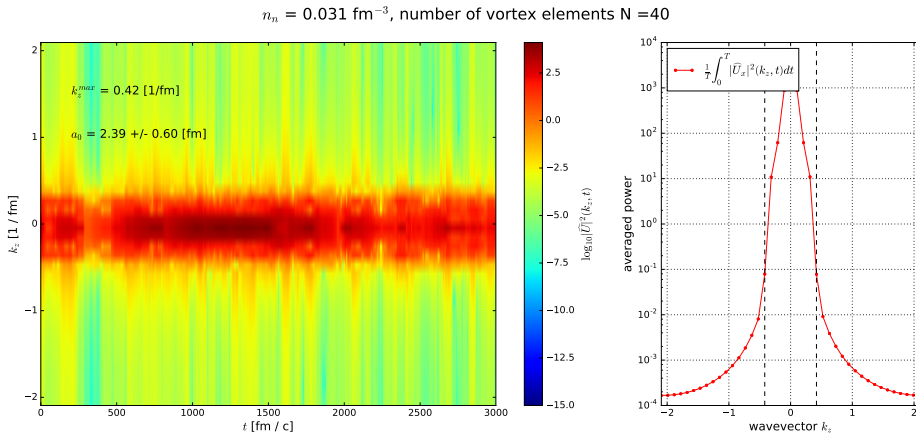


Figure 4.8: Analysis of power spectrum of vortex motion signal U . Spectrograms for neutron background density $n_n = 0.014 \text{ fm}^{-3}$ on inset a. and $n_n = 0.031 \text{ fm}^{-3}$ on inset b. Dotted horizontal lines indicate k_z^{\max} . See definitions of spectrogram and U in text.

4.2.2 Trials of detrending vortex motion signal for analysis

The author of the thesis is conscious of drawbacks of power spectrum analysis and it is suspected that the failure of Kelvin waves dispersion relation designation can be connected with non-stationarity of the vortex motion signal U .

The linear methods of signal analysis are mostly applicable for stationary signals, however vortex motion can be thought as consisting of two components: a trend connected with vortex-nucleus interaction (thus signal is non-stationary) and Kelvin wave oscillations that will appear for higher frequencies. Despite the fact, that both components are non-linearly coupled by vortex-nucleus force a trial of extraction of detrended signal (stationary) was performed. An idea of Empirical Mode Decomposition proposed by N. E. Huang [66] was utilized, but trial ended up with no success.

This trial of vortex position signal detrending was described to reveal some of troubles when estimation of Vortex Filament Model parameters from vortex trajectories obtained in TDSLDA simulations (sec. 4.1.2). Parameters estimation was not the main goal of the thesis, therefore further work on this topic was abandoned.

Chapter 5

Metodology of numerical simulations

5.1 Utilized algorithms

5.1.1 Discretization of vortex line

In order to perform a numerical calculations, the vortex line was represented as array of points, called vortex elements. The distance between two adjacent vortex elements is constant and it is denoted as Δz throughout the thesis. Constant spacing between the vortex elements is required by FFT algorithm that was utilized in my code (see sec. 5.1.3).

Discretization of the vortex line transforms nonlinear partial differential equation (3.45) (it is dependent on variables z and t) into a number of coupled nonlinear ordinary differential equations, each corresponding to motion of a single vortex element.

5.1.2 Method of solving the equations of motion

Test simulations, not presented in this thesis, revealed that numerical solution of vortex-nucleus system can exhibit instability for some values of parameters. To avoid instability problems, a reciprocal space representation for solving the discretized eq. (3.45) was utilized (no need for explicit evaluation of second derivative).

An algorithm for time integration of ODE equations with Backward Differentiation Formula was utilized (due to choice of Python programming language, class `scipy.integrate.ode` with integrator ZVODE [40] was adopted). According to documentaion it is Variable-coefficient Ordinary Differential Equation solver with fixed-leading-coefficient implementation.

Choice of implicit solver should definitely eliminate problems with instabilities due to possible stiffness of equation¹ (see appendix B) and allows setting higher Δt for time evolution.

Furthermore, ZVODE solver can adapt some of coefficients being evaluated during integration step and throws exceptions when the error estimate exceeds allowable restriction. Thus the issue of selection of time step Δt is greatly simplified.

¹Dispersion relation do not exclude coexistence of quickly and slowly oscillating modes — described situation is often referred as stiff system of equations.

5.1.3 Algorithm steps

It is convenient to explain steps of constructed algorithm with snippets of the code placed in listings 5.1 and 5.2. The detailed description is provided in lines starting with '#' symbol (marker of comment in Python language syntax).

Time integration is performed by class `scipy.integrate.ode` and only a suitable function calculating right hand side (RHS) of ordinary differential equation (ODE) need to be written. An example of this implementation is given in listing 5.1.

The prototype functions are implemented in self-prepared *Superfluid Vortex Filament Model* library (SVFM) and they can be import with module `cfunctions` after specifying location of the shared library `cfunctions.so`. Time evaluation of RHS of ODEs is crucial to performance of the whole simulations, thus the key parts were written exploiting C and Cython extensions to Python programming language (see sec. 5.2.1 for details).

```
1 # definitions of function evaluation RHS of ODE, cfunctions is a shared library
2 # containing c and cython functions
3 func = lambda t,x,rVN : cfunctions.multiple_impurities( t,x,
4                                         np.empty(2*N,dtype = np.complex128),
5                                         np.empty(N), np.empty(N), zv ,np.empty(N), np.empty(N),
6                                         2*np.pi*scipy.fftpack.fft freq(N, d=dz), fx , fy , fVN_params,
7                                         rVN, vext_x, vext_y, eta, T_estimated, kappa, rho )
8
9 # solution is stored in a numpy.array of length 2N
10 # first N elements stores Fourier transforms of x value of positions
11 # of vortex elements (u_x) second half of the array stores Fourier
12 # transforms of y value of positions of vortex elements (u_y)
13
14 # setting integrator of ODE
15 solver = ode(func).set_integrator('zvode',method='bdf') # class initialization
16 solver.set_initial_value(y0, time[0]) # setting initial u_x, u_y
17 solver.set_f_params( RCM ) # setting additional parameter to integrator
18 # in this case RCM is a np.array
19 # with positions of impurities
20
21 # this loop iterates over 'measurements' (times when saving vortex positions)
22 for it in range(nom-1):
23     # numpy.array time contains precalculated values of time points
24     # to evaluate vortex positions from their Fourier transfroms.
25
26     # this loop performs integration from time[it] to time[it+1]
27     while ( solver.successful() and (solver.t < time[it+1]) ):
28         sol = solver.integrate(solver.t+dt)
29
30     # number of vortex elements
31     N = sol.size // 2
32
33     # get positions of vortex elements and store them to file
34     # (with utilization of numpy.memmap)
35     sim_data[it+1,:N] = scipy.fftpack.ifft(sol[:N]).real
36     sim_data[it+1,N:] = scipy.fftpack.ifft(sol[N:]).real
37
38 # make sure that data are written to file (specific to numpy.memmap)
39 sim_data.flush()
```

Listing 5.1: Example of usage module `cfunctions` from library *SVFM* as an utility for constructing ODE suitable to integration by class `scipy.integrate.ode`.

An example of a function from `cfunctions.pyx` (file provided with the library, see sec. 5.2.1) with description of steps of algorithm is presented in listing 5.2.

Generally, the algorithm contains (in the order of following): evaluation of the vortex line elements positions and their derivatives (to compute angle between tangent vector), computation of the force in positions representation, transformation of the force by FFT to reciprocal space, evaluation of the RHS of the ODE equations in reciprocal representation.

```

1  # xk      — numpy.array that is processed by scipy.integrate.ode
2  # xk[:N] — Fourier transform of x positions of vortex line
3  # xk[N:] — Fourier transform of y positions of vortex line
4  # x,y      — memory buffers to store positions of vortex elements
5  # dx,dy    — memory buffers to store derivatives of positions of vortex elements
6  # dxdt    — memory buffer to store RHS of the ODE being solved
7
8
9  # get positions of vortex filaments (from their Fourier transforms)
10 x[:] = numpy.ascontiguousarray( numpy.real( numpy.fft.ifft(xk[:N]) ) )
11 y[:] = numpy.ascontiguousarray( numpy.real( numpy.fft.ifft(xk[N:]) ) )
12
13 # get Fourier transform of first derivatives of positions
14 dxdt[:N] = 1j*kz*xk[:N]
15 dxdt[N:] = 1j*kz*xk[N:]
16 dxdt[N//2] = 0
17 dxdt[N+N//2] = 0
18
19 # derivatives of u_x, u_y (obtained from their Fourier transforms)
20 dx = numpy.ascontiguousarray( numpy.fft.ifft(dxdt[:N]).real )
21 dy = numpy.ascontiguousarray( numpy.fft.ifft(dxdt[N:]).real )
22
23 # evaluate forces acting on a nucleus — example of calling C function
24 #
25 # cdef extern from "cfunctions.h" nogil:
26 #     void get_forces_multiple_impurities(
27 #         double* xV,double* yV,double* zV,double* dx,double* dy,double* rN,
28 #         double complex* fx,double complex* fy,double* fVN_params,int M);
29 #
30 # was called before.
31 # &x[0] is a C pointer to first element of data stored in numpy.array (cython specific)
32 get_forces_multiple_impurities(&x[0],&y[0],&z[0],&dx[0],&dy[0],&rN[0],&fx[0],
33                                         &fy[0],&fVN_params[0],rN.size)
34
35 # transform forces to Fourier space
36 fx = numpy.ascontiguousarray( numpy.fft.fft(fx) )
37 fy = numpy.ascontiguousarray( numpy.fft.fft(fy) )
38
39 # evaluate RHS of the ODE
40 for it in range(N):
41     dxdt[it] = ( Tv*kappa*kz[it]*kz[it]/(4.0*math.pi) *(-eta*xk[it] + 1.0*xk[N+it]) \
42                  + (-eta*fx[it] + 1.0*fy[it])/(rho*kappa) ) / (1.0 + eta*eta)
43     dxdt[N+it] = ( Tv*kappa*kz[it]*kz[it]/(4.0*math.pi) *(-1.0*xk[it] - eta*xk[N+it]) \
44                  + (-1.0*fx[it] - eta*fy[it])/(rho*kappa) ) / (1.0 + eta*eta)
45     dxdt[0]   += vext_x*N
46     dxdt[N]   += vext_y*N

```

Listing 5.2: Code snippet demonstrating evaluation of the RHS of discretized form of eq. (3.45). It is part of module *cfunctions* of library *SVFM*.

5.1.4 Scaling and execution time

Analysis of algorithm presented in sec. 5.1.3 contains of following elements:

- Summing two array, scalar multiplications, calculation of angles in eq. (4.3).
- The vortex-nucleus force computation — depends on several arrays of length N and have to be performed for M impurities — $N \cdot M$ scaling.
- Usage of FFT — $N \log N$ scaling.
- Solving the linear algebraic equations needed in case of Backward Differentiation Formula.

The final scaling is expected to be $\max[N \log N, NM]$, where N- number of the vortex elements, M- number of impurities.

Execution time was measured on machine with processor Intel(R) Core(TM) i7-4720HQ (2.60 GHz). The code exploited single core and was compiled with GCC 5.4.0. Single integration timestep took 36 ms and with average number of 1 000 000 steps to be performed a simulation takes about an hour.

Most of the simulations were performed on cluster DWARF at Faculty of Physics of Warsaw University of Technology. It is equipped with processors Intel(R) Xeon(R) CPU E5-2670 v2 (2.50 GHz) and compiler GCC 4.4.7. Many simulations were executed in parallel. It was noticed that the simulations for comparable number of time steps have taken about half a day. The significant increase of execution time is suspected to be connected with frequent saving data to files by large number of simultaneously working processes.

5.2 Software implementation

5.2.1 Applied programming tools and organization of code

Due to great simplification in code development and visualization of results a Python programming language with C and Cython extensions was chosen. A lot of work on this thesis was concentrated on investigation of various models approximating the full Vortex Filament approach. Thus flexibility together with reasonable execution time was taken into account when choosing the programming tools.

The organization of the code including C and Cython extensions is schematically explained in fig. 5.1. Great advantage is achieved due to the readability of a python code and possibility to benefit from large number of open source, convenient libraries for scientific data analysis or visualization. For purpose of this thesis following libraries were mostly exploited: Numpy [67], Scipy [40], Matplotlib [68] and MayaVi [69].

The code is available on website <https://github.com/KKobuszewski/svfm> and also included on a DVD disk attached to the thesis as a .zip file. The repository contains files with cfunctions.h and cfunctions.pyx that are automatically compiling to shared library cfunctions.so with python bindings through the command:

```
python setup.py build_ext
```

The shared library contains functions evaluating right hand side of discretized form of eq. (3.45). The author of thesis proposed name *Superfluid Vortex Filament Model* (SVFM) for the library.

Moreover some functions that facilitate saving and exploring data generated by execution of program are collected in file svfm_datautil.py (there are in example utilities to construct and read .xml files containing information on parameters used for simulation). The script setup.py is also attached to repository.

Shared library can be imported to any file processed by python interpreter and the functions that contains can be combined with any python library. Examples of scripts performing numerical simulations of vortex moving through a lattice of impurities (`simulation_bcc.py` and `simulation_fcc.py`) are included on a DVD disk attached to the thesis.

Some remarks on performance of code due to utilization of fragments written in C language are discussed in sec. 5.1.4.

5.2.2 General output from simulations

The result of execution of the prepared code were three files containing positions of vortex line in different time steps, positions of nuclei and .xml file containing information on parameters simulations.

Files with positions of nuclei and vortex elements are raw binary data and parameters needed to process data stored in these files have to be obtained from .xml file.

Nevertheless output of the simulation can be organized in another way by programmer, because scripts generating the output are independent on compiled modules of library SVFM.

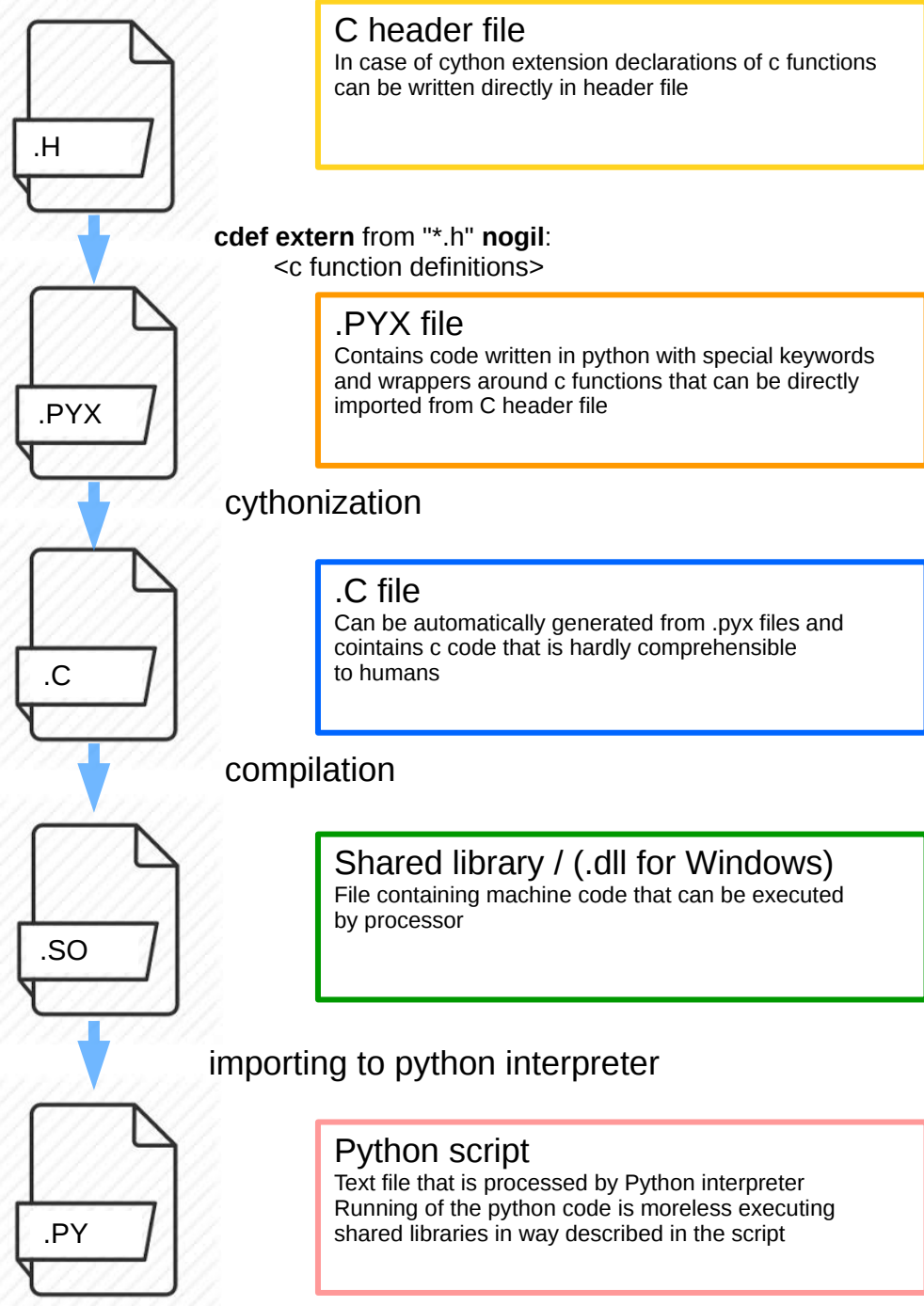


Figure 5.1: Schematical organization of Superfluid Vortex Filament Model (SVFM) program.

5.3 Verification of correctness of numerical simulations

5.3.1 Correctness tests

In order to confirm correctness of the computation, various test configurations were investigated, including:

1. No impurities and constant external flow (the results of this test are omitted).
2. Single impurity moving along same trajectory as in TDSLDA simulations (see sec. 4.1.2).

The comparison of data obtained in TDSLDA approach and results of SVFM simulations were performed only at qualitative level and no quantitative method was elaborated. This was caused because of essential discrepancy in details of the vortex motion in these two models. See fig. 5.2 and 5.3 for reference. Moreover, I do not expect to get very good agreement between the SVFM and the TDSLDA. In the second case the vortex was confined in a tube. It is reasonable to assume that the tube presence can generate noticeable effects in the vortex dynamics. Thus, one cannot directly compare mean square value of difference between a trajectory of the vortex obtained within these two different approaches.

5.3.2 Impact of time step and vortex elements spacing

In order to perform stable integration time step Δt and the vortex elements constant Δz have to be chosen carefully. Empirical validation of these parameters was made.

Various time steps in interval $1 \div 10$ fm/c where tested, but no qualitative changes of trajectory were observed. According to description of ZVODE algorithm in sec. 5.1.2 the method of integration should not be sensitive to small time step changes. Thus author of the thesis examined only if the ZVODE does not return errors for given configuration, set of parameters and time step. Detailed investigation of this issue was considered to be irrelevant.

Simulations of single vortex and single impurity reproducing the system evolved in TDSLDA simulations were performed for different vortex element spacing Δz and reduced dissipation parameter $\tilde{\eta}$. The nuclear impurity in the Vortex Filament Model is forced to move along the same trajectory as in the microscopic model. Analysis of vortex trajectories for different simulation parameters reveal no discrepancy due to tested values of vortex spacing. Some of the test cases were visualized on figures fig. 5.2 and 5.3. Vortex elements spacing assumed in TDSLDA simulation ($\Delta z = 1.5$ fm, see [20] for details) is also sufficient in context of stable calculations with the SVFM. Therefore in all other simulations, distance between two adjacent vortex elements was ensured not to exceed this limit.

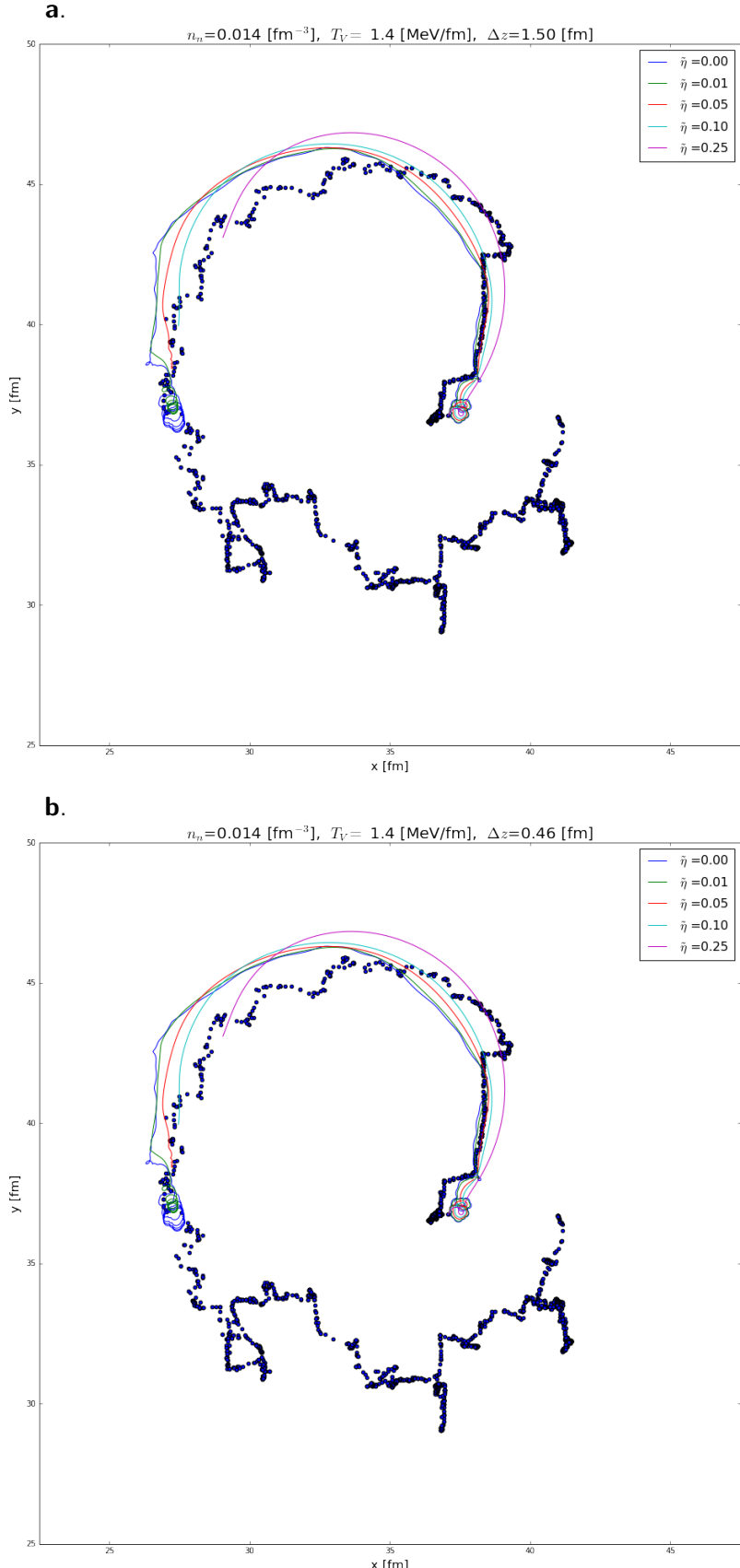


Figure 5.2: Solid lines represent trajectories of vortex $\mathbf{u}(z_{max}/2, t)$ in x,y plane obtained from simulations in Vortex Filament Model and scattered points represent corresponding vortex positions in TDSLDA simulations for neutron background density 0.014 fm^{-3} . In the insets a. and b. evolution for different computational grid step Δz is compared.

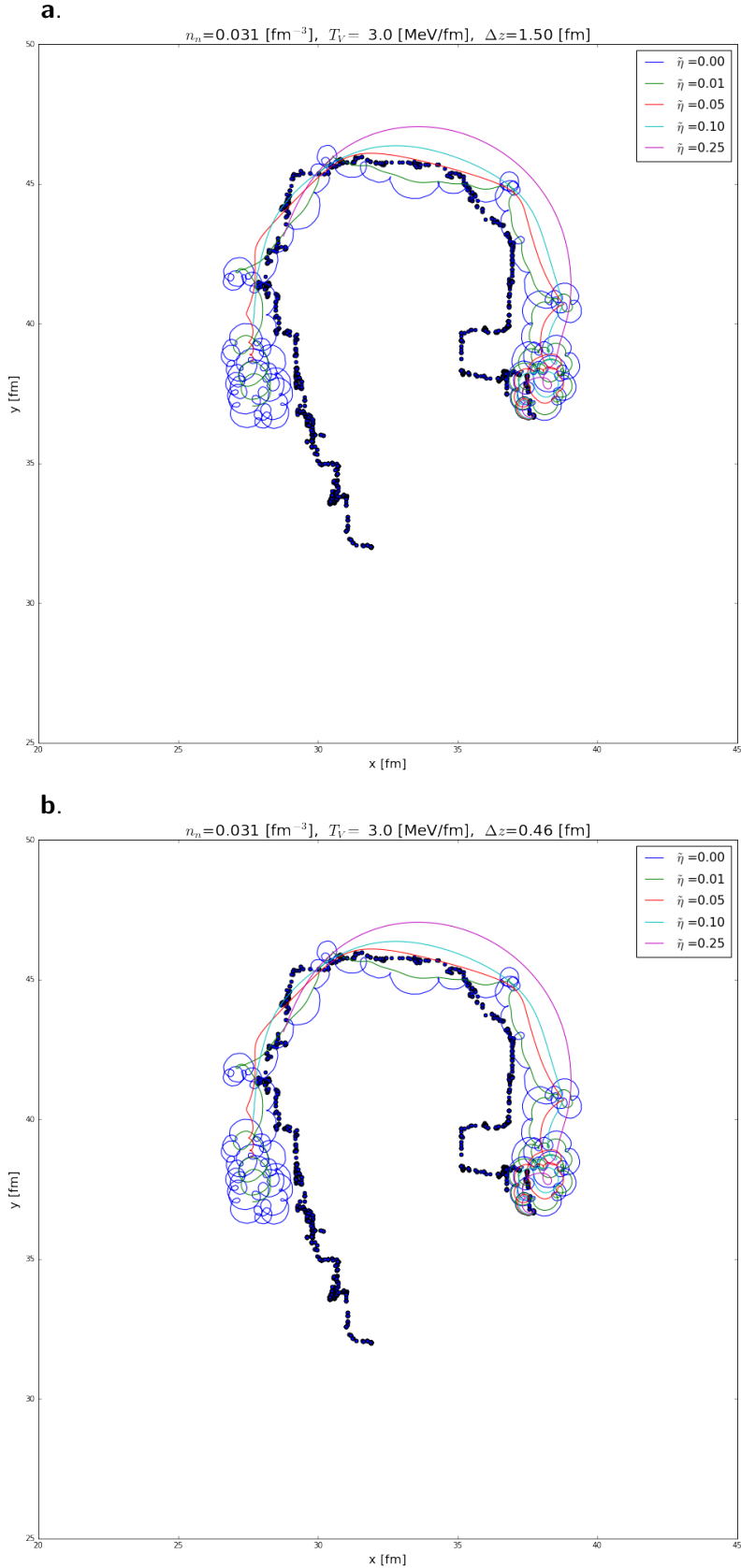


Figure 5.3: Solid lines represent trajectories of vortex $\mathbf{u}(z_{max}/2, t)$ in x, y plane obtained from simulations in Vortex Filament Model and scattered points represent corresponding vortex positions in TDSLDA simulations of vortex-nucleus system for neutron background density 0.031 fm^{-3} . In the insets a. and b. comparison of evolution for different computational grid step Δz is displayed. No noticeable changes in the trajectory are detected when changing Δz from 1.5 fm to 0.46 fm .

5.4 The planning of simulations imitating neutron star crust environment

5.4.1 Vortex-nucleus force parameters

In numerical simulations force given by eq. (4.2) with Padé approximant of order $n = 2$ was utilized. The parameters were taken according Ref. [20] and are presented in tab. 5.1.

Table 5.1: Tab. I. from supplementary material for article by G. Włazłowski et al. [20], showing Padé approximant coefficients of the vortex-nucleus force. These coefficients were utilized in numerical simulations presented here.

Neutron background den.	0.014 fm ⁻³	0.031 fm ⁻³
a_0 [MeV fm]	-4549.83	-3735.28
a_1 [MeV fm ⁻³]	-4525.79	- 988.42
a_2 [MeV fm ⁻⁴]	-505.60	-4257.99
b_1 [fm ⁻¹]	6455.46	6738.74
b_2 [fm ⁻²]	6299.41	8430.92
b_3 [fm ⁻³]	23440.34	35498.57
b_4 [fm ⁻⁴]	-5640.24	-7190.64
b_5 [fm ⁻⁵]	341.73	397.51

5.4.2 Other parameters of SVFM

Except the vortex-impurity force, in SVFM there are other parameters that needs to be provided. They are listed in table 5.2. Their values were chosen to be representative based on literature analysis.

Table 5.2: Comparison of the most important simulation parameters for two different neutron background particle densities n_n . For references see sec. 2.1.3, 2.1.4, 3.1.1, 3.4.3 and fig. 2.2.

n_n [fm ⁻³]	Δ [MeV]	$k_{F,n}$ [fm ⁻¹]	ξ_{BCS} [fm]	$R_{WS}^{\text{spherical}}$ [fm]	$a^{b.c.c.}$ [fm]	$a^{f.c.c.}$ [fm]	T_V [MeV fm]
0.014	2.00	0.75	2.47	25.0 \div 30.0	50.8 \div 60.9	64.0 \div 76.8	1.4
0.031	1.50	0.97	4.27	17.5 \div 22.5	35.5 \div 45.7	44.8 \div 57.6	7.3

Main motivation of this thesis is to provide answer if a quantum vortex can be pinned by lattice of impurities, assuming realistic vortex-impurity interaction. Thus, author decided to perform simulations for several sets of parameters which are expected to be the most important in context of the pinning problem.

As the most important parameter from pinning perspective (assuming that the vortex nucleus force is fixed) is expected to be the impurity lattice constant. Two types of lattices were investigated: f.c.c. or b.c.c., as described in section 2.1.4. Analysis of fig. 2.5 reveals that microscopic determination of the Wigner-Seitz cells parameters is attributed by significant uncertainty. It translates into uncertainties for $a^{b.c.c.}$ and $a^{f.c.c.}$, as shown in the table 5.2. Another parameter is reduced dissipation coefficient $\tilde{\eta}$, see eq. (3.29). It is purely phenomenological parameter and was assumed to be comparable with values used by B. Link in work [21], i.e. $\tilde{\eta} \approx 0.0 \div 0.1$.

5.4.3 Frame of reference

Typical superfluid model of neutron star glitch assumes that inside rotating star the global neutrons superflow (represented by external velocity field v_{ext}) is different from velocity of nuclei constructing lattice of impurities. In SVFM we work in reference frame where the impurity lattice is in rest. This eliminates an unknown velocity of the lattice.

Existence of the normal component in background sea of neutrons is taken into account implicitly, via dissipation force in form (3.26). This form of the dissipation contribution assumes that the velocity of the normal component is equal to global neutrons superflow v_{ext} , which seems to be reasonable approximation.

The unknown velocity of lattice can be also considered as an argument against dissipation force proposed by B. Link in article [21].

5.4.4 Configuration of the impurity lattice

As it was mentioned in sec. 2.1.4 two configurations of impurity lattice have to be considered — b.c.c. and f.c.c. lattice. To perform reliable simulations imitating neutron star crust environment we assumed periodicity along z direction (with period sufficient to enclose two primitive cells of lattice in this direction).

On the contrary to the vortex line, which periodicity is imposed by FFT algorithm utilization, the interaction effects are evaluated in positions representation (see sec. 5.1.3). Thus addition of layers of impurities imitating periodic boundary conditions on lattice is needed. Details can be seen in fig. 5.5

The volume of simulation box (outlined by white lines in fig. 5.4 and fig. 5.5) is large enough to contain many primitive cells. In this way realistic situation is imitated — motion of the vortex inside large lattice of impurities.

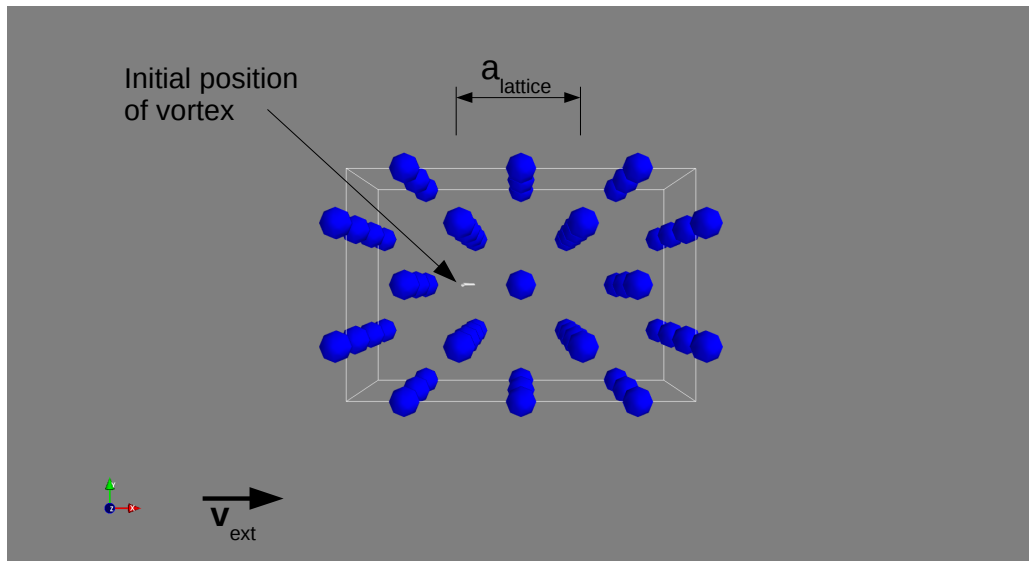


Figure 5.4: Example of initial configuration for simulation of vortex dynamics through a b.c.c. lattice of impurities. The simulation environment was planned in such a manner to allow the vortex to move one primitive cell of lattice along external flow direction.

In fig. 5.4 example initial configuration is presented: single quantum vortex immersed in lattice of impurities.

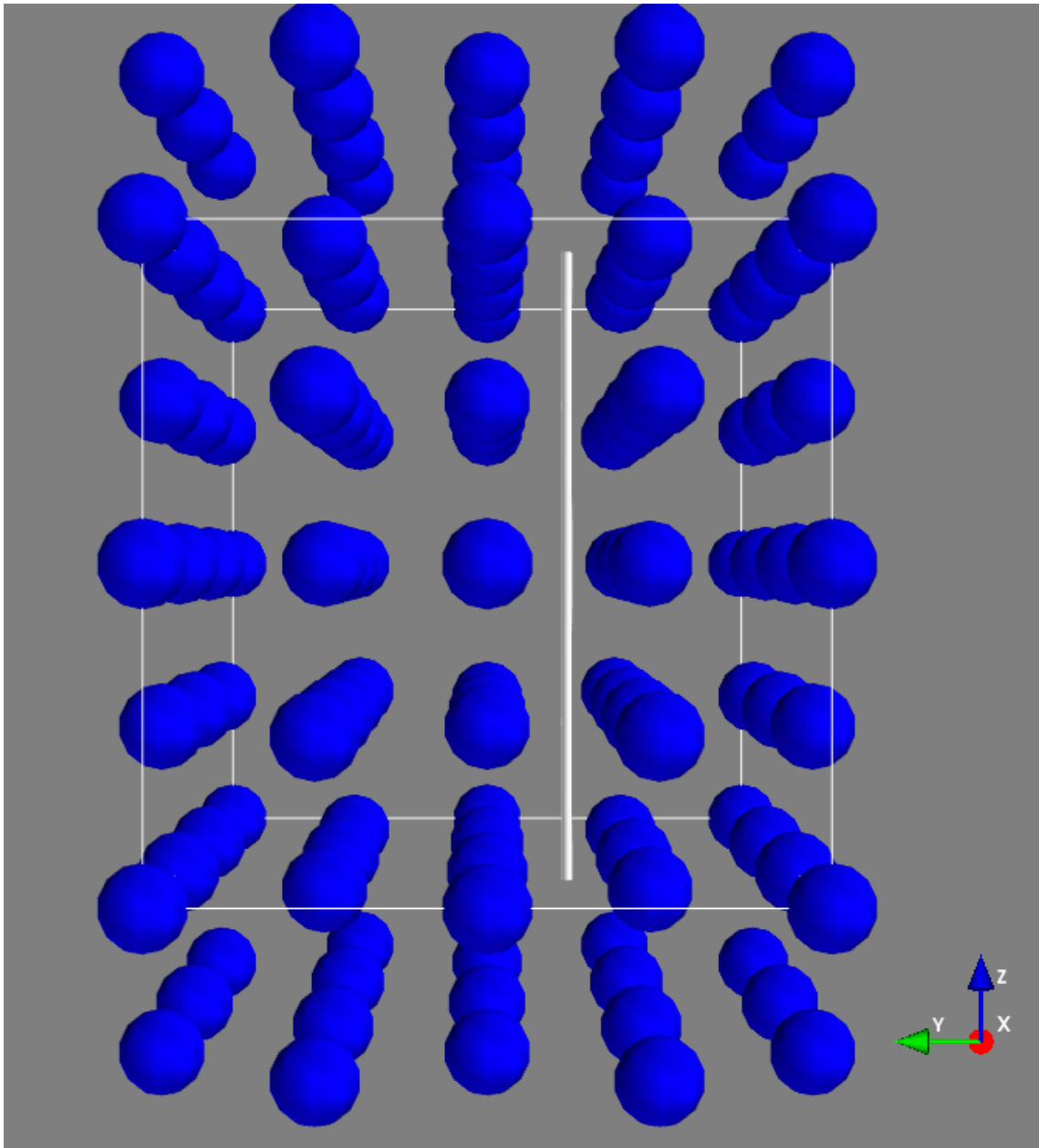


Figure 5.5: Forcing periodicity on vortex-nucleus force. The algorithm of solving SVFM equations assumes periodic boundary conditions along z-axis. We add extra impurities outside simulation box to impose the vortex-impurity interaction to be also periodic along z direction.

Chapter 6

Results of numerical simulations

6.1 System consisting of single vortex and single nucleus

6.1.1 Comparison of vortex-nucleus system evolution in TDSLDA to Vortex Filament Model simulations

Simulations with single vortex and single nucleus were performed to verify correctness of constructed theoretical approach. Comparison of results obtained by means of TDSLDA and SVFM provided also useful information about suitable ranges of phenomenological parameters.

This results were already mentioned in sec. 5.3, but it is needed to provide an additional comment here. Referring to fig. 5.2 and 5.3 one can justify that vortex motion in the SVFM simulations preserves main, qualitative features of the vortex motion in TDSLDA model. It is bending and rotating under interaction with impurity, excited of Kelvin waves are quickly suppressed. On quantitative level, the evolution in the SVFM results in significantly different trajectories (in terms of absolute values). Therefore the results of well-known methods for parameter fitting like least squares become unreliable for direct comparison of the two models. To investigate the dispersion relation of Kelvin waves (3.44) and reduced dissipation coefficient $\tilde{\eta}$, a spectral analysis of vortex motion was attempted, but it also failed, probably due to non-stationarity of the signal obtained from vortex positions. Only qualitative analysis of the Kelvin modes and dissipation was available. As a result only orders of magnitude were determined — see sec. 4.2 and 6.1.2.

Nevertheless, small numerical complexity of the SVFM code can be exploited. Large number of simulations for vortex immersed among many impurities can be preformed in reasonable time. This is advantage of the semi-classical description over microscopic description. The results of the simulations are presented in sec. 6.2, and in some cases they reveal surprising behaviour of the vortex line.

6.1.2 Spectrum of waves on a vortex line in SVFM simulations

In this section a spectrum of columnar vortex model with dispersion $\omega(k_z) \propto k_z^2$ is presented. Similarly to spectra of vortex motion obtained in TDSLDA approach (see sec. 4.1.2 and 4.2) the cutoff wavenumber k_z^{max} for excitations propagating along the vortex is present.

Qualitative analysis of fig. 6.1 implies that reduced dissipation coefficient $\tilde{\eta}$ should be of order of magnitude less than 0.01 (the most similar to TDSLDA results is spectrum for SVFM simulation with no dissipation $\tilde{\eta} = 0$)¹.

¹In mature neutron star the Fermi energy highly exceeds thermal excitations energy and thus amount of normal fluid is small in comparison to superfluid component. Thus vortex-phonon interaction should occur rarely and result in little dissipation, which is consistent with the result of SVFM simulation.

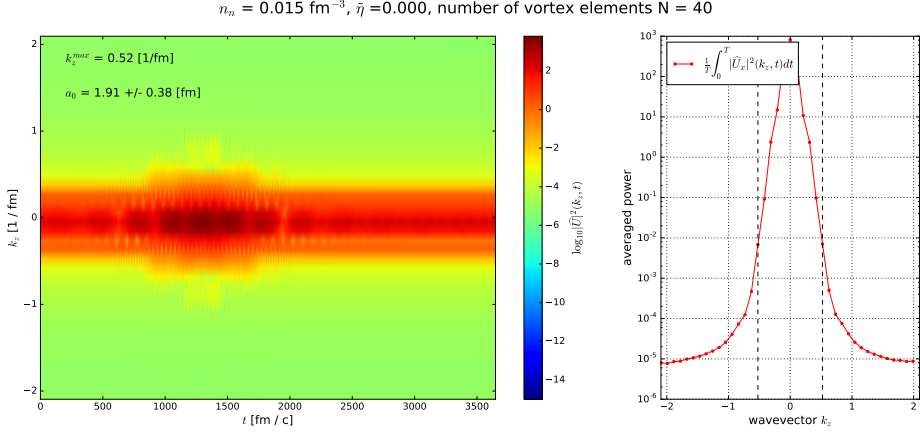
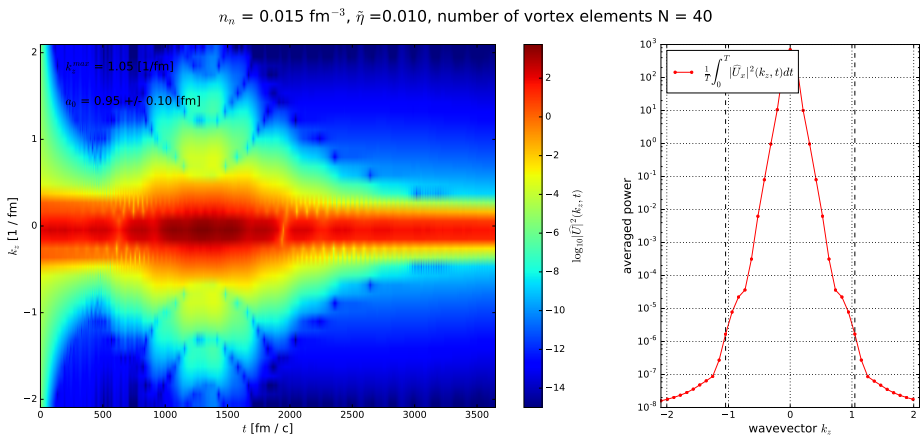
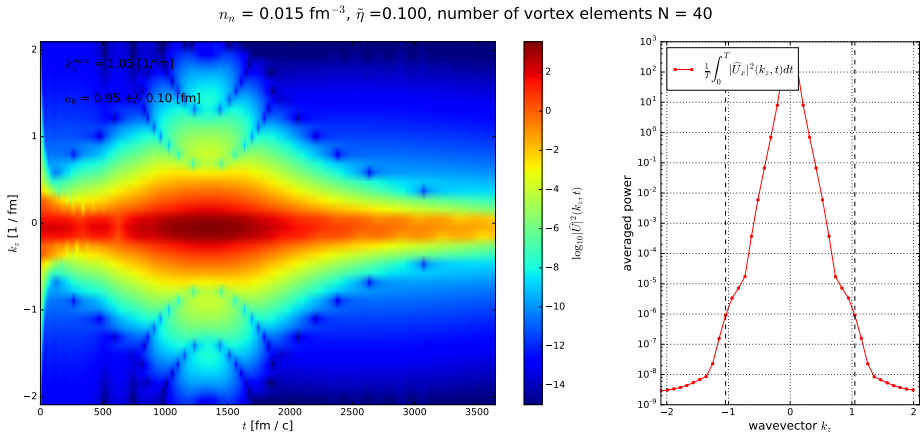
a.**b.****c.**

Figure 6.1: Spectrograms of vortex motion signal (see sec. 4.2 for definition) for different reduced dissipation coefficients $\tilde{\eta}$.

6.2 Simulations of vortex moving through a lattice of impurities.

6.2.1 General remarks on results of simulations

According to values of parameters presented in sec. 5.4.2 there were performed number of simulations.

Investigated ranges of the parameters:

- primitive cell constant $a^{latt.}$: $35 \div 60$ fm for b.c.c. lattice and $35 \div 45$ for f.c.c.;
- reduced dissipation coefficient $\tilde{\eta} \in [0.000, 0.001, 0.010, 0.100]$;
- external flow velocity v_{ext} for orders of magnitude $10^{-4} \div 10^{-3}$ c.

Moreover the simulations were repeated for two neutron background densities investigated throughout the thesis and whole set of cell sizes was investigated for both of these cases to better investigate the conditions under which the pinning can occur.

General output of simulation is visualized in fig. 6.2. As a main indicator of the vortex motion character a mean vortex velocity is considered:

$$\langle \dot{u} \rangle (t) = \frac{1}{z_{max} - z_{min}} \int_{z_{min}}^{z_{max}} \dot{u}(z, t) dz \quad (6.1)$$

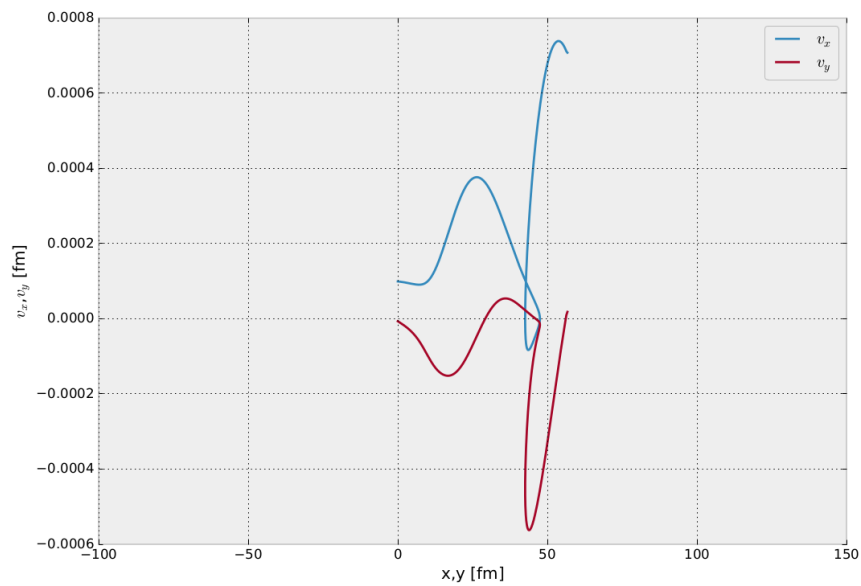
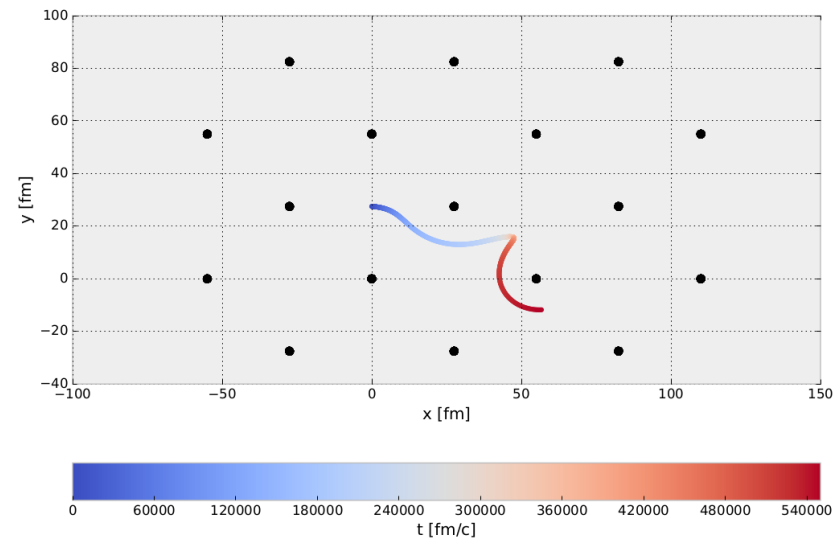


Figure 6.2: Visualization of an example trajectory with dependence on time indicated by changing color (upper inset) and velocity in dependence as s function of the vortex position (lower inset).

6.2.2 Types of trajectories observed in numerical simulations

Number of simulations with different velocity of external flow in frame of reference connected with lattice of impurities were performed. It was revealed that motion of the vortex through the lattice is changing character depending on the parameter values.

To discuss trajectories observed in numerical simulations we will refer to fig. 6.3. Three types of trajectories are observed in all performed simulations:

1. vortex stays trapped in position between impurities (black arrow in fig. 6.3);
2. vortex is moving through the lattice, but the direction of propagation is substantially different from direction of external flow (blue arrow in fig. 6.3);
3. vortex is moving through the lattice in same direction as external flow (red arrow in fig. 6.3).

The revealed phenomena of changing motion character seems to have features of phase transition, but further research is required to justify this conjecture.

6.2.3 Inspection of methods for evaluation mean vortex velocity

Two methods for calculation of mean vortex velocity were investigated.

The methods can be expressed by following formulas:

$$\frac{\Delta \langle |\mathbf{u}| \rangle}{\Delta t} = \frac{\langle |\mathbf{u}| \rangle(t_{max}) - \langle |\mathbf{u}| \rangle(t_0)}{t_{max} - t_0}, \quad (6.2a)$$

$$\frac{d\langle |\mathbf{u}| \rangle}{dt} = \frac{1}{\Delta t N} \sum_{i=1}^{N-1} \langle |\mathbf{u}| \rangle(t_i) - \langle |\mathbf{u}| \rangle(t_{i-1}) \quad (6.2b)$$

Where $\langle \cdot \rangle$ denotes averaging over z-axis and $\bar{\cdot}$ stands for averaging in time. The first formula indicates mean displacement during the simulation, while the second averages magnitude velocity vector over time. However, a note that for closed trajectories the mean vortex velocity can be still comparable to velocity of external flow is worth to be pointed.

Comparison of methods can be seen in fig. 6.4. Analysis of this figure suggest usage of $\frac{\Delta \langle |\mathbf{u}| \rangle}{\Delta t}$ because it better indicates pinned trajectories, which are of main interest in context of neutron star glitches.

The author of the thesis does not consider measures of displacement of mean vortex positions along x,y axis, because it unnecessarily complicates analysis (distinction between three types of trajectories can be done only by investigation of magnitude of the mean vortex velocity).

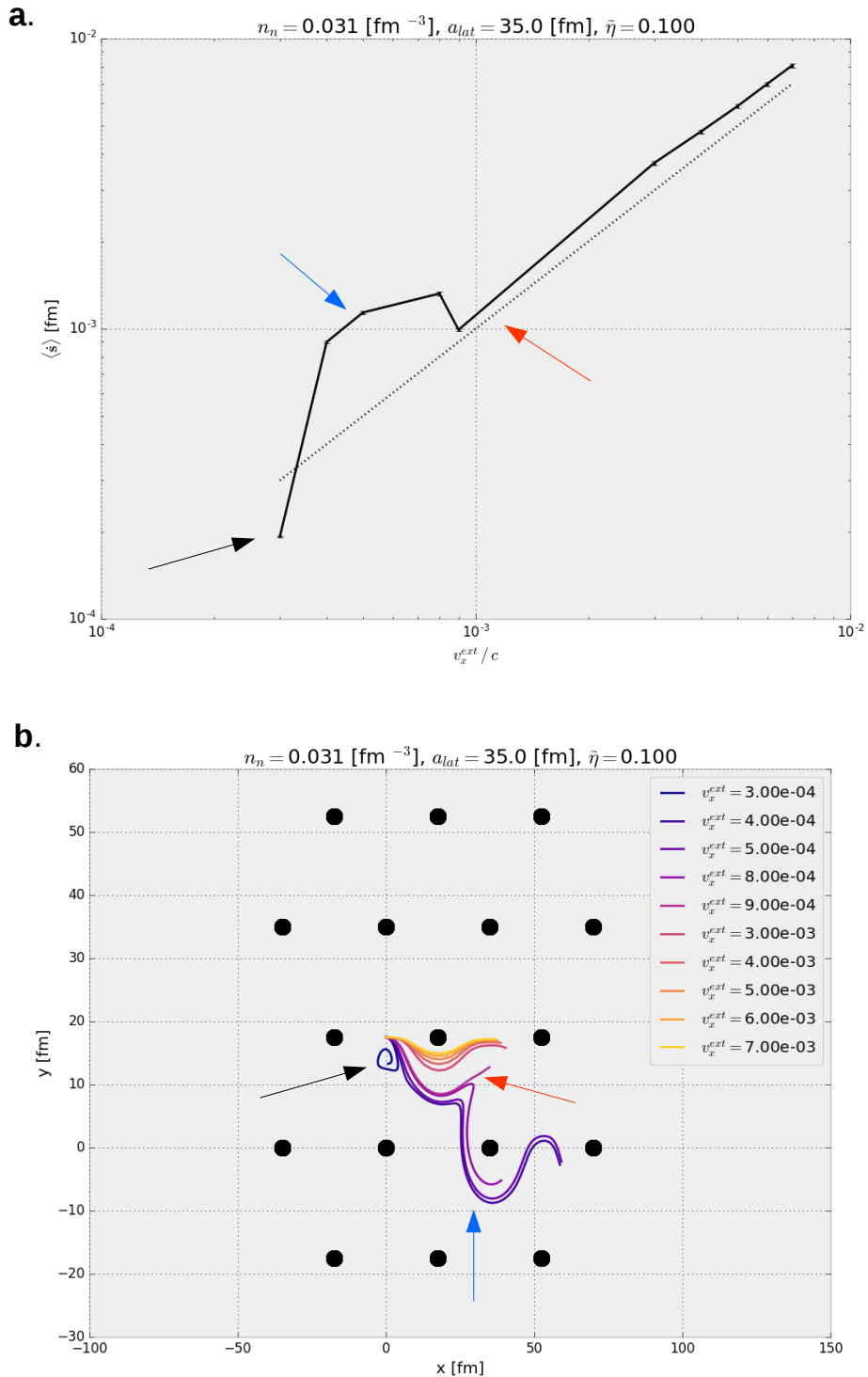


Figure 6.3: In inset a. mean velocity of the vortex line, calculated according formula 6.2a, as a function of the external flow velocity. In inset b. mean value of position of the vortex line. Position of impurities, projected on a plane, are marked by black dots. The arrows indicate three different types of trajectories: pinned (black), moving in same direction as external flow (red) and in another direction than external flow (blue).

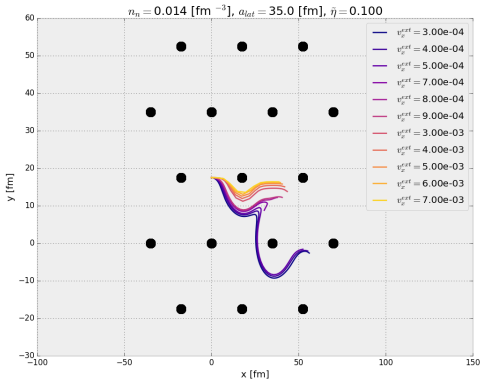
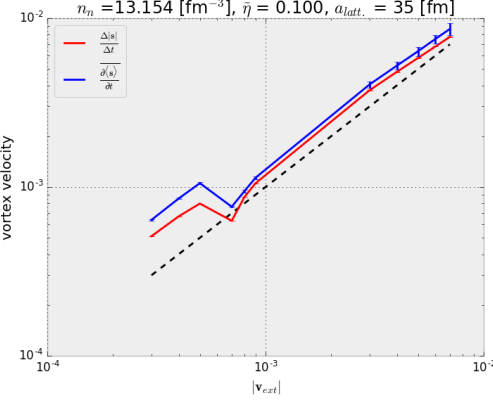
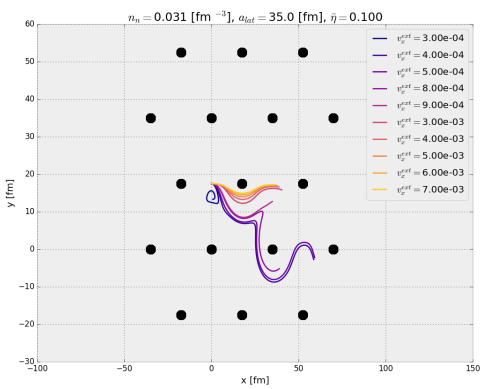
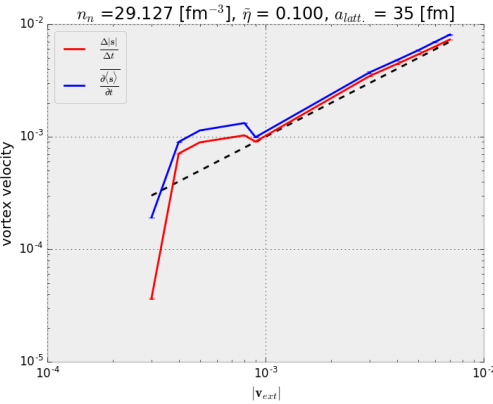
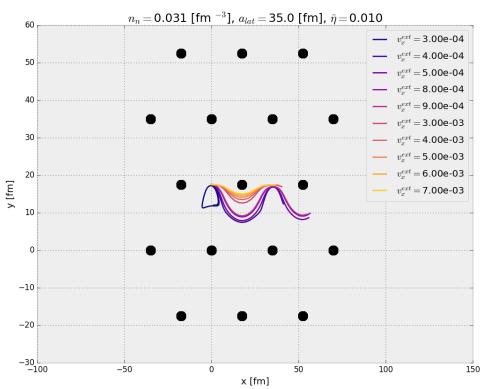
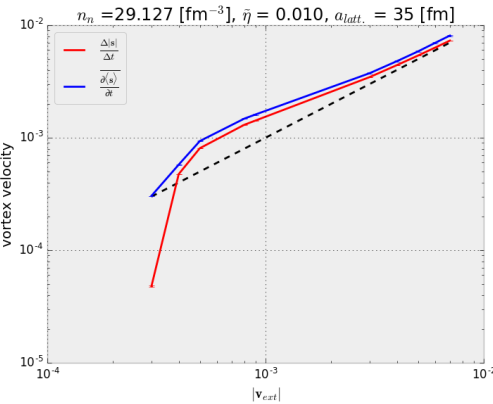
a.**b.****c.**

Figure 6.4: Comparison of methods for evaluation of the vortex mean velocity (plots on left insets) illustrated in three different cases (**a.,b.,c.**) of trajectories (plots on right insets). The results given as a function of external flow velocity. Comparison of cases **b.** and **c.** reveals that usage of $\frac{d\langle|u|\rangle}{dt}$ may not be sensitive indicator of pinned trajectory, because magnitude of mean velocity may not decrease while vortex is moving around closed trajectory.

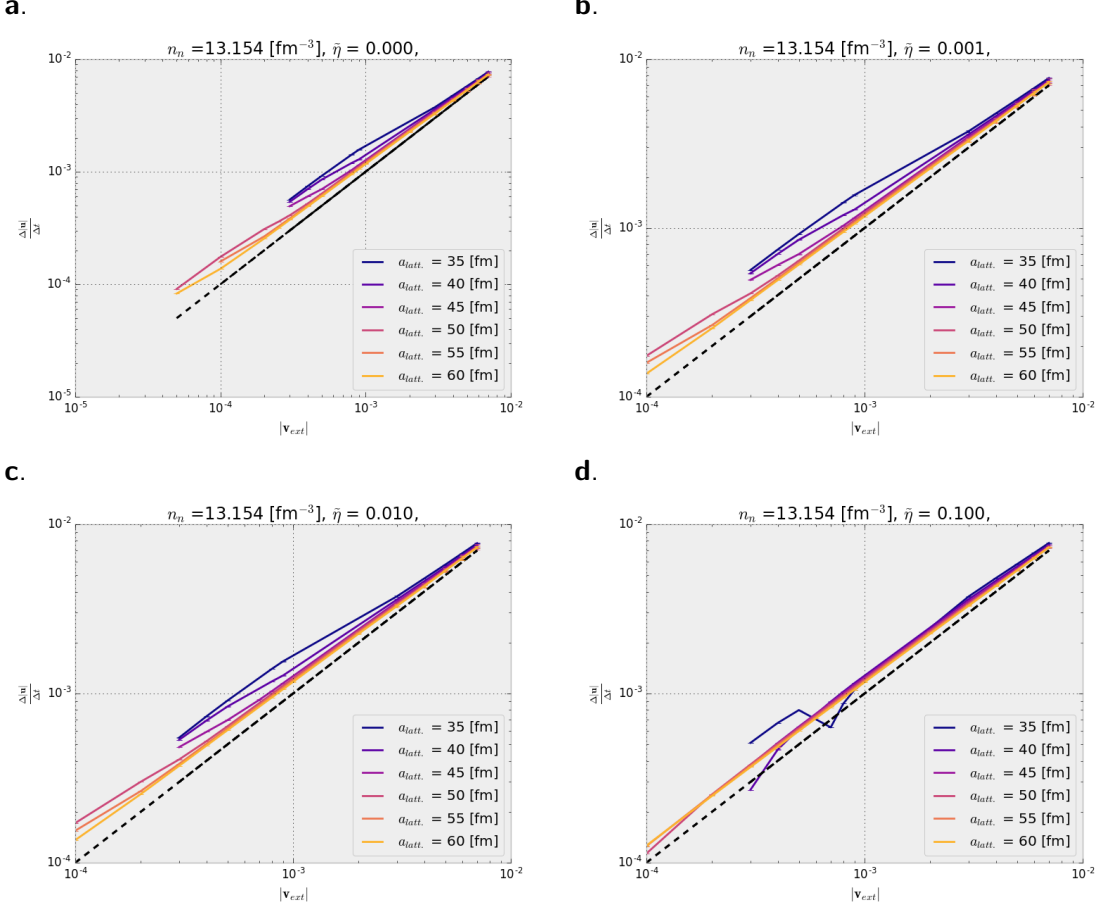


Figure 6.5: Mean vortex velocity as a function of external flow velocity, for $n_n = 0.014 \text{ fm}^{-3}$.

6.2.4 Analysis of factors affecting vortex motion through the lattice

In this section an analysis of fig. 6.5 and 6.6 is presented and the conclusions are given without further references to the figures.

Size of primitive cells of impurity lattice is suspected to have the main impact on the vortex pinning, because it is connected with average magnitude of the vortex-nucleus force exerted on the line. Numerical simulations confirm this expectation. In case of b.c.c. lattice only for primitive cells constants $a^{latt.} = 35 \text{ fm}$ and higher neutron background density $n_n = 0.031 \text{ fm}^{-3}$ the trapped vortices inside the lattice cells are observed.

The vortex pinning occurs irrespectively to reduced dissipation coefficient. However, for high dissipation case $\tilde{\eta} = 0.1$ and both neutron background densities there appears a sharp deviation for value of $\frac{\Delta\langle|u|\rangle}{\Delta t}$ at external flow velocity v_{ext} corresponding to transition between trajectories of types 2. and 3., described in sec. 6.2.2.

The mentioned transition point is moving toward $v_{ext} \rightarrow 0$ as a function of primitive cell size $a^{latt.}$, thus it is expected to encounter transition to pinned trajectories for sufficiently small external flow velocities for b.c.c. with cell constants larger than 35 fm.

In regime of tight lattice the pinning is observed for external flow velocities smaller than $v_{ext} \leq 3 \cdot 10^{-4}c$, which can be considered as a restrictive condition. However, note that the v_{ext} is velocity of the fluid with respect of the frame of reference moving with lattice (see sec. 5.4.3).

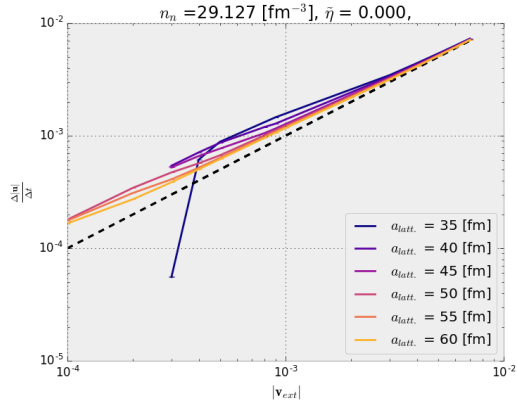
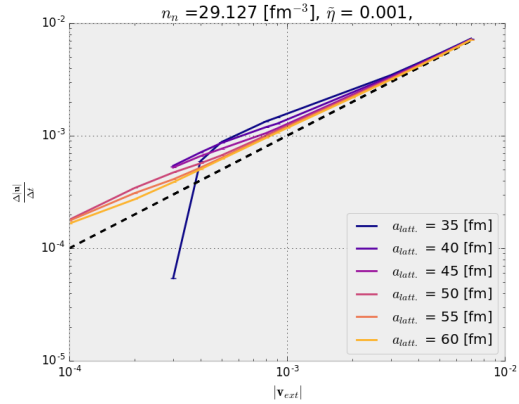
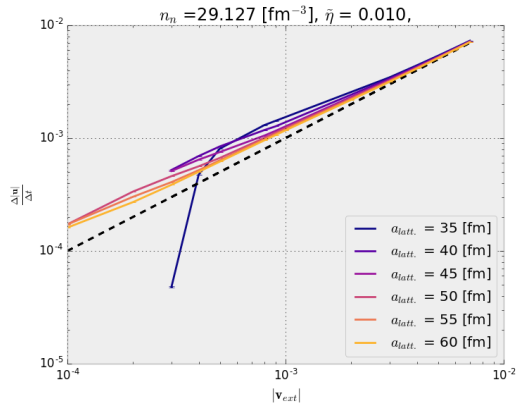
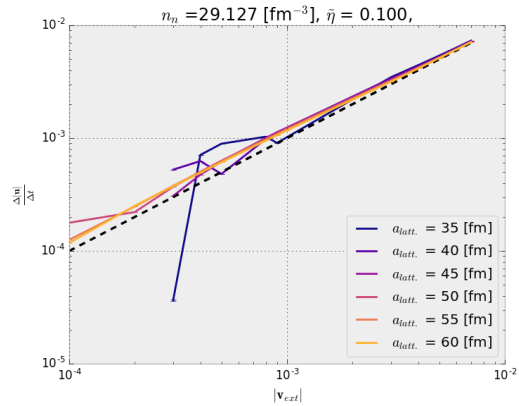
a.**b.****c.****d.**

Figure 6.6: Mean vortex velocity as a function of external flow velocity, for $n_n = 0.031 \text{ fm}^{-3}$.

6.3 Impact of configuration of impurity lattice on vortex motion

Numerical simulations presented in sec. 6.2 were repeated for f.c.c. lattice configuration revealing possibilities of more complex behaviour of the vortex line. This indicates relevant affection of the space configuration of impurities on the phenomena.

According to fig. 6.7 (inset d.) still pinned trajectories can be obtained for sufficiently slow external flow velocity v_{ext} . In case of neutron background density $n_n = 0.031 \text{ fm}^{-3}$ the pinning is seen for $v_{ext} \leq 1 \cdot 10^{-4}c$.

However, even more interesting result was obtained in case of neutron background density $n_n = 0.014 \text{ fm}^{-3}$ and smaller lattice constant $a^{latt.} = 35 \text{ fm}^2$ presented in fig. 6.8. The transition phase between pinning and quasi-free motion of vortex line has features of random walk from one to another site of the impurity lattice. However justification of this conjecture requires further research.

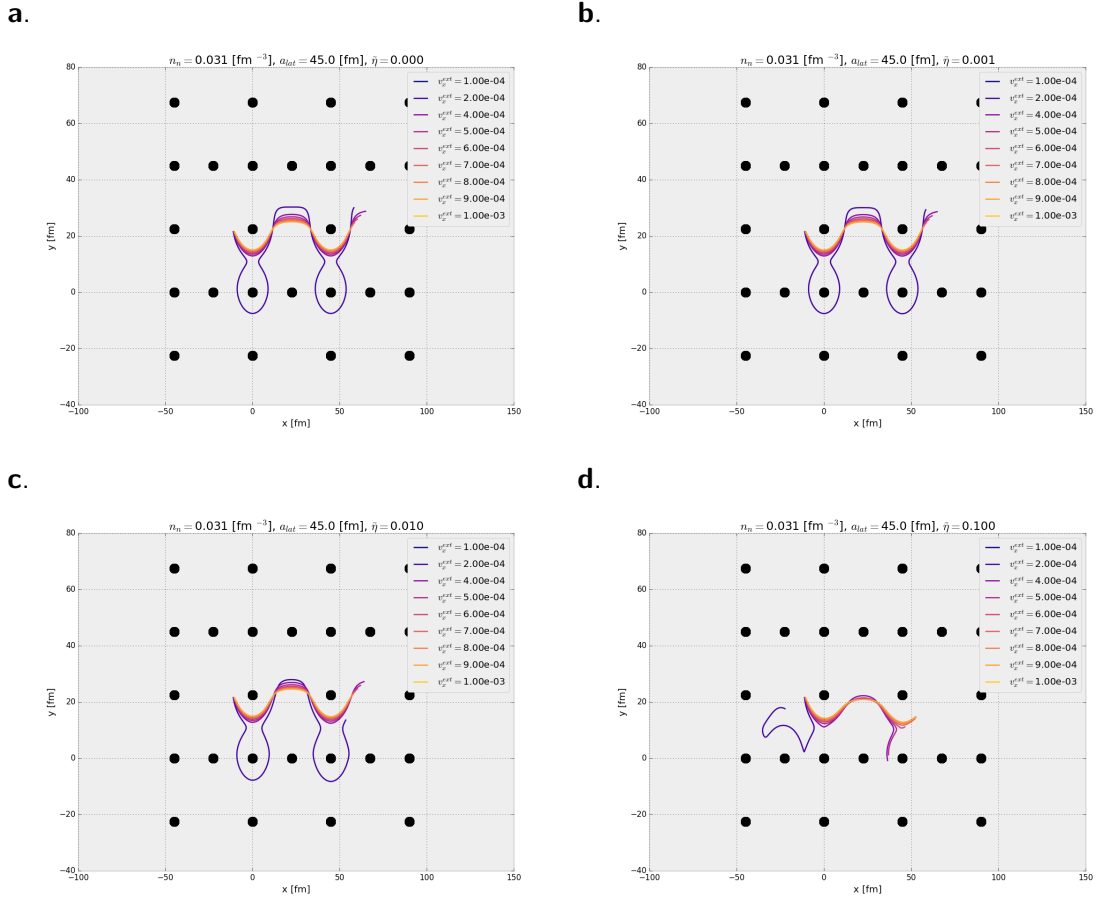


Figure 6.7: Trajectories of mean position of vortex moving through the f.c.c. lattice obtained for neutron background density $n_n = 0.031 \text{ fm}^{-3}$. Insets a. - d. presents results for different reduced dissipation coefficients $\tilde{\eta} \in 0.0 \div 0.1$. Lattice constant $a_{latt.}^{f.c.c.} = 45 \text{ fm}$ corresponds to Wigner-Seitz cell radius for b.c.c. lattice with $a_{latt.}^{b.c.c.} = 35$. Compare the lattice size with sec. 2.1.4 and tab. 5.2.

²According to results presented in sec. 2.1.4, 2.5 and tab. 5.2 the value of lattice constant of 35 fm is unphysical in case of f.c.c. configuration, but the author of the thesis considers that for smaller external flow velocities v_{ext} similar results can be obtained with bigger lattice constants.

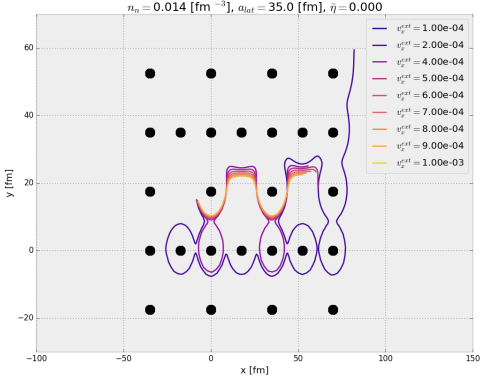
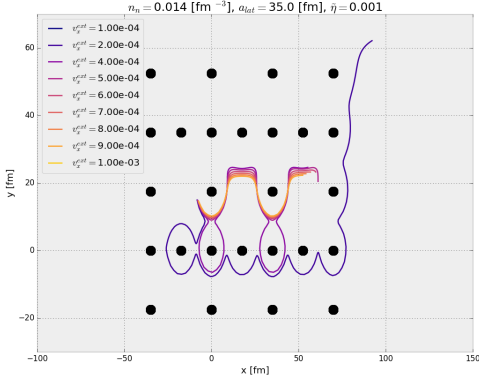
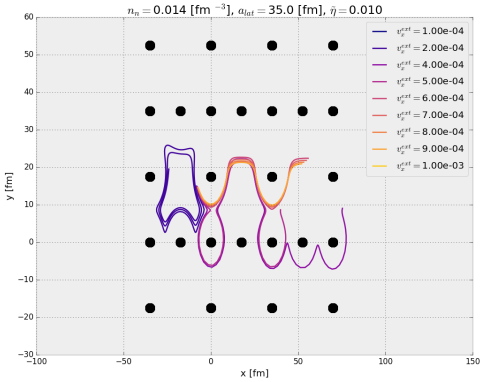
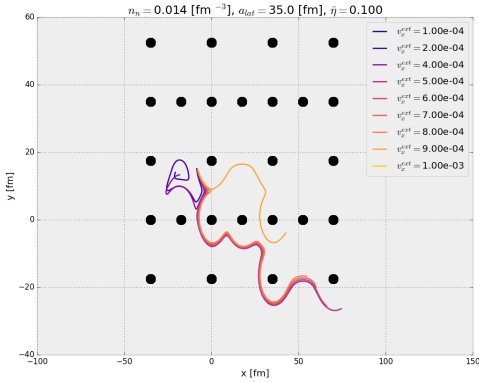
a.**b.****c.****d.**

Figure 6.8: Trajectories of mean position of vortex moving through the f.c.c. lattice obtained for neutron background density $n_n = 0.014 \text{ fm}^{-3}$. Insets **a.** - **d.** presents results for different reduced dissipation coefficients $\tilde{\eta}$ $0.0 \div 0.1$. A regime of extremely tight lattice with $a^{latt.} = 35 \text{ fm}$ is presented due to the widest number of types of vortex behaviour obtained. Compare the lattice size with sec. 2.1.4 and tab. 5.2.

Chapter 7

Resume of numerical simulations, conclusions and further research proposal

7.1 Conclusions

7.1.1 Theoretical part of work

The first conclusion obtained during my work on the thesis, was a fact that deeper insight on both quantum microscopical and semi-classical theories are required to choose appropriate approximation for vortex equation of motion in Vortex Filament Model. Many misleading statements found in various papers (cited in rich bibliography) caused great enlargement of this part of the thesis, but also enabled better understanding of the results.

In section 3.4.2 range of applicability of the Local Induction Approximation was investigated. I find this approximation to be very cumbersome from point of view of numerical simulations, if the vortex line is parametrized by coordinate on z-axis with forced periodicity along this axis. For this reason, I excluded this approximation from my model. In fact, the Local Induction Approximation generates a lot of problems when applied to almost straight lines, which have been omitted in the literature.

An approximation suitable for purpose of this thesis research was found. It appeared to be the columnar vortex approximation, proposed by Lord Kelvin in nineteenth century in work about helical waves propagating along vorticity line in classical hydrodynamics. Providing an experimental dispersion relation $\omega(k_z)$ for these waves and exploiting eq. (3.47) is considered to be more reliable than the classical Vortex Filament Model, due to number of approximations needed for its derivation.

An attempt to extract $\omega(k_z)$ from data for the vortex motion obtained within TDSLDA simulations resulted in no quantitative outcome. Data provided by authors of paper [20] are probably not suitable for this aim — the TDSLDA simulation was constructed to obtain vortex-nucleus force, which causes vortex to bend and rotate and thus the signal of vortex motion is highly non-stationary.

7.1.2 Summary of numerical simulations

About 1000 simulations for different sets of parameters were performed in period of time not exceeding a week (however some of the simulations were conducted in parallel), thus author of the thesis considers that aim of providing a model of low numerical complexity was achieved. Further development of the programs can result in new framework for large-scale simulations suitable for investigation of neutron star crust hydrodynamics.

The two main remarks revealed by numerical simulations analysis are:

- Vortex pinning can occur in system with vortex-nucleus repelling for sufficiently small values of the external flow velocity v_{ext} (that is given in frame of reference connected with lattice moving with unknown velocity, see sec. 5.4.3 for discussion). The precise value of v_{ext} , below which the transition to pinned state occurs, depends on mean impurity spacing, configuration of lattice of impurities and strength of dissipation force acting on a vortex line.
- Form of the dissipation force is not negligible. It is because trajectories of vortex line obtained with assumption of force in form (3.26) present essentially different features than trajectories appearing for force (3.27) utilized in work of B. Link [21].

Further conclusions should not be drawn without further research, because only specific initial configurations of the vortex immersed among impurities were investigated. Especially time and length scales of simulations are not sufficient to predict impact of obtained results on neutron star glitches theory.

7.2 Further research proposal

In opinion of the author of this thesis, a main result revealed by numerical simulations are transitions between three regimes of the vortex motion. Thus some issues affecting existence of these regimes have to be investigated deeper:

1. Since consistency of dynamics VFM with TDSLDA simulations was only qualitatively tested some effort to obtain quantitative methods — if the VFM does not include some important features of microscopic model it cannot be considered as a trustworthy approach to the hydrodynamics of neutron superfluid.
2. Comparison of result of this thesis to results of B. Link shows that influence of dissipative force cannot be treated as insignificant matter, thus its correct form should be elaborated. The dispersion relation for Kelvin waves should also be tested more carefully. Concerning these two matters, it is recommended to perform more microscopical simulations (i. e. within TDSLDA approach), targeted precisely into studies of waves propagating along the vortex line.
3. One should also research features of transitions between different types of trajectories. Moreover, an investigation of impact of the trajectories types on neutron star glitches phenomenon may be interested and probably large-scale hydrodynamic simulations should be performed to achieve this aim.

Appendix A

Mathematical description of curves

A.1 Natural parameter of a curve

Any curve in \mathbb{R}^n can be described as a vector dependent of single parameter $p \in [a, b] \subset \mathbb{R}$:

$$\mathbf{s}(p) = [s_x(p), s_y(p), s_z(p)] \quad (\text{A.1})$$

Length of an infinitesimal arc element of the curve is given by

$$dl = \sqrt{\left(\frac{ds_x}{dp}\right)^2(p) + \left(\frac{ds_y}{dp}\right)^2(p) + \left(\frac{ds_z}{dp}\right)^2(p)} dp \quad (\text{A.2})$$

Natural parameter of a curve is called a variable representing a length of curve:

$$\zeta = \int_a^p \left\| \frac{d}{dp} \mathbf{s}(p') \right\| dp' \quad (\text{A.3})$$

Choosing a natural parameterization is called a mapping $p \mapsto \zeta$ (inverse mapping exists and is corresponding to fixing a general parameterization).

Parameterization by ζ gives the simplest form of equations describing a curve, but commonly is not useful in numerical applications.

A.2 Frenét vectors

Frenét–Serret formulas given in natural (arclength - denoted by ζ) parameterization of curve:

$$\hat{\mathbf{t}} = \mathbf{s}'(\zeta, t) \quad (\text{A.4})$$

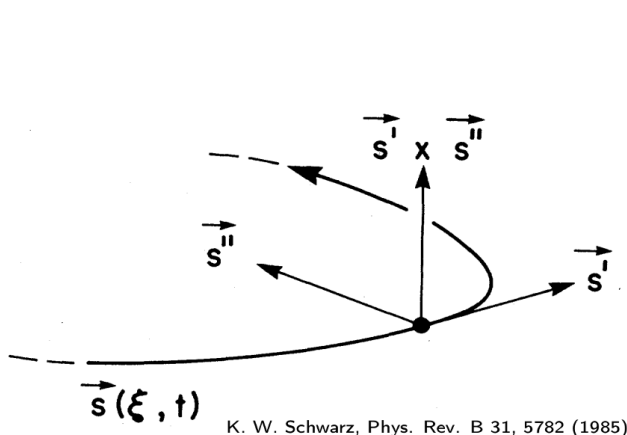
$$\hat{\mathbf{n}} = \frac{\mathbf{s}''(\zeta, t)}{\|\mathbf{s}''(\zeta, t)\|} - \underbrace{\langle \mathbf{s}''(\zeta, t), \mathbf{s}'(\zeta, t) \rangle}_{=0} \hat{\mathbf{t}} \quad (\text{A.5})$$

$$\hat{\mathbf{b}} = \hat{\mathbf{t}} \times \hat{\mathbf{n}} \quad (\text{A.6})$$

In this case binormal vector is easy to compute:

$$\hat{\mathbf{b}} = \hat{\mathbf{t}} \times \hat{\mathbf{n}} = \mathbf{s}'(\zeta, t) \times \frac{\mathbf{s}''(\zeta, t)}{\|\mathbf{s}''(\zeta, t)\|}$$

a.



K. W. Schwarz, Phys. Rev. B 31, 5782 (1985)

b.

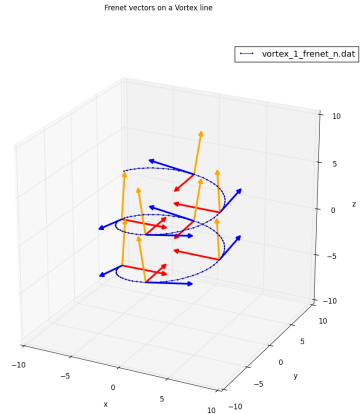


Figure A.1: Frénet frame of reference in natural parameter description (inset a.) and visualization of Frénet vector for helix (inset b., blue, red and orange lines correspond to tangent, normal and binormal vectors, respectively).

Now we consider Frénet–Serret basis vectors for a curve parameterized by value of z coordinate:

$$\hat{\mathbf{t}} = \mathbf{s}'(\zeta, t) = \frac{1}{\|\mathbf{dl}\|} \frac{\partial \mathbf{s}(z, t)}{\partial z} = \frac{1}{\sqrt{s_x'^2(z, t) + s_y'^2(z, t) + 1}} [s_x'(z, t), s_y'(z, t), 1] \quad (\text{A.7a})$$

$$\hat{\mathbf{n}} = \mathbf{s}''(\zeta, t) = \frac{\mathbf{s}''(z, t) - \langle \mathbf{s}''(z, t), \mathbf{s}'(z, t) / \|\mathbf{dl}\| \rangle \hat{\mathbf{t}}}{\|\mathbf{s}''(z, t) - \langle \mathbf{s}''(z, t), \mathbf{s}'(z, t) \rangle \hat{\mathbf{t}}\|} \quad (\text{A.7b})$$

$$\hat{\mathbf{b}} = \hat{\mathbf{t}} \times \hat{\mathbf{n}} = \frac{1}{\sqrt{s_x'^2(z, t) + s_y'^2(z, t) + 1}} [s_x'(z, t), s_y'(z, t), 1] \times [\hat{n}_x, \hat{n}_y, \hat{n}_z] \quad (\text{A.7c})$$

The Frénet vectors become quite complicated, so that for numerical issues we can evaluate expression

$$\begin{aligned} \mathbf{s}''(z, t) - \langle \mathbf{s}''(z, t), \mathbf{s}'(z, t) / \|\mathbf{dl}\| \rangle \hat{\mathbf{t}} = \\ \left[s_x'' - \frac{s_x'' s_x' + s_y'' s_y'}{s_x'^2 + s_y'^2 + 1} s_x', s_y'' - \frac{s_x'' s_x' + s_y'' s_y'}{s_x'^2 + s_y'^2 + 1} s_y', - \frac{s_x'' s_x' + s_y'' s_y'}{s_x'^2 + s_y'^2 + 1} \right] \end{aligned}$$

and normalize it to get normal vector $\hat{\mathbf{n}}$. Further we can use $\hat{\mathbf{n}}$ for evaluation of binormal vector $\hat{\mathbf{b}}$:

$$\hat{\mathbf{b}} = \begin{vmatrix} \hat{\mathbf{x}} & \hat{\mathbf{y}} & \hat{\mathbf{z}} \\ \frac{\partial s_x(z, t)}{\partial z} & \frac{\partial s_y(z, t)}{\partial z} & 1 \\ \hat{n}_x & \hat{n}_y & \hat{n}_z \end{vmatrix} = \frac{1}{\sqrt{s_x'^2(z, t) + s_y'^2(z, t) + 1}} [s_y' \hat{n}_z - \hat{n}_y, \hat{n}_x - s_x' \hat{n}_z, s_x' \hat{n}_y - s_y' \hat{n}_x]$$

(vector $\hat{\mathbf{b}}$ is needed for computation of vortex's self-induced velocity field in LIA, look section 3.4.2).

Torsion and curvature of a curve are given respectively by:

$$\tau =$$

(A.8)

$$\kappa(z, t) == \frac{\|\mathbf{s}'(z, t) \times \mathbf{s}''(z, t)\|}{\|\mathbf{s}'(z, t)\|^3} = \frac{\sqrt{(z''y' - y''z')^2 + (x''z' - z''x')^2 + (y''x' - x''y')^2}}{(x'^2 + y'^2 + z'^2)^{3/2}},$$

(A.9)

Notice that $z' = 1$ and $z'' = 0$.

Radius of curvature is defined as inversion of curvature:

$$\mathcal{R} = \frac{1}{\kappa}$$

A.3 Frenét-Serret formulas

Frenét vectors are related by Frenét-Serret equations:

$$\begin{aligned} \frac{d\hat{\mathbf{t}}}{d\zeta} &= \kappa \hat{\mathbf{n}} \\ \frac{d\hat{\mathbf{n}}}{d\zeta} &= -\kappa \hat{\mathbf{t}} + \tau \hat{\mathbf{b}} \\ \frac{d\hat{\mathbf{b}}}{d\zeta} &= -\tau \hat{\mathbf{n}} \end{aligned} \quad (\text{A.10})$$

One can determine $\hat{\mathbf{t}}$, $\hat{\mathbf{n}}$, $\hat{\mathbf{b}}$ at point $\zeta + d\zeta$ having these vectors at point ζ with exclusion of the inflection points — points where the second derivative with respect to natural parameter of a curve is equal to zero. In inflection points the curvature is equal 0, so the first of equations (A.10) does not determine the normal vector so binormal vector also cannot be calculated. Moreover numerical computation of Frénet vectors can be highly non-stable for almost straight curve due to finite precision of floating-point numbers.

In inflection points the curve is locally straight, so we cannot establish a direction of normal and binormal vector as well as for simple straight line.

Appendix B

Stability of numerical methods for solving ODEs

B.1 Definition of stability for numerical schemes

To investigate the stability of numerical methods a simple test ODE is provided in form:

$$\dot{y}(t) = \lambda y(t), \quad y : \mathbb{R} \rightarrow \mathbb{C}, \lambda \in \mathbb{C}$$

If real equation $\dot{y}(t) = f(y(t))$ has the property $\forall_{t \in \mathbb{R}} |f(y(t))| \leq |\lambda y|$ and numerical method provides stable solution for test equation (see definitions below), it is expected that a solution of real equation using numerical method converges to true solution of the equation.

B.1.1 Stability function of a numerical method

Numerical scheme for linear ODE can be expressed as:

$$y_{n+1} = \phi(\lambda \Delta t) y_n$$

where ϕ is called stability function.

B.1.2 A-stable methods

If the numerical method applied to the test equation with subject to the initial condition $y(0) = 1$ exhibits the behaviour that solution of this equation ($y(t) = e^{\lambda t}$) approaches zero as $t \rightarrow \infty$ when $\text{Re}(\lambda) < 0$, then the method is said to be A-stable.

In terms of stability function it means that for test equation $y_n = (\phi(\lambda \Delta t))^n \cdot y_0 \rightarrow 0$ as $n \rightarrow \infty$ or equivalently $|\phi(\lambda \Delta t)| < 1$.

Commonly only A-stability is required to get reliable solution of ODEs.

B.1.3 L-stable methods

A method is L-stable if it is A-stable and stability function has the property $\phi(z) \rightarrow 0$ as $z \rightarrow \infty$.

Note that a numerical method that is L-stable has the stronger property that the solution approaches zero in a single step as the step size goes to infinity. L-stable methods are in general very good at integrating stiff equations and exploited ZVODE solver belongs to this class.

List of Figures

1.1	Pulsar schematic	18
1.2	Hierarchy of models in neutron stars physics.	20
2.1	Structure of neutron star interior	25
2.2	Superfluidity in Neutron Stars	26
2.3	Number of protons inside nucleus in dependence on baryon density (in neutron star crust)	27
2.4	Parameters of matter in neutron star crust with respect to neutron background density	28
2.5	Dependence of Wigner-Seitz cell radius on baryon density in the neutron star's inner crust	29
2.6	Changes of rotation period of neutron star	30
2.7	Vortices in neutron stars	31
2.8	Two rectilinear vortices energy	32
3.1	Vortex structure in neutron matter.	36
3.2	Illustration of problems of Local Induction Approximation	46
3.3	Scheme of vectors used for description of a vortex line in parametrization of curve by value of z coordinate	47
3.4	Kelvin waves approximated dispersion relation	48
4.1	Schematic of vortex nucleus system with perspicuous explanation of symbols used in equations.	51
4.2	Visualization of vortex-nucleus system studied in TDSLDA model	52
4.3	Schematic of method used for extraction of vortex-nucleus force from TDSLDA model	53
4.4	3-D visualization of vortex-nucleus in different time steps.	54
4.5	Magnitude of the force acting between vortex and nucleus (per unit length of the vortex line)	55
4.6	Results from works of Epstein & Baym	57
4.7	Comparison of magnitude of vortex-nucleus forces in different models.	58
4.8	Analysis of power spectrum of moving quantum vortex deflections	60
5.1	Organization of program for Vortex Filament Model simulations	66
5.2	Vortex trajectories in dependence on Δz (neutron background den. 0.014 fm^{-3})	68
5.3	Vortex trajectories in dependence on Δz (neutron background den. 0.031 fm^{-3})	69

5.4	Example of initial configuration for simulation of vortex dynamics through a b.c.c. lattice of impurities. The simulation environment was planned in such a manner to allow the vortex to move one primitive cell of lattice along external flow direction.	72
5.5	Illustration of method for forcing periodicity on vortex-nucleus force	73
6.1	Spectrum of waves on a vortex line in SVFM simulations	77
6.2	Visualization of an example trajectory with dependence on time indicated by changing color and velocity in dependence of vortex position	79
6.3	Types of trajectories observed in numerical simulations	81
6.4	Comparison of methods for evaluation of vortex mean velocity	82
6.5	Mean vortex velocity as a function of external flow velocity, for neutron background density $n_n = 0.014 \text{ fm}^{-3}$	83
6.6	Mean vortex velocity as a function of external flow velocity, for neutron background density $n_n = 0.031 \text{ fm}^{-3}$	84
6.7	Example trajectories of mean position of vortex moving through the f.c.c. lattice obtained for neutron background density $n_n = 0.031 \text{ fm}^{-3}$	85
6.8	Example trajectories of mean position of vortex moving through the f.c.c. lattice obtained for neutron background density $n_n = 0.014 \text{ fm}^{-3}$	86
A.1	Frénet frame of reference	92

List of Tables

5.1	Padé approximant coefficients of the vortex-nucleus force	70
5.2	Comparison of the most important simulation parameters for two different neutron background particle densities n_n . For references see sec. 2.1.3, 2.1.4, 3.1.1, 3.4.3 and fig. 2.2.	70

Bibliography

- [1] P. Kapitza. Viscosity of liquid helium below the l-point. *Nature*, 141:74 EP –, Jan 1938. [15](#)
- [2] J. F. Allen and A. D. Misener. Flow of liquid helium ii. *Nature*, 141:75 EP –, Jan 1938. [15](#)
- [3] D. D. Osheroff, R. C. Richardson, and D. M. Lee. Evidence for a new phase of solid he^3 . *Phys. Rev. Lett.*, 28:885–888, Apr 1972. [15](#)
- [4] C. E. Wieman, E.A. Cornell, et al. Observation of Bose-Einstein Condensation in a Dilute Atomic Vapor. *Science*, 269(5221):198–201, 1995. [15](#)
- [5] C. A. , Jin D. S. Markus, G. , Regal. Bose-Einstein Condensation in a Gas of Sodium Atoms. *Nature*, 426, 2003. [15](#)
- [6] A. Bohr, B. R. Mottelson, and D. Pines. Possible analogy between the excitation spectra of nuclei and those of the superconducting metallic state. *Phys. Rev.*, 110:936–938, May 1958. [15](#)
- [7] A. B. Migdal. Superfluidity and the moments of inertia of nuclei. *Nuclear Physics*, 13(5):655 – 674, 1959. [15](#)
- [8] M. Gyulassy. The qgp discovered at rhic. In Walter Greiner, Mikhail G. Itkis, Joachim Reinhardt, and Mehmet Cem Güçlü, editors, *Structure and Dynamics of Elementary Matter*, pages 159–182, Dordrecht, 2004. Springer Netherlands. [15](#)
- [9] P. W. Anderson. Theory of dirty superconductors. *Journal of Physics and Chemistry of Solids*, 11(1):26 – 30, 1959. [15](#)
- [10] A. Bulgac, P. Magierski, K. J. Roche, and I. Stetcu. Induced fission of ^{240}Pu within a real-time microscopic framework. *Phys. Rev. Lett.*, 116:122504, Mar 2016. [16](#)
- [11] B. Haskell and A. Melatos. Models of pulsar glitches. *International Journal of Modern Physics D*, 24(03):1530008, 2015. [16](#), [17](#), [31](#), [32](#)
- [12] B. Haskell and A. Sedrakian. Superfluidity and superconductivity in neutron stars. *arxiv*, 09 2017. eprint, available at <https://arxiv.org/abs/1709.10340> (22.01.2018). [16](#), [26](#)
- [13] J. S. Bell Burnell. Petit four*. *Annals of the New York Academy of Sciences*, 302(1):685–689, 1977. [17](#)

- [14] W. Baade and F. Zwicky. Remarks on super-novae and cosmic rays. *Phys. Rev.*, 46:76–77, Jul 1934. [17](#)
- [15] J.J. Condon and S.M. Ransom. *Essential Radio Astronomy*. Princeton Series in Modern Observational Astronomy. Princeton University Press, 2016. [17](#)
- [16] V. Radhakrishnan and R. N. Manchester. Detection of a change of state in the pulsar psr 0833-45. *Nature*, 222:228 EP –, Apr 1969. [17](#), [30](#)
- [17] P. W. Anderson and N. Itoh. Pulsar glitches and restlessness as a hard superfluidity phenomenon. *Nature*, 256:25 EP –, Jul 1975. [17](#), [31](#)
- [18] M. Ruderman. Pulsar wobble and neutron starquakes. *Nature*, 225:838 EP –, Feb 1970. [17](#)
- [19] S. B. Popov. Tkachenko waves, glitches and precession in neutron stars. *Astrophysics and Space Science*, 317(3):175–179, Oct 2008. [17](#)
- [20] G. Włazłowski, K. Sekizawa, P. Magierski, A. Bulgac, and M. McNeil Forbes. Vortex pinning and dynamics in the neutron star crust. *Phys. Rev. Lett.*, 117:232701, Nov 2016. [19](#), [26](#), [27](#), [38](#), [41](#), [44](#), [49](#), [51](#), [52](#), [53](#), [54](#), [55](#), [56](#), [67](#), [70](#), [87](#)
- [21] B. Link. Dynamics of quantum vorticity in a random potential. *Phys. Rev. Lett.*, 102:131101, Apr 2009. [19](#), [42](#), [44](#), [46](#), [49](#), [55](#), [56](#), [71](#), [88](#)
- [22] T. Zhang, D. Celik, and S. W. Van Sciver. Tracer particles for application to piv studies of liquid helium. *Journal of Low Temperature Physics*, 134(3):985–1000, Feb 2004. [21](#)
- [23] G. P. Bewley, Daniel P. Lathrop, and Katepalli R. Sreenivasan. Visualization of quantized vortices. *Nature*, 441:588 EP –, May 2006. [21](#)
- [24] I. A. Pshenichnyuk. Pair interactions of heavy vortices in quantum fluids. *Physics Letters A*, 382(7):523 – 527, 2018. [21](#)
- [25] K. W. Schwarz. Three-dimensional vortex dynamics in superfluid ^4He : Line-line and line-boundary interactions. *Phys. Rev. B*, 31:5782–5804, May 1985. [21](#), [41](#), [42](#), [46](#)
- [26] J. G. Bednorz and K. A. Müller. Possible hightc superconductivity in the ba–la–cu–o system. *Zeitschrift für Physik B Condensed Matter*, 64(2):189–193, Jun 1986. [21](#)
- [27] D. Apushkinskaya, E. Apushkinskiy, and M. Astrov. Movement of a vortex filament near oscillating pinning centers in the hard superconductor. *Journal of Physics: Conference Series*, 633(1):012114, 2015. [21](#)
- [28] J. R. Oppenheimer and G. M. Volkoff. On massive neutron cores. *Phys. Rev.*, 55:374–381, Feb 1939. [23](#)
- [29] I. Bombaci. The maximum mass of a neutron star. *Astronomy and Astrophysics*, 305:871, January 1996. [24](#), [25](#)
- [30] N. Chamel, P. Haensel, J. L. Zdunik, and A. F. Fantina. On the maximum mass of neutron stars. *International Journal of Modern Physics E*, 22(07):1330018, 2013. [24](#)

- [31] S. Gandolfi, A. Gezerlis, and J. Carlson. Neutron matter from low to high density. *Annual Review of Nuclear and Particle Science*, 65(1):303–328, 2015. [24](#)
- [32] M. Okamoto, T. Maruyama, K. Yabana, and T. Tatsumi. Nuclear “pasta” structures in low-density nuclear matter and properties of the neutron-star crust. *Phys. Rev. C*, 88:025801, Aug 2013. [25](#), [26](#)
- [33] N. Chamel and P. Haensel. Physics of neutron star crusts. *P. Living Rev. Relativ.*, 2008. Pages 7 and 26-31. [25](#), [27](#)
- [34] B. K. Harrison, K. S. Thorne, M. Wakano, and J. A. Wheeler. *Gravitation Theory and Gravitational Collapse*. 1965. [25](#)
- [35] R. Shankar. *Principles of Quantum Mechanics*. Springer, 2012. [26](#)
- [36] E. Wigner and F. Seitz. On the constitution of metallic sodium. *Phys. Rev.*, 43:804–810, May 1933. [27](#)
- [37] J. W. Negele and D. Vautherin. Neutron star matter at sub-nuclear densities. *Nuclear Physics A*, 207(2):298 – 320, 1973. [27](#), [29](#)
- [38] M. Baldo, E. E. Saperstein, and S. V. Tolokonnikov. Upper edge of the neutron star inner crust: The drip point and its vicinity. *Phys. Rev. C*, 76:025803, Aug 2007. [27](#), [29](#)
- [39] P. Magierski and P.-H. Heenen. Structure of the inner crust of neutron stars: Crystal lattice or disordered phase? *Physical Review C*, 65(4):045804, Apr 2002. [27](#)
- [40] E. Jones, T. Oliphant, P. Peterson, et al. SciPy: Open source scientific tools for Python, 2001–. [Online; accessed 2017-23-12]. [28](#), [61](#), [65](#)
- [41] P. Dierckx. An algorithm for smoothing, differentiation and integration of experimental data using spline functions. *Journal of Computational and Applied Mathematics*, 1:165–184, 1975. [28](#)
- [42] P. Dierckx. An algorithm for surface-fitting with spline functions. *IMA Journal of Numerical Analysis*, 1(3):267–283, 1981. [28](#)
- [43] A. Pastore, S. Baroni, and C. Losa. Superfluid properties of the inner crust of neutron stars. *Phys. Rev. C*, 84(6):065807, December 2011. [28](#), [29](#)
- [44] F. Grill, J. Margueron, and N. Sandulescu. The cluster structure of the inner crust of neutron stars in the Hartree-Fock-Bogoliubov approach. 2011. [29](#)
- [45] M. Antonelli and P. Pizzochero. Axially symmetric equations for differential pulsar rotation with superfluid entrainment. 464, 03 2016. [30](#), [31](#)
- [46] B. Haskell, N. Andersson, and G. L. Comer. Dynamics of dissipative multifluid neutron star cores. *Phys. Rev. D*, 86:063002, Sep 2012. [32](#)
- [47] A. L. Fetter. Quantum theory of superfluid vortices. i. liquid helium ii. *Phys. Rev.*, 162:143–153, Oct 1967. [32](#), [40](#), [41](#), [47](#)

- [48] E. B. Sonin. Vortex oscillations and hydrodynamics of rotating superfluids. *Rev. Mod. Phys.*, 59:87–155, Jan 1987. [32](#), [40](#), [41](#), [47](#), [48](#)
- [49] J. Bardeen, L. N. Cooper, and J. R. Schrieffer. Theory of superconductivity. *Phys. Rev.*, 108:1175–1204, Dec 1957. [35](#)
- [50] L. N. Cooper. Bound electron pairs in a degenerate fermi gas. *Phys. Rev.*, 104:1189–1190, Nov 1956. [35](#)
- [51] J. F. Annett. *Superconductivity, Superfluids, and Condensates (Oxford Master Series in Physics)*. Oxford University Press, 2004. [36](#)
- [52] A. Bulgac and Y. Yu. Spatial structure of a vortex in low density neutron matter. *Phys. Rev. Lett.*, 90:161101, Apr 2003. [36](#), [42](#)
- [53] Burke K. [et al.]. *ABC of DTF*. 2007. Link: <http://dft.uci.edu/doc/g1.pdf> [Online; dostęp 15.02.2015]. [37](#)
- [54] L. D. Landau and E. M. Lifshitz. *Fluid Mechanics, Second Edition: Volume 6 (Course of Theoretical Physics S)*. Butterworth-Heinemann, 1987. [39](#)
- [55] H. Bhatia, G. Norgard, V. Pascucci, and P.-T. Bremer. The helmholtz-hodge decomposition-a survey. 19:1386–, 11 2012. [39](#)
- [56] L. Morino. Helmholtz decomposition revisited: Vorticity generation and trailing edge condition. *Computational Mechanics*, 1(1):65–90, Mar 1986. [39](#)
- [57] R. P. Feynman. Chapter ii application of quantum mechanics to liquid helium. volume 1 of *Progress in Low Temperature Physics*, pages 17 – 53. Elsevier, 1955. [40](#)
- [58] V. Espino. *On Point Vortex Solutions of the Euler Equations*. PhD thesis, University of New Mexico, 1987. Available at <http://www.math.unm.edu/~vageli/papers/victor.pdf> (11.12.2017). [40](#)
- [59] A. Bulgac and Y. Yu. Vortex state in a strongly coupled dilute atomic fermionic superfluid. *Phys. Rev. Lett.*, 91:190404, Nov 2003. [42](#)
- [60] D. J. Thouless, Ping Ao, Qian Niu, M. R. Geller, and C. Wexler. Quantized vortices in superfluids and superconductors. *International Journal of Modern Physics B*, 13(05n06):675–686, 1999. [42](#)
- [61] C. F. Barenghi, R. J. Donnelly, and W. F. Vinen. *Quantized Vortex Dynamics and Superfluid Turbulence*. Lecture Notes in Physics. Springer Berlin Heidelberg, 2001. [45](#), [46](#), [47](#)
- [62] M. Tsubota, M. Kobayashi, and H. Takeuchi. Quantum hydrodynamics. *Physics Reports*, 522(3):191 – 238, 2013. Quantum hydrodynamics. [45](#), [46](#)
- [63] Sir William Thomson. Xxiv. vibrations of a columnar vortex. *The London, Edinburgh, and Dublin Philosophical Magazine and Journal of Science*, 10(61):155–168, 1880. [47](#)

- [64] R. I. Epstein and G. Baym. Vortex drag and the spin-up time scale for pulsar glitches. *The Astrophysical Journal*, 387:276–287, March 1992. 47, 55, 56
- [65] R. I. Epstein and G. Baym. Vortex pinning in neutron stars. *The Astrophysical Journal*, 328:680–690, May 1988. 55, 56
- [66] N. E. Huang, Z. Shen, S. R. Long, Ma. C. Wu, H. H. Shih, Q. Zheng, N.-C. Yen, C. C. Tung, and H. H. Liu. The empirical mode decomposition and the hilbert spectrum for nonlinear and non-stationary time series analysis. *Proceedings of the Royal Society of London A: Mathematical, Physical and Engineering Sciences*, 454(1971):903–995, 1998. 60
- [67] D. Ascher, P. F. Dubois, K. Hinsen, J. Hugunin, T. Oliphant, et al. Numerical python, 2001. 65
- [68] J. D. Hunter. Matplotlib: A 2d graphics environment. *Computing In Science & Engineering*, 9(3):90–95, 2007. 65
- [69] P. Ramachandran and G. Varoquaux. Mayavi: 3D Visualization of Scientific Data. *Computing in Science & Engineering*, 13(2):40–51, 2011. 65